Dissertation

submitted to the

Combined Faculties of the Natural Sciences and Mathematics

of the Ruperto-Carola-University of Heidelberg, Germany

for the degree of

Doctor of Natural Sciences

Put forward by

Archana SAMPATH

born in Nagercoil, India.

Oral Examination: November 18, 2020

Strong-field QED and collisional effects in electron beam-plasma interaction

Referees:

Hon.-Prof. Dr. Christoph H. KEITEL
Prof. Dr. Joerg JAECKEL

Zusammenfassung

Intensive, hochenergetische Teilchenstrahlen werden in der physikalischen Grundlagenforschung, den Materialwissenschaften, der relativistischen Laborastrophysik sowie der Industrie verwendet. Üblicherweise werden dichte, kollimierte Multi-GeV-Photonen- und Elektronen-Positronenstrahlen durch Bremsstrahlung beziehungsweise Bethe-Heitler (BH) Elektron-Positron-Paarbildung erzeugt. Die jüngste Forschung konzentrierte sich auf Starkfeld-QED-Prozesse, um Fluss und Intensität der erzeugten Strahlen erheblich zu verstärken. Zur Bestimmung der relativen Rolle von Kollisions- und Starkfeld-QED-Prozessen haben wir Bremsstrahlung und BH-Paarproduktionsprozesse in den Particle-in-Cell-Code Smilei implementiert. Mittels Simulationen zeigen wir, dass ein ultrarelativistischer Hochstrom-Elektronenstrahl, der mit einer submikrometerdicken, leitenden Folie wechselwirkt, starke Selbstfokussierung erfahren kann; begleitet von einer effizienten Emission von Gammastrahlenphotonen. Wir untersuchen die Auswirkung variierender Elektronenstrahlform, Radius und Länge auf die endgültige Strahlungsenergie. Wir zeigen, dass selbsterzeugte Felder stark genug sein können, dass eine Emission im Starkfeld-QED-Regime auftritt, in dem ein einzelnes emittiertes Photon einen signifikanten Teil der Energie des emittierenden Elektrons wegtragen kann. Wir legen dar, dass wir, nach einer Strahlkollision mit mehreren Folien, femtosekunden-kollimierte Elektronen- und Photonenstrahlen mit einer Anzahldichte gewinnen, die die eines Festkörpers übersteigen. Diese Arbeit ist zeitgemäß, da sie laserlose QED-Untersuchungen in starken Feldern mit einem einzigen Hochstrom-Elektronenstrahl ermöglicht, die besonders relevant für die künftige FACET II-Einrichtung sind.

Abstract

Intense high-energy particle beams are used in fundamental sciences, material sciences, relativistic laboratory astrophysics, and in the industry. Traditionally, dense collimated multi-GeV photon and electron-positron beams are generated via bremsstrahlung and Bethe-Heitler (BH) electron-positron pair creation, respectively. Recent research has focused on strong-field QED processes for greatly enhancing the flux and intensity of the generated beams. To determine the relative role of collisional and strong-field QED processes, we implemented bremsstrahlung and BH pair production processes in the particle-in-cell code Smilei. Using simulations, we show that a high-current ultra-relativistic electron beam interacting with a submicrometer-thick conducting foils can undergo strong self-focusing accompanied by efficient emission of gamma-ray photons. We study the effect of varying electron beam shape, radius and length on the final radiated energy. We show that the self-generated fields can be strong enough that emission occurs in the strong-field QED regime, where a single emitted photon can carry away a significant fraction of the emitting electron energy. We demonstrate that, after beam collision with multiple foils, femtosecond collimated electron and photon beams with particle number density exceeding that of a solid are obtained. This study is timely as it enables laserless strong-field QED investigations with a single high-current electron beam, particularly relevant for the upcoming FACET II facility.

Within the scope of this thesis, the following article has been submitted for publication:

Extremely Dense Gamma-Ray Pulses in Electron Beam-Multifoil Collisions
Archana Sampath, Xavier Davoine, Sébastien Corde, Laurent Gremillet, Maitreyi Sangal, Christoph H. Keitel, Robert Ariniello, John Cary, Henrik Ekerfelt, Claudio Emma, Frederico Fiuza, Hiroki Fujii, Max Gilljohann, Mark Hogan, Chan Joshi, Alexander Knetsch, Valentina Lee, Mike Litos, Kenneth Marsh, Zan Nie, Brendan O'Shea, J. Ryan Peterson, Pablo San Miguel Claveria, Doug Storey, Yipeng Wu, Xinlu Xu, Chaojie Zhang and Matteo Tamburini
arXiv:2009.01808 [physics.plasm-ph] (2020)

Contents

List of Figures

List of Tables

Definitions and constants

Speed of light in vacuum	$c = 2.997\,924\,58 \times 10^{10}\,\mathrm{cm/s}$
Reduced Planck constant	$\hbar = 1.054\,571\,817 \times 10^{-36}\,\mathrm{cm^2 g/s}$
Electron charge	$e = 4.8032 \times 10^{-10}\,\mathrm{cm^{3/2} g^{1/2}/s}$
Electron rest mass	$m_e = 9.1094 \times 10^{-28}\,\mathrm{g}$
QED critical electric field	$E_c = 4.4 \times 10^{13}\,\mathrm{esu}$
QED critical magnetic field	$B_c = 4.4 \times 10^{13}\,\mathrm{gauss}$
Fine structure constant	$\alpha = \frac{e^2}{\hbar c}$
Classical electron radius	$r_e = 2.817\,940\,326\,2 \times 10^{-13}\,\mathrm{cm}$
Boltzmann constant	$k_B = 1.380\,649 \times 10^{-16}\,\mathrm{cm^2 g/s^2/K}$

Throughout the thesis Gaussian units are used unless otherwise specified.

Chapter 1

Introduction

1.1 Motivation

An important prediction of quantum electrodynamics (QED) is the "break-down" of vacuum in ultra-strong electromagnetic fields which results in the spontaneous generation of electron-positron pairs. The field strength required to test this prediction is of the order of the QED critical field $E_c = 1.3 \times 10^{16}$ V/cm, which corresponds to an intensity $I_c = 4.6 \times 10^{29}$ W/cm^2 (Sauter, 1931, Heisenberg and Euler, 1936, Schwinger, 1951). In these strong fields, exotic phenomena such as vacuum polarisation, light-by-light scattering, vacuum birefringence can also be tested (Toll, 1952, Antonino Di Piazza, Karen Zaven Hatsagortsyan, and Christoph Helmut Keitel, 2005, Heinzl et al., 2006, Marklund and Shukla, 2006, Fedotov and Narozhny, 2007, Di Piazza, Müller, et al., 2012). Hitherto, fields of such intensities and above are observed only in astrophysical environments such as magnetars (Kaspi and Beloborodov, 2017), binary neutron-star mergers (Xue et al., 2019), and core-collapse supernovae explosions (Mösta et al., 2015).

The journey to realise such fields in earth-based experiments gained momentum with the advent of chirped pulse amplification (CPA) technique in 1985 (Strickland and Mourou, 1985). With CPA, current high power laser facilities provide laser pulses with peak intensities of the order of 10^{22} W/cm^2, and next generation facilities such as the ELI will provide peak intensities greater than or equal to 10^{23} W/cm^2. Although such intensities remain much below the critical QED intensity, it is still possible to make use of presently available lasers to probe the strong-field QED regime. This is viable if one considers ultra-relativistic particles and recalls that QED is a Lorentz invariant theory. The field strengths in the rest frame of the ultra-relativistic particles are Lorentz boosted and approach the QED critical field already at laser intensities $I \lesssim 10^{22}$ W/cm^2. Thus, the onset of strong-field QED effects is governed by the quantum non-linearity parameter $\chi = E^*/E_c$ which compares the electromagnetic field in the rest frame of the particle (E^*) with the QED critical field (Di Piazza, Matteo Tamburini, et al., 2018).

To begin with, when a laser pulse with intensity 10^{18} W/cm^2 interacts with matter, the plasma electrons reach relativistic velocities within one laser time period and the electron motion becomes highly non-linear. In this relativistic regime, the quiver momentum p_0 of the plasma electrons is comparable to $m_e c$ where m_e is the electron

rest mass and c is the speed of light. The onset of relativistic effects is thus governed by the classical non-linearity parameter $a_0 = p_0/(m_e c) = eE/(m_e \omega c)$, where e is the charge of electron, E and ω are the laser electric field amplitude and frequency respectively (Di Piazza, Müller, et al., 2012). For a laser pulse with intensity 10^{18} W/cm^2 and wavelength $\lambda = 1\,\mu$m, $a_0 \gtrsim 1$.

A further increase in the laser intensities to the order of 10^{19-21} W/cm^2 generates relativistic electrons that can emit MeV bremsstrahlung photons which, in turn, can decay into Bethe-Heitler electron-positron pairs in the Coulomb field of a high Z nuclei. Both these collisional processes of radiation and pair production are strongly dependent on the atomic number Z of the target nuclei and on the incoming electron or photon energy. This led to the availability of new laser-assisted bremsstrahlung radiation sources and also in the generation of electron-positron pair plasmas. The laser field plays an indirect role here in the pair production process by serving solely as a particle accelerator, i.e., accelerates electrons that emits photons. In particular, dense electron-positron pair plasmas play a fundamental role in the dynamics of most powerful astrophysical systems such as blackholes, pulsars and quasars. The gamma-ray bursts observed from these pair plasmas are still poorly understood. Recently, the interaction of a laser generated electron beam with a solid lead (Pb) target was shown to produce high density (10^{16} cm^{-3}) pair plasmas with a small divergence of approximately 10-20 mrad (Sarri et al., 2015). These experimental findings open up the possibility of studying astrophysical environments in a controlled laboratory experiment. (Kmetec et al., 1992, Cowan et al., 2000, Santala et al., 2000, C. Chen et al., 2008, Compant La Fontaine, Courtois, and Lefebvre, 2012, Cipiccia et al., 2012, Courtois et al., 2013, Hui Chen, Scott C Wilks, et al., 2009, Hui Chen, S. Wilks, et al., 2010, Liang, 2010, Hui Chen, Fiuza, et al., 2015).

With the next upgrade of laser intensities ($I > 5\times10^{22}$ W/cm^2, Powell, 2013), in addition to the Coulomb fields, the laser fields experienced by the electrons in their rest frame is strong enough to trigger photon emission via non-linear Compton scattering (J.-X. Li, Karen Z. Hatsagortsyan, et al., 2015, Di Piazza, Müller, et al., 2012). This implies, the quantum non-linearity parameter χ of the electrons approaches unity. This opened up a new channel to generate laser based photon sources. Furthermore, pair production by photons propagating in a strong laser field (non-linear Breit-Wheeler pair production) also becomes viable when the χ parameter of the photon is approximately greater than unity. Thus the value of quantum non-linearity parameter $\chi \gtrsim 1$ marks the onset of quantum regime during laser-matter interaction (Di Piazza, Müller, et al., 2012). Based on these mechanisms of photon emission and pair production, different groups have proposed various configurations to generate intense photon beams and dense pair plasmas. The laser accelerated electrons are able to generate photons in a wide range of energy ranging from the extreme ultraviolet (XUV) to the gamma rays. These sources were seen as a potential alternative to conventional synchrotron sources, due to their compact size, potential for high brightness, and femtosecond duration. Such ultrashort, compact, high-energy gamma beams attract attention for their

numerous applications in fundamental science, industry, medicine, biology, chemistry and material science. For example, to resolve the timescales of atomic or nuclear transitions (Habs et al., 2009), for probing hot dense matter (Ben-Ismaïl et al., 2011), and for synthesising materials (Seguchi et al., 2002). Laser based photon sources that rely on triggering non-linear Compton scattering has attracted attention recently. Ridgers et al., 2012 show that during the interaction of 10 PW laser with a solid density aluminium target, dense electron-positron pair plasma is generated. Their simulations reported a positron density of 10^{26} /m^3 and approximately 35% conversion of laser energy into synchrotron photons. Nakamura et al., 2012 also propose the use of 10 PW lasers with tailored targets to convert approximately 32% of laser energy into high energy gamma photons. Ji et al., 2014 performed simulations to understand the laser energy absorption via different processes such as absorption via electrons, ions, photons and concluded that conversion efficiency of laser energy into collimated photons increases as the relativistic transparency regime of interaction is reached. J.-X. Li, Karen Z Hatsagortsyan, et al., 2015 propose the collision of intense laser pulse with electron beam to generate attosecond gamma-ray pulses. Similar proposals to further increase attainable photon energy and flux focus on laser-plasma interactions (Chang et al., 2017, W.-M. Wang et al., 2018, Huang et al., 2019, Vranic, Thomas Grismayer, Sebastian Meuren, et al., 2019, Jirka, Ondrej Klimo, Gu, et al., 2020, Zhu et al., 2020). Furthermore, Magnusson et al., 2019 propose the collision of high energy electron beams with strong laser fields generated by the collision of multiple laser pulses to generate intense photon beams.

A unique phenomena that can be triggered during collisions of multiple laser pulses is the formation of QED cascades. QED cascades are avalanche processes of hard photon emission and electron-positron pair creation driven by ultra-strong electromagnetic fields. They play an essential role in extreme astrophysical scenarios (Remington, Drake, and Ryutov, 2006). This complex cyclical process of hard photon emission and electron-positron pair production leads to an exponential growth in the number of particles. For example, in magnetars, strong-field QED cascades fill the magnetosphere with a relativistic electron-positron pair plasma (Medin and Lai, 2010, A. Y. Chen, Cruz, and Spitkovsky, 2020 Timokhin and Harding, 2019). Magnetars are rotating magnetized neutron stars with strong surface magnetic field strengths. In particular, the field strengths are up to 10^{15} G, well above the QED critical field strength (B_c = 4.4 $\times$ 10^{13} G). It is pertinent to note that a pure magnetic field can exceed the QED critical field strength as it cannot spontaneously create pairs in vacuum. Surrounding these stars, there are electrons that emit hard photons which convert into electron-positron pairs, which in turn emit photons, leading to the initiation of QED cascades. Magnetars were recently suggested as the most promising progenitors of the mysterious "Fast Radio Bursts" (FRBs) (Tavani et al., 2020, Lin et al., 2020, Ridnaia et al., 2020, C. Li et al., 2020, Bochenek et al., 2020, Andersen et al., 2020). Hence, understanding this new dense electron-positron-gamma plasma regime will pave way for the rendering of earth-based astrophysical experiments. The formation of QED cascades was also

demonstrated as a possible route to efficiently generate GeV photon source (Gonoskov et al., 2017).

The necessary criteria for using lasers for the spontaneous creation of pairs from vacuum is that the laser field invariant $\mathcal{E} = \sqrt{(\mathcal{F}^2 + \mathcal{G}^2)^{1/2} + \mathcal{F}}$ must approach the QED critical field strength E_c. $\mathcal{F} \equiv \left(\boldsymbol{E}^2 - \boldsymbol{B}^2\right)/2$ and $\mathcal{G} \equiv \boldsymbol{E} \cdot \boldsymbol{B}$ are the electromagnetic field invariants, with $\boldsymbol{E}$ and $\boldsymbol{B}$ being the electric and magnetic field, respectively. One of the simplest configuration for satisfying this condition is during the collision of multiple laser pulses. Bell and Kirk, 2008 proposed the use of seed electrons during the collision of two counter-propagating laser pulses to initiate a cascade. Recently, the effect of laser parameters such as the intensity, polarisation, waist radius, the spatial and temporal gradients of the pulse on the development of cascades have been thoroughly investigated (Bulanov, Mur, et al., 2010, Elkina et al., 2011, Bashmakov et al., 2014 , A. Mironov, Narozhny, and Fedotov, 2014, Gelfer et al., 2015, Thomas Grismayer, Vranic, Joana Luis Martins, et al., 2016, Vranic, Thomas Grismayer, Fonseca, et al., 2016, Thomas Grismayer, Vranic, Joana L Martins, et al., 2017, Matteo Tamburini, Antonino Di Piazza, and Christoph H Keitel, 2017, Jirka, Ondrej Klimo, Vranic, et al., 2017, Sampath and Matteo Tamburini, 2018). In fact, Matteo Tamburini, Antonino Di Piazza, and Christoph H Keitel, 2017 demonstrated both the possibility of onset of QED cascades and prevention of QED cascades during the collision of laser pulses. They show that even at very high laser intensities 10^{26} W/cm^2, tightly focused laser pulses and low-Z gases prevent the onset of cascades, while high-Z gases and large focal waist triggers the onset of cascades at lower intensities (10^{24} W/cm^2). Understanding the prevention of cascade formation is crucial as the development of these dense electron-positron-gamma plasma is predicted to deplete the complete laser energy in vacuum. The formation of these QED cascades thereby impose a threshold on the attainable laser intensities (Fedotov, Narozhny, et al., 2010). The role of high Z elements to support initiation of QED cascades was further investigated by Artemenko and Kostyukov, 2017. The literature mentioned above focused on using two or more laser pulses with or without seed particles for the initiation and development of QED cascades. Alternatively, A. Mironov, Narozhny, and Fedotov, 2014, and Arsenii Antonovich Mironov, Aleksandr Mikhailovich Fedotov, and Narozhnyi, 2016 propose the collision of an ultra-relativistic GeV electron beam with an intense laser field. Here the Lorentz boosted electric field in the rest frame of the electron aids in the development of QED showers. Recently, Qu, Sebastian Meuren, and Fisch, 2020 propose the use of a 3PW laser with a 30 GeV electron beam to observe the collective plasma effects that develop during the formation of QED showers when the generated particle density approaches the critical plasma density.

Based on the above, we observe that the generation of intense high energy particle beams and photon beams, along with the production of dense electron-positron pair plasmas are being investigated vigorously using laser beams within the scientific community. In general, we have two major channels for novel radiation sources and

for the generation of electron-positron-gamma plasmas. The collisional processes of bremsstrahlung emission and Bethe-Heitler pair production, and the strong-field processes of non-linear inverse Compton scattering and multiphoton-Breit Wheeler pair production. On the one hand, the competition between these two channels have been studied extensively by Martinez, 2018 in the context of laser-plasma interactions. Their works have shown that the efficiency of bremsstrahlung emission is comparable with that of synchrotron emission during the interaction between a laser pulse with intensity 10^{22} W/cm^2 and a one-micron thick copper foil. On the other hand, the relative role of collisional and strong-field processes is largely unexplored in the context of high current electron beam interaction with matter. Within the context of this thesis, we would like to address this question and also explore the possibility of accessing strong-field QED regimes with a single high-current electron beam.

The interaction of dense ultra-relativistic electron beams with matter has gained attention in the recent times. Specifically their potential to generate collimated photon sources is being explored. It was demonstrated by Benedetti, Matteo Tamburini, and Christoph H Keitel, 2018 that the interaction of an ultra-relativistic electron beam with millimetre thick aluminium targets trigger electromagnetic instabilities when the electron beam density is above 3×10^{19}/cm^3. The ultra-relativistic electrons traverse through strong self-generated fields resulting in the production of collimated gamma-ray pulse with photon energies ranging from 200 keV to GeV and upto 60% conversion of electron energy into photons. Another viable route for photon beam generation and strong-field QED investigations is during the collision of particle beams. Beamstrahlung emission occurs during the collision of particle beams. Physically, the particles of the first beam experience the strong electromagnetic fields of the second beam and get deflected and emit beamstrahlung radiation. Although this process was previously considered detrimental, more recently, research has focused on the use of beamstrahlung emission as a viable gamma beam source (Matteo Tamburini and Sebastian Meuren, 2019, Del Gaudio et al., 2019). Collision of tightly compressed and focused electron beams to explore the non-perturbative QED regime has also been proposed recently by Yakimenko, Meuren, et al., 2019.

All these proposals to understand the strong-field QED regime in the context of laser-plasma or electron beam-plasma are innovative and necessary. Through the course of this thesis, we explore an unique possibility of accessing strong-field QED regime in a laserless setup, with a single high current electron beam (Sampath, Davoine, et al., 2020). This timely study is relevant for the upcoming FACET II facility.

1.2 Key results and thesis outline

1.2.1 Key results

In our work, we use Particle-In-Cell (PIC) simulations to investigate the role of collisional and strong field processes in electron-beam plasma interactions. We show that

an ultra-relativistic electron beam during the interaction with a conductor foil(s), undergoes strong self-focusing accompanied by efficient gamma-ray emission. We discuss the physical origin for both self-focusing and photon emission as near field transition radiation that arises during beam-foil collision. We show that these effects can be enhanced during the collision of the electron beam with a series of conducting foils and approximately 30% energy of the electron beam can be efficiently converted into a dense collimated gamma beam. In this interaction, we show that the quantum parameter χ_e that determines the strength of strong-field QED effects approaches ~ 3, indicating the possibility of accessing the strong field QED regime ($\chi > 1$) with a single electron beam and without external super intense laser fields.

1.2.2 Outline

This thesis is organised in the following way.

In Chapter 2, we describe the Maxwell-Vlasov model, which provides the basic governing equations for studying a collisionless plasma. Subsequently, we provide an overview of the numerical tool used to solve the Maxwell-Vlasov equations, i.e., the Particle-In-Cell (PIC) codes. We also mention the latest additions to PIC method which enables one to study electron beam-plasma interactions with these codes.

In Chapter 3, we discuss the modelling of Monte Carlo processes in a PIC code. We implement collisional processes such as bremsstrahlung emission and Bethe-Heitler pair production which are important during the interaction of laser or electron/photon beam with matter in the PIC code SMILEI. We consider the ultra-relativistic regime for both these processes and and describe the cross-sections used within our implementation. Moreover, as bremsstrahlung emission and Bethe-Heitler pair production occur in the field of a nucleus, the screening of nuclear field by surrounding electrons can be significant depending on the beam and target plasma parameters of interaction. Hence, we implement the two limiting cases of nuclear field screening, the non-screened and completely screened regime.

We then present results of our test simulations validating these models against theoretical predictions.

In Chapter 4, we discuss the interaction of an ultra-relativistic electron beam with a sub-micrometre thick aluminium foil. We discuss our analytical model based on the method of images to understand the key phenomena of self-focusing and photon emission during this interaction. We conduct parametric scans for understanding the dependence of total radiated energy on electron beam length, beam radius, beam shape and beam energy. We extend this study to put forward a relatively simple setup for the generation of dense collimated electron and photon beam. For this, we propose the interaction of an ultra-relativistic electron beam with a periodic array of aluminium foils. We show the legitimacy of 2D and 3D simulation results with the aid of analytical predictions.

Finally in Chapter 5, we provide a summary of our work and its future prospects.

Chapter 2

Theoretical Background

In this chapter we give an introduction to the basic equation and numerical tools that will be used throughout this thesis. We begin with a brief description of the relativistic Maxwell-Vlasov model and then discuss the numerical tool used to solve these equations for plasmas: the Particle-In-Cell method. These PIC codes have been used for decades to gain deeper insights into relativistic laser beam or electron beam interactions with plasma.

2.1 Maxwell-Vlasov model

The starting point to describe a collisionless plasma is the Maxwell-Vlasov description. In this description, a particle species s with charge q_s and mass m_s is described by it's distribution function $f_s(\boldsymbol{x}, \boldsymbol{p}, t)$. This distribution function $f_s \equiv f_s(\boldsymbol{x}, \boldsymbol{p}, t)$ represents the particle density in phase space at point $(\boldsymbol{x}, \boldsymbol{p})$ and at time t. The time evolution of f_s under the influence of a collective electromagnetic field created in the point $\boldsymbol{x}$ at a time t field is given by the Vlasov equation,

$$\partial_t f_s + \boldsymbol{v}_s(\boldsymbol{p}) \cdot \nabla f_s + \boldsymbol{F}_L \cdot \nabla_{\boldsymbol{p}} f_s = 0 \tag{2.1}$$

where ∇ and $\nabla_{\boldsymbol{p}}$ represent the gradients of f_s with respect to the position and momentum variables respectively. The velocity is related to the momentum of the particle by $\boldsymbol{v_s}(\boldsymbol{p}) = \frac{\boldsymbol{p}}{m_s \gamma_s}$, where γ_s is the Lorentz factor given by $\gamma_s = \sqrt{1 + \frac{|\boldsymbol{p}|^2}{m_s^2 c^2}}$.
$\boldsymbol{F}_L$ is the Lorentz force given by,

$$\boldsymbol{F}_L = q_s \left[\boldsymbol{E} + \left(\boldsymbol{v}_s(\boldsymbol{p})/c \right) \times \boldsymbol{B}) \right] \tag{2.2}$$

The fields $\boldsymbol{E}$ and $\boldsymbol{B}$ follow the Maxwell's system of equations given by:

$$\begin{aligned} \nabla \cdot \boldsymbol{B} &= 0 \\ \nabla \cdot \boldsymbol{E} &= 4\pi\rho \\ \nabla \times \boldsymbol{E} &= -\frac{1}{c}\frac{\partial \boldsymbol{B}}{\partial t} \\ \nabla \times \boldsymbol{B} &= \frac{1}{c}\frac{\partial \boldsymbol{E}}{\partial t} + \frac{4\pi}{c}\boldsymbol{j} \end{aligned} \tag{2.3}$$

where the source terms ρ and $\boldsymbol{j}$ are the charge density and current density respectively. They can be obtained from the distribution function of the particles using the relations,

$$\begin{aligned} \rho(\boldsymbol{x},t) &= \sum_s q_s \int f_s(\boldsymbol{x},\boldsymbol{p},t)\mathrm{d}\boldsymbol{p} \\ \boldsymbol{j}(\boldsymbol{x},t) &= \sum_s q_s \int f_s(\boldsymbol{x},\boldsymbol{p},t)\boldsymbol{v_s}(\boldsymbol{p})\mathrm{d}\boldsymbol{p} \end{aligned} \tag{2.4}$$

The Vlasov equation 2.1 when it takes into account the self-consistent electromagnetic field generated by the particles in the plasma, is coupled to the Maxwell equations 2.3. These coupled system of equations enables us to describe the self-consistent dynamics of a collisionless plasma. For any real system, solving these coupled partial differential equations is non-trivial and requires the use of numerical tools. In the next section, we describe a well established numerical method, based on finite element approach called the Particle-In-Cell (PIC) method.

2.2 Particle-In-Cell

A plasma in reality is an ensemble of many charged particles which are interacting with each other via their self-consistently generated fields. It is challenging to follow the evolution of all these real particles using the Maxwell-Vlasov coupled system of equations. In a PIC code, this is addressed by using the concept of a numerical macro-particle that is a representative of many real particles. In short, we follow the evolution of a numerical plasma consisting of heavy macro-particles that have the same charge-to-mass ratio as the real plasma particles (electrons or ions) on a discretised grid (Refer Figure 2.1).

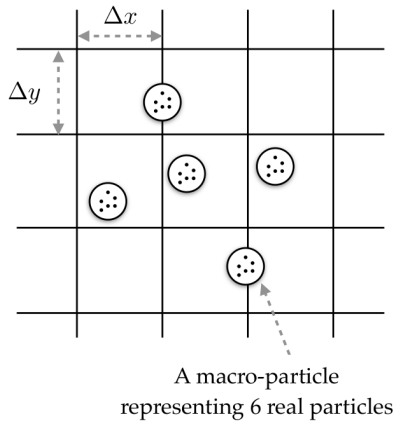

FIGURE 2.1: A schematic of the two dimensional discretised PIC spatial domain with grid resolution Δx and Δy. The numerical plasma distribution in the figure is represented by 5 macro-particles each representing 6 real particles.

The resolution of the discretised grid ($\Delta x, \Delta y$ and Δz in 3D) sets a lower limit to the spatial resolution of particle-particle or particle-field interaction. In general, the common length scales that define the characteristics of a plasma are the plasma electrons' skin-depth and the Debye length. The skin-depth governs the distance up-to which electromagnetic radiations can penetrate within a plasma and is given by $l_{skin} = c/\omega_{pe}$ where ω_{pe} is the plasma electrons' oscillation frequency. For a plasma with electron density n_e,

$$\omega_{pe} = \left(\frac{4\pi n_e e^2}{m_e}\right)^{\frac{1}{2}} \tag{2.5}$$

The Debye length (λ_D) determines the length scale at which electric fields are screened out by a redistribution of the plasma electrons,

$$\lambda_D = \left(\frac{k_B T_e}{4\pi n_e e^2}\right)^{\frac{1}{2}} \tag{2.6}$$

Similarly, the size of time step Δt is decided based on the time scale of the physical phenomena we are interested in. Usually, this is determined by either the laser beam or electron beam time scale or the target plasma time scale.

The mathematical representation of the PIC method is obtained by assuming that the distribution f_s is given by the superposition of N_s macro-particles.

$$f_s(\boldsymbol{x}, \boldsymbol{p}, t) = \sum_{p=1}^{N_s} w_p S\left(\boldsymbol{x} - \boldsymbol{x}_p(t)\right) \delta\left(\boldsymbol{p} - \boldsymbol{p}_p(t)\right) \tag{2.7}$$

where w_p is the numerical weight of the macro-particle, ($\boldsymbol{x}, \boldsymbol{p}$) it's position and momentum at time t, $S\left(\boldsymbol{x} - \boldsymbol{x}_p(t)\right)$ is the shape function for the macro-particles (spatial form of the macro-particles) and $\delta\left(\boldsymbol{p} - \boldsymbol{p}_p(t)\right)$ represents the Dirac distribution for momentum.

The shape functions for the macro-particles have the following properties.

- Symmetric with respect to their argument x, implies, $S\left(\boldsymbol{x} - \boldsymbol{x}_p\right) = S\left(\boldsymbol{x}_p - \boldsymbol{x}\right)$
- They are compact such that they describe a small portion of the spatial grid, i.e., it is zero outside a small range.
- Their integral is normalised to unity, i.e., $\int_{-\infty}^{\infty} S\left(\boldsymbol{x}\right) \mathrm{d}\boldsymbol{x} = 1$

For a species (plasma electron or ions) with number density n_s, the weights of the macro-particles present in a computational cell of size $\mathrm{d}V = \mathrm{d}x\mathrm{d}y\mathrm{d}z$ with N_{ppc} macro-particles per cell is defined as,

$$w_p = \frac{n_s dV}{N_{ppc}} \tag{2.8}$$

By taking a partial time derivative of the discrete distribution function f_s in Equation 2.7, we obtain

$$\begin{aligned}\partial_t f_s &= -w_p \sum_{p=1}^{N_s} \{\delta(\boldsymbol{p}-\boldsymbol{p}_p(t))\dot{\boldsymbol{x}}_p(t)\cdot\nabla S(\boldsymbol{x}-\boldsymbol{x}_p(t)) \\ &\quad +S(\boldsymbol{x}-\boldsymbol{x}_p(t))\dot{\boldsymbol{p}}_p(t)\cdot\nabla_{\boldsymbol{p}}\delta(\boldsymbol{p}-\boldsymbol{p}_p(t))\} \\ &= -w_p \sum_{p=1}^{N_s} \{\nabla\cdot(\dot{\boldsymbol{x}}_p(t)S(\boldsymbol{x}-\boldsymbol{x}_p(t))\delta(\boldsymbol{p}-\boldsymbol{p}_p(t))) \\ &\quad +\nabla_{\boldsymbol{p}}\cdot(\dot{\boldsymbol{p}}_p(t)S(\boldsymbol{x}-\boldsymbol{x}_p(t))\delta(\boldsymbol{p}-\boldsymbol{p}_i(t)))\}\end{aligned} \tag{2.9}$$

Substituting Equation 2.7 and Equation 2.9 in Equation 2.1,

$$\begin{aligned}\sum_{p=1}^{N_s} \{\nabla\cdot[(\boldsymbol{v}_s(\boldsymbol{p})-\dot{\boldsymbol{x}}_p(t))\,S(\boldsymbol{x}-\boldsymbol{x}_p(t))\,\delta(\boldsymbol{p}-\boldsymbol{p}_p(t))\,]+ \\ +\nabla_{\boldsymbol{p}}\cdot[(\boldsymbol{F}_L-\dot{\boldsymbol{p}}_p(t))\,S(\boldsymbol{x}-\boldsymbol{x}_p(t))\,\delta(\boldsymbol{p}-\boldsymbol{p}_p(t))]\}=0\end{aligned} \tag{2.10}$$

On integrating Equation 2.10 over all $\boldsymbol{p}$ gives,

$$\begin{aligned}&\sum_{p=1}^{N_s}\nabla\cdot[(\boldsymbol{v}_s(\boldsymbol{p}_p(t))-\dot{\boldsymbol{x}}_p(t))\,S(\boldsymbol{x}-\boldsymbol{x}_p(t))] \\ =&\sum_{p=1}^{N_s}[(\boldsymbol{v}_s(\boldsymbol{p}_p(t))-\dot{\boldsymbol{x}}_p(t))]\cdot\nabla S(\boldsymbol{x}-\boldsymbol{x}_p(t))=0\end{aligned} \tag{2.11}$$

as the flux of $[(\boldsymbol{F}_L-\dot{\boldsymbol{p}}_p(t))\,S(\mathbf{x}-\mathbf{x}_p(t))\delta(\boldsymbol{p}-\mathbf{p}_p(t))]$ is zero when $\boldsymbol{p}\to\pm\infty$. As the gradient of the spatial shape function is not zero, one obtains from Equation 2.11,

$$\dot{\mathbf{x}}_p(t)=\boldsymbol{v}_s(\boldsymbol{p}_p(t)) \tag{2.12}$$

On integrating Equation 2.10 over all $\boldsymbol{x}$ and as the flux of $[(\boldsymbol{v}_s(\boldsymbol{p}_p(t))-\dot{\boldsymbol{x}}_p(t))\,S(\mathbf{x}-\mathbf{x}_p(t))\delta(\boldsymbol{p}-\mathbf{p}_i(t))]$ is zero when $\boldsymbol{x}\to\pm\infty$, one obtains

$$\begin{aligned}&\sum_{p=1}^{N_s}\nabla_{\boldsymbol{p}}\cdot\left[\int(\boldsymbol{F}_L-\dot{\boldsymbol{p}}_p(t))\,S(\boldsymbol{x}-\boldsymbol{x}_p(t))\delta(\boldsymbol{p}-\boldsymbol{p}_p(t))\mathrm{d}\boldsymbol{x}\right]= \\ =&\sum_{p=1}^{N_s}\nabla_{\boldsymbol{p}}\cdot\left[\int\boldsymbol{F}_L S(\boldsymbol{x}-\boldsymbol{x}_p(t))\delta(\boldsymbol{p}-\boldsymbol{p}_p(t))\mathrm{d}\boldsymbol{x}-\dot{\boldsymbol{p}}_p(t)\delta(\boldsymbol{p}-\boldsymbol{p}_p(t))\right]= \\ =&\sum_{p=1}^{N_s}\left[\int\boldsymbol{F}_L S(\boldsymbol{x}-\boldsymbol{x}_p(t))\mathrm{d}\boldsymbol{x}-\dot{\boldsymbol{p}}_p(t)\right]\cdot\nabla_{\boldsymbol{p}}\delta(\boldsymbol{p}-\boldsymbol{p}_p(t))=0\end{aligned} \tag{2.13}$$

and we obtain the relativistic equations of motion for the macro-particles.

$$\begin{aligned}\dot{\boldsymbol{p}}_p(t)&=\int\boldsymbol{F}_L S\left(\boldsymbol{x}-\boldsymbol{x}_p(t)\right)\mathrm{d}\boldsymbol{x} \\ \implies\partial_t\boldsymbol{p}_p&=q_s\left(\boldsymbol{E}_p+\boldsymbol{v}\times\boldsymbol{B}_p\right)\end{aligned} \tag{2.14}$$

where,

$$\begin{aligned} \boldsymbol{E}_p &= \int \mathrm{d}\boldsymbol{x} S\left(\boldsymbol{x} - \boldsymbol{x}_p(t)\right) \boldsymbol{E}(\boldsymbol{x}) \\ \boldsymbol{B}_p &= \int \mathrm{d}\boldsymbol{x} S\left(\boldsymbol{x} - \boldsymbol{x}_p(t)\right) \boldsymbol{B}(\boldsymbol{x}) \end{aligned} \tag{2.15}$$

In essence, the macro-particles evolve as a set of real particles. This shows that the PIC method is a fully consistent approximation to the Maxwell-Vlasov model.

Now that we described the basic equations which we solve for the fields and the particles, we briefly present the basic PIC algorithm. It consists of the following steps:

- At time $t = 0$, initialise all the macro-particles with their charge, mass, weight, spatial and momentum distribution.
- At $t = 0$, project the charge density and current density on to the computational grid.
- At $t = 0$, using the source charge and current densities, compute the initial electric and magnetic fields at the grid points.
- PIC time loop begins:
  - Interpolate the electric and magnetic fields at the particle position.
  - Push the particles according to the equations of motion 2.12 and 2.14 . One of the commonly used method to integrate these equations of motion is the leap frog method.
  - Project the new current and charge densities onto the grid.
  - Compute the new electric and magnetic fields on the grid (Equation 2.15).

The PIC algorithm described so far is accurate for a collisionless plasma and the propagation of the corresponding electromagnetic fields. Different groups across the world have immensely contributed in the development and scaling of these codes. It does not include physical effects that will arise during the interaction of plasma with external electromagnetic fields, lasers, and matter. The most common physical processes that occur during these interactions are described below. We briefly mention their implementation in

1. Binary Coulomb collisions: The trajectory of a charged particle is influenced by the Coulomb force exerted on it by the background charges present in the plasma. The effect of this Coulomb interaction between charged particles can be taken into account in PIC codes via Monte-Carlo algorithm. The general algorithm is further described in section 3.1. The modelling of relativistic collisions and collisional ionisation is thoroughly described by Nanbu, 1997, Nanbu and Yonemura, 1998, Sentoku and Kemp, 2008, Pérez et al., 2012.
2. Ionisation: Ionisation of the atoms present in target material occur both through collisions of charged species, or due to the presence of an external field (such

as laser). With appropriate knowledge of ionisation cross-sections, Monte-Carlo algorithms are again used to incorporate their effect in PIC codes. The field and collisional ionisation models implemented in PIC codes are described in the works of Nuter et al., 2011 and Pérez et al., 2012 respectively.

3. Radiation: When charged particles are accelerated they emit radiation. If the acceleration is very large, then the charge particle also experiences a significant effect of recoil. In the classical regime, it can be treated as a continuous friction force acting on the particles. In PIC codes, these radiation reaction force can be treated using Landau and Lifshitz, 1980 model, and are implemented in the particle pusher using a splitting technique proposed by Tamburini et al., 2010.

4. Strong field emission and pair production: When the emitted radiation is due to a strong electromagnetic field, the process of photon emission and pair production are probabilistic and can be treated stochastically. These are implemented via the Monte-Carlo algorithm within the PIC code (Duclous, Kirk, and Bell, 2010, Lobet, 2015, Duclous, Kirk, and Bell, 2010).

5. Nuclear field emission and pair production: Similar to strong-field processes, the scattering of an electron and the subsequent emission of bremsstrahlung photon, and the decay of a photon into electron-positron pairs in Coulomb field are treated as stochastic processes within the PIC code. They are also implemented via the Monte-Carlo algorithm. As a part of this thesis, we implement these nuclear field processes in a PIC code and this is further explained in Chapter 3.

In summary, we have described the basic numerical tool that we will be using for all our simulations performed during the course of this thesis. In particular, we use the open-source PIC code SMILEI developed by Derouillat et al., 2018 for our investigations.

Chapter 3

Bremsstrahlung Emission and Bethe-Heitler Pair Production

The process of bremsstrahlung emission by charged particles and Bethe-Heitler pair creation by photons are probabilistic. The differential cross-sections for both the processes vigorously grows with the atomic number of the target nuclei, and is dependent on the energy of the charged particle (photon) and the newly generated photon (electron-positron pair). In general, in PIC simulations, these two processes are treated as binary collision processes. At every time-step within each computational cell, for each pair of macro-particles, one computes the probability of the event and obtains the resultant photon/pair energy via the inverse transform sampling method.

3.1 Monte-Carlo processes in Particle-in-Cell codes

3.1.1 Algorithm

In this section, we briefly describe the well established Monte-Carlo algorithm for the simulation of stochastic processes. Using this technique, we implement bremsstrahlung emission and Bethe-Heitler pair production processes within PIC code SMILEI (Derouillat et al., 2018). We treat both emission and pair production under the binary collision approximation, i.e., they are separated into a series of distinct two-particle encounters. Inside the main PIC time-loop, at every time-step and inside every computational cell of the PIC grid, the macro-particles are shuffled and randomly paired. For each pair of macro-particles, we

1. identify the beam (b) and the target (t) particle,
2. calculate the collision rate W_{total} for the event (bremsstrahlung emission and/or Bethe-Heitler pair creation) given by (Akhiezer and Berestetskii, 1986),

$$W_{total} = \frac{\Delta P}{\Delta t} = \sigma(\varepsilon) v_{rel} n_t \tag{3.1}$$

where $\frac{\Delta P}{\Delta t}$ gives the probability of the event per time-step per beam particle, n_t is the target particle number density, $\sigma(\varepsilon)$ is the total cross-section for the process and v_{rel}, the velocity of beam (target) particle in the rest frame of target (beam) particle. $\sigma(\varepsilon)$ and the relative velocity v_{rel} are given by

$$\begin{aligned} \sigma(\varepsilon) &= \int_{x_{min}}^{x_{max}} \frac{\mathrm{d}\sigma(\varepsilon, x)}{\mathrm{d}x} \mathrm{d}x \\ v_{rel} &= \frac{\sqrt{(p_{bi} p_t^i)^2 - m_b^2 m_t^2}}{\varepsilon_b \varepsilon_t} \end{aligned} \tag{3.2}$$

where x is the energy of the particle that is a result of this collision (photon for bremsstrahlung emission and positron or electron for Bethe-Heitler pair production), $p_{b/t}^i$ and $m_{b/t}$ are the four momenta and mass of the relevant beam or target particle.

3. The probability of the event $W\Delta t$ is then compared with a random number r between 0 and 1. If $W\Delta t > r$, the collision occurs.

4. The corresponding photon (pair) energy is computed by solving the sampling equation,

$$\int_{x_{min}}^{x} \frac{\mathrm{d}W(x)}{\mathrm{d}x} \mathrm{d}x = r W_{total} \tag{3.3}$$

where r is a new random number between 0 and 1.

3.1.2 Different Weights for Beam and Target Macro-particles

The algorithm in the previous section works as such without modifications for collisions between real particles. As PIC codes make use of macro-particles (refer Section 2.2), we account for their numerical weights by using the technique proposed by Nanbu and Yonemura, 1998. They modify the effective interaction time-step Δt experienced by each macro-particle during collisions to compensate for artificial numerical effects arising from macro-particle weights. We explain their method with the help of an example.

Consider two species (beam (b) and target (t)) colliding within a single cell of the computational grid. Let the number of macro-particles corresponding to the beam and target species within this cell be N_b and N_t, and the corresponding numerical weights of each macro-particle be W_b and W_t. The first step is to shuffle and pair the macro-particles within a PIC cell. If $N_b = N_t$, each beam and target macro-particles are given unique collision partners. While, if $N_b > N_t$ ($N_t > N_b$), certain target (beam) particles must undergo repeated collisions. As a result, necessary duplicates of macro-particles are created to ensure all macro-particles have pairs (Refer Figure 3.1(a)-(c)). Thus the total number of macro-collisions within any PIC cell is always equal to $\max(N_b, N_t)$. In our discussions, a macro-collision corresponds to the collision between macro-particles

in the simulation and a real collision corresponds to the collision between real physical particles.

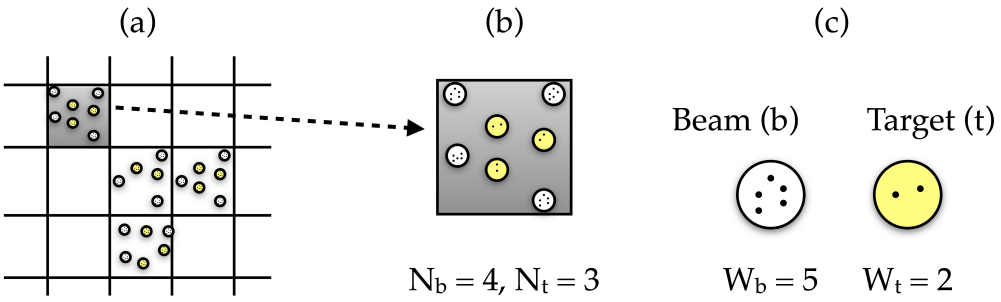

FIGURE 3.1: A schematic of Monte-Carlo pairing process. (a) Beam and target macro-particles are distributed in a 2D PIC grid. (b) Illustration of two example cells where different numbers of target and beam macro-particles are present. (c) The macro-particle pairing process when there are equal and unequal number of macro-particles of different species. The green background indicates macro-particle duplication. (d) An example of differently weighted beam and target macro-particle pair undergoing collision.

Specifically, let us analyse the macro-collision between a beam and target macro-particle with weight $W_b = 5$ and $W_t = 2$, i.e., each beam and target macro-particle represents five and two real physical particles respectively (Refer Figure 3.1(d)). In this case, the probability for a real beam particle to collide with a real target particle is 2/5, while the probability for a real target particle to collide with a real beam particle is 5/5. Thus during one macro-collision in this example, the number of real physical collisions experienced by beam and target macro-particle is

$$P_b = \frac{W_t}{\max(W_b, W_t)} \quad \text{and} \quad P_t = \frac{W_b}{\max(W_b, W_t)} \tag{3.4}$$

respectively. This implies, the macro-particle with the lower weight undergoes the correct number of collisions, while the other macro-particles experiences too many collisions. Now, the key idea is that the time increment experienced per real particle (beam or target) must be the same. This physical argument must hold during the simulation on average, i.e., the average time increment experienced by a beam and target particle must be the same. This is ensured by modifying the time increment experienced during each macro- collision by the beam and target macro-particle to $\Delta t_b = P_b \Delta t$ and $\Delta t_t = P_t \Delta t$ respectively. The average time increment experienced by the real beam or target particle is,

$$\overline{\Delta t_{b/t}} = \frac{\text{Number of colliding beam or target particles} \times \text{Time increment for each particle}}{\text{Total number of particles}} \tag{3.5}$$

The number of macro-particles colliding within a cell is $\max(N_b, N_t)$ which corresponds to $\max(N_b, N_t) \times W_b$ real beam particles and $\max(N_b, N_t) \times W_t$ real target particles.

The total number of real beam and target particles is

$$\begin{aligned} n_b &= N_b W_b \text{ and,} \\ n_t &= N_t W_t \end{aligned} \tag{3.6}$$

respectively. The average time increment per real beam particle is

$$\begin{aligned} \overline{\Delta t_b} &= \max(N_b, N_t) W_b \times \frac{P_b \Delta t}{N_b W_b} \\ &= \max(N_b, N_t) \times \frac{W_b W_t}{\max(W_b, W_t)} \frac{1}{n_b} \Delta t \\ &= \max(N_b, N_t) \times \frac{\min(W_b, W_t)}{n_b} \Delta t \\ &= \frac{n_{bt}}{n_b} \Delta t \end{aligned} \tag{3.7}$$

where $n_{bt} \equiv \max(N_b, N_t) \times \min(W_b, W_t)$ and the average time increment per real target particle is

$$\begin{aligned} \overline{\Delta t_t} &= \max(N_b, N_t) W_t \times \frac{P_t \Delta t}{N_t W_t} \\ &= \max(N_b, N_t) \times \frac{W_t W_b}{\max(W_b, W_t)} \frac{1}{n_t} \Delta t \\ &= \max(N_b, N_t) \times \frac{\min(W_b, W_t)}{n_t} \Delta t \\ &= \frac{n_{bt}}{n_t} \Delta t \end{aligned} \tag{3.8}$$

is kept to be equal to the simulation time-step, i.e., $\overline{\Delta t_b} = \overline{\Delta t_t} = \Delta t_{PIC}$. This ensures that we conserve energy and momentum on a large number of collisions, and we restore the symmetry of collisions between species with different numerical weights.

Hitherto, we have presented the basic Monte-Carlo algorithm required for the implementation of collisional processes inside a PIC code. In particular, we use this algorithm to implement bremsstrahlung emission and Bethe-Heitler pair production in the PIC code SMILEI. These two processes are discussed individually in the following sections.

The following notations are used henceforth:

- σ_{bs} is the total bremsstrahlung emission cross-section,
- σ_{pp} is the total Bethe-Heitler pair production cross-section,
- ε_γ is the photon energy,
- ε_{e^-} is the electron energy,
- ε_{e^+} is the positron energy,
- $\frac{\mathrm{d}\sigma_{bs}}{\mathrm{d}\varepsilon_\gamma}$ is the differential bremsstrahlung cross-section as a function of energy of the emitted photon,

- $\frac{d\sigma_{bs}}{d\varepsilon_{e+}}$ is the differential Bethe-Heitler pair production cross-section as a function of energy of the emitted positron,
- Z is the target nucleus atomic number, and
- $f(Z)$ is the Coulomb correction to the Born approximation worked out by Davies, Bethe, and L. Maximon, 1954:

$$\begin{aligned} f(Z) &= (\alpha Z)^2 \Sigma_{n=1}^{\infty} n(n^2 + (\alpha Z)) \\ &\approx 1.202(\alpha Z) - 1.0369(\alpha Z)^2 + 1.008\frac{(\alpha Z)^2}{(1 + (\alpha Z))} \end{aligned} \tag{3.9}$$

3.2 Bremsstrahlung emission in the ultra-relativistic regime

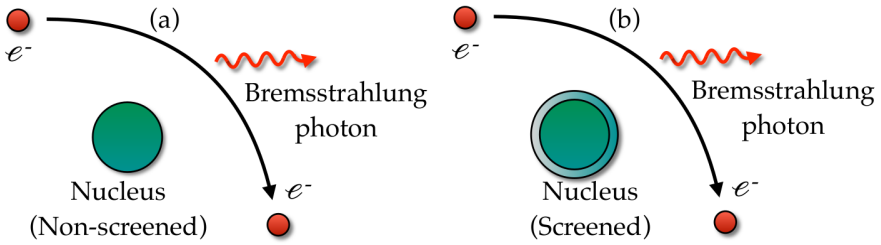

FIGURE 3.2: Bremsstrahlung emission in the field of an atomic nucleus which is (a) not screened (b) fully screened by the surrounding electrons.

During the collision of high energy electrons with an atomic nucleus, the electrons decelerate and lose a portion of their kinetic energy via bremsstrahlung photon emission. Calculations for predicting the bremsstrahlung radiation properties can be made by using cross-sections tabulated in the paper by Koch and Motz, 1959. The differential cross-sections in the ultra-relativistic regime in their paper have been derived by H. Olsen, L. C. Maximon, and Wergeland, 1957 and H. Olsen and L. C. Maximon, 1959. In general, the cross-section is proportional to the square of the target atomic number (Z^2). Depending on the extent of screening of the nuclear field by the surrounding electrons, the cross-section for bremsstrahlung emission varies. In the following subsections, we consider bremsstrahlung emission in the ultra-relativistic regime, i.e., when the initial and final electron energy, and outgoing photon energy is greater than the electron rest mass energy. We consider two limiting cases of screening, the non-screened and the completely screened nucleus bremsstrahlung cross-sections. For each of the above two considerations, we derive the cumulative cross-sections and provide some test results for showing the validity of the implementation.

3.2.1 Non-screened cross-section

The differential cross-section for bremsstrahlung emission without accounting for the screening effects is taken from Koch and Motz, 1959 (Eq. 3CN).

$$\frac{\mathrm{d}\sigma_{bs}}{\mathrm{d}\varepsilon_\gamma} = \frac{4Z^2\alpha r_0^2}{\varepsilon_\gamma}\left\{\left[1+\left(\frac{\varepsilon_{e^-}-\varepsilon_\gamma}{\varepsilon_{e^-}}\right)^2-\frac{2}{3}\frac{\varepsilon_{e^-}-\varepsilon_\gamma}{\varepsilon_{e^-}}\right]\left(\ln\left(\frac{2\varepsilon_{e^-}(\varepsilon_{e^-}-\varepsilon_\gamma)}{\varepsilon_\gamma}\right)-\frac{1}{2}-f(Z)\right)\right\} \tag{3.10}$$

where Z is the atomic number of the nuclei, α is the fine-structure constant and r_0 is the classical electron radius. The cumulative cross-section is obtained by integrating Eq. 3.10 with respect to the photon energy,

$$\begin{aligned}
\sigma_{bs} &= \int_{\varepsilon_{LPM}}^{\varepsilon_{e^-}-1}\frac{\mathrm{d}\sigma_{bs}}{\mathrm{d}\varepsilon_\gamma}\mathrm{d}\varepsilon_\gamma \\
&= \int_{\varepsilon_{LPM}}^{\varepsilon_{e^-}-1}\frac{c_0}{\varepsilon_\gamma}\left\{\left[1+\left(\frac{\varepsilon_{e^-}-\varepsilon_\gamma}{\varepsilon_{e^-}}\right)^2-\frac{2}{3}\frac{\varepsilon_{e^-}-\varepsilon_\gamma}{\varepsilon_{e^-}}\right]\left(\ln\left(\frac{2\varepsilon_{e^-}(\varepsilon_{e^-}-\varepsilon_\gamma)}{\varepsilon_\gamma}\right)-\frac{1}{2}-f(Z)\right)\right\}d\varepsilon_\gamma \\
&= \int_{\varepsilon_{LPM}}^{\varepsilon_{e^-}-1}\frac{c_0}{\varepsilon_\gamma}\left\{\left[1+\left(\frac{\varepsilon_{e^-}-\varepsilon_\gamma}{\varepsilon_{e^-}}\right)^2-\frac{2}{3}\frac{\varepsilon_{e^-}-\varepsilon_\gamma}{\varepsilon_{e^-}}\right]\left(\ln\left(\frac{2\varepsilon_{e^-}(\varepsilon_{e^-}-\varepsilon_\gamma)}{\varepsilon_\gamma}\right)-c\right)\right\}d\varepsilon_\gamma \\
&= \frac{1}{6\varepsilon_{e^-}^2}\Bigg[-8c\varepsilon_{e^-}^2\ln(\varepsilon_\gamma)+ \\
&\quad \ln(\frac{2\varepsilon_{e^-}(\varepsilon_{e^-}-\varepsilon_\gamma)}{\varepsilon_\gamma})(8\varepsilon_{e^-}^2\ln(\varepsilon_\gamma)-8\varepsilon_{e^-}\varepsilon_\gamma+3\varepsilon_\gamma^2) \\
&\quad +8\varepsilon_{e^-}^2\mathrm{Li}_2(\frac{\varepsilon_{e^-}}{\varepsilon_\gamma})-8\varepsilon_{e^-}^2\ln(\varepsilon_\gamma)\ln(1-\frac{\varepsilon_{e^-}}{\varepsilon_\gamma}) \\
&\quad +8\varepsilon_{e^-}^2\ln(\varepsilon_\gamma-\varepsilon_{e^-}) \\
&\quad +8\varepsilon_{e^-}c\varepsilon_\gamma-3\varepsilon_{e^-}\varepsilon_\gamma-3c\varepsilon_\gamma^2\Bigg]_{\varepsilon_{LPM}}^{\varepsilon_{e^-}-1}
\end{aligned} \tag{3.11}$$

where $c_0 = 4Z^2\alpha r_0^2$, $c = \frac{1}{2} - f(Z)$, and Li_2 is the dilogarithm function. We set a lower energy limit ε_{LPM} to account for Landau–Pomeranchuk–Migdal (LPM) effect (Migdal, 1956, Aurenche, Gelis, and Zaraket, 2000). The LPM effect is the suppression of the bremsstrahlung and pair production cross-sections at high energies or high matter densities due to interference effects from multiple-scattering sites.

Figure 3.3 shows the differential cross-section as a function of emitted bremsstrahlung photon energy obtained during the interaction of electrons with "bare" lead (Pb) nucleus for three different initial electron energies. In the plot, we show the data obtained via 10^7 photon emissions by the electrons and the corresponding analytical (Eq. 3.10) result. The figure shows that the obtained photon energy distribution matches very

well with the expected differential cross-section distribution function.

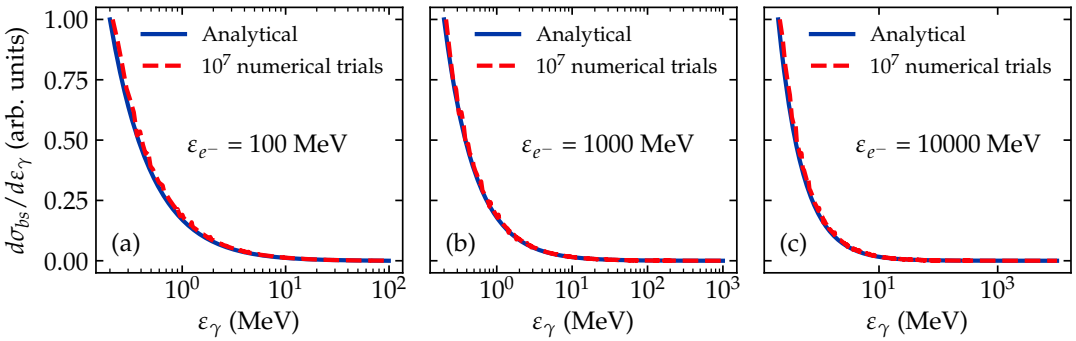

FIGURE 3.3: The bremsstrahlung photon energy distribution in the field of a completely screened nucleus obtained from numerical trials and corresponding analytical distribution function (Eq. 3.10).

We now illustrate the numerical validation of the implemented cross-section in the case of arbitrarily weighted macro-particles. We performed 2D test simulations where we consider the interaction of a mono-energetic electron beam with density $n_b = 1e^-/m^3$ through a neutral lead (Pb) target atom with electron density $n_e = 3.3 \times 10^{28} e^-/m^3$. At such low beam density, the collective plasma effects are negligible. For this test scenario, the expected theoretical number of photons is obtained from the relation between cross section and number of events,

$$\nu = \sigma_{bs} v_{rel} n_t n_b V t \tag{3.12}$$

where ν gives the number of events (macro photon emissions), v_{rel} is the relative velocity between two colliding particles, V is the volume of interaction (area in 2D simulations) and t is the time of interaction. We perform the tests for three different initial electron energies. The area of interaction is kept to be 0.1 μm^2. The number of target macro-particles is varied and the number of beam macro particles is kept constant to change the ratio of numerical weights W_t/W_b. W_t, W_b represent the target and beam macro-particle weights respectively. The results of these tests are given in Table 3.1. The simulation outcomes (macro-particle emissions) match very closely with the expected theoretical result.

$\frac{W_t}{W_b}$	ν (theory)	ν (computation) Trial 1	Trial 2	Trial 3
k	6679	6678	6732	6620
$2k$	6679	6701	6724	6699
$\frac{k}{2}$	6679	6663	6560	6773

TABLE 3.1: Validation of non-screened bremsstrahlung module for arbitrarily weighted macro-particles. ν is the number of macro photon emissions obtained during the collision of an electron beam with energy $\varepsilon_- = 100$ MeV on neutral lead atoms (k is a constant).

3.2.2 Completely screened cross-section

The formula (equation 3.10) used in the previous section is accurate when the incoming electron sees the nuclear field from distances smaller than the radius of the K-shell of the atom. At greater distances the field of the nucleus is partially or completely screened by the field of the atomic electrons. The differential cross-section for bremsstrahlung emission by considering complete screening of the nuclear field by the atomic electrons is tabulated in Koch and Motz, 1959 and is also available in Tsai, 1974 as,

$$\frac{\mathrm{d}\sigma_{bs}}{\mathrm{d}\varepsilon_\gamma} = \frac{4Z^2\alpha r_0^2}{\varepsilon_\gamma}\left\{\left[1+\left(\frac{\varepsilon_- - \varepsilon_\gamma}{\varepsilon_-}\right)^2 - \frac{2}{3}\frac{\varepsilon_- - \varepsilon_\gamma}{\varepsilon_-}\right]c_0(Z) + \frac{1}{9}\frac{\varepsilon_- - \varepsilon_\gamma}{\varepsilon_-}\right\} \tag{3.13}$$

where $c_0(Z) = \ln(183Z^{-1/3}) - f(Z)$.
In order to compute the probability for emitting a bremsstrahlung photon, we obtain the cumulative cross-section by integrating Eq(3.13):

$$\begin{aligned}\sigma_{bs} &= \int_{\varepsilon_\gamma^*}^{\kappa_0} \mathrm{d}\varepsilon_\gamma \frac{\mathrm{d}\sigma_{bs}}{\mathrm{d}\varepsilon_k} \\ &= 4Z^2\alpha r_0^2\left\{\left(\frac{4c_0(Z)}{3}+\frac{1}{9}\right)\left[\ln\left(\frac{\kappa_0}{\varepsilon_\gamma^*}\right) - \frac{\kappa_0 - \varepsilon_\gamma^*}{\varepsilon_-}\right] + \frac{c_0(Z)}{2\varepsilon_-^2}(\kappa_0^2 - \varepsilon_\gamma^{*2})\right\}\end{aligned} \tag{3.14}$$

Similar to the non-screened bremsstrahlung emission scenario, we perform tests to verify the implemented cumulative cross-section for different initial electron energies. The electron beam now interacts with a "screened" lead (Pb) nucleus. In Figure 3.4, we present the differential cross-section as a function of emitted bremsstrahlung photon energy. We show the data obtained via 10^7 photon emissions by the electrons and the corresponding analytical (Equation 3.14) result. From the figure, it is evident that the obtained photon energy distribution matches closely with the expected differential cross-section distribution function.

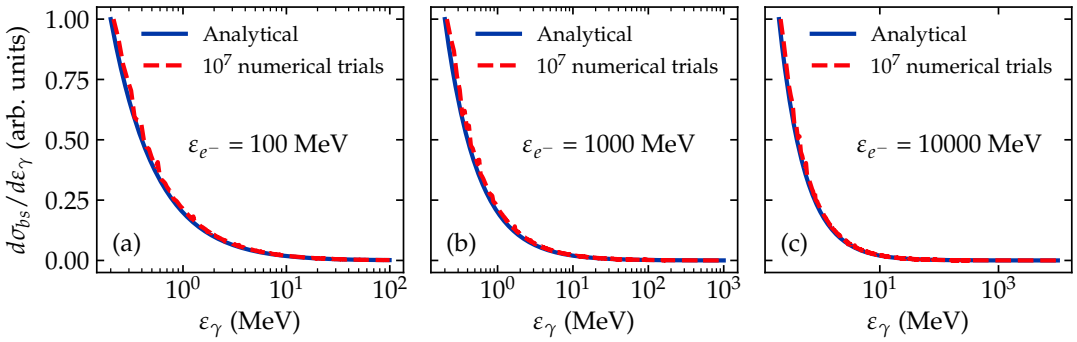

FIGURE 3.4: The bremsstrahlung photon energy distribution in the field of a completely screened nucleus obtained from numerical trials and corresponding analytical distribution function (Equation 3.14).

To elucidate the validity of the completely screened bremsstrahlung module to handle arbitrarily weighted macro-particles, we perform the same 2D test simulations as done in the previous section, but with a fully screened lead target nucleus. The theoretical number of outcomes (macro photon emissions) were obtained from Equation 3.12. The results of the tests are tabulated in table 3.2. The obtained number of macro-particle emissions match very closely with the expected theoretical results for different macro-particle weight ratios.

$\frac{W_t}{W_b}$	ν (theory)	ν (computation) Trial 1	Trial 2	Trial 3
k	6679	6674	6727	6646
$2k$	6679	6569	6742	6733
$\frac{k}{2}$	6679	6676	6580	6765

TABLE 3.2: Validation of completely screened bremsstrahlung module for arbitrarily weighted macro-particles. ν is the number of macro photon emissions obtained during the collision of an electron beam with energy $\varepsilon_- = 100$ MeV on neutral lead atoms (k is a constant).

3.2.3 Screening Effects

To understand importance of screening effects, we show in Figure 3.5, the non-screened and fully screened bremsstrahlung cross-section as a function of ultra-relativistic initial electron energies in the presence of different target nuclei (lead (Pb) with Z= 82 and aluminium (Al) with Z= 13). The first conclusion seen in the figure is that cross-section is two orders more in Pb in comparison to Al nuclei. This is expected from to the Z^2 dependence of the cross-section. Secondly, as screening effects reduce the strength of the nuclear field, the completely screened cross-sections values are always lower than the non-screened cross-sections. This will result in the reduction of effective number of electron-nucleus collisions, consequently leading to a reduced bremsstrahlung photon yield. This trend is consistent with both lead and aluminium nuclei. The difference between the two limiting cross-sections for a particular target nuclei is present for electron energies greater than 50 MeV and increases with the increase in initial electron energy.

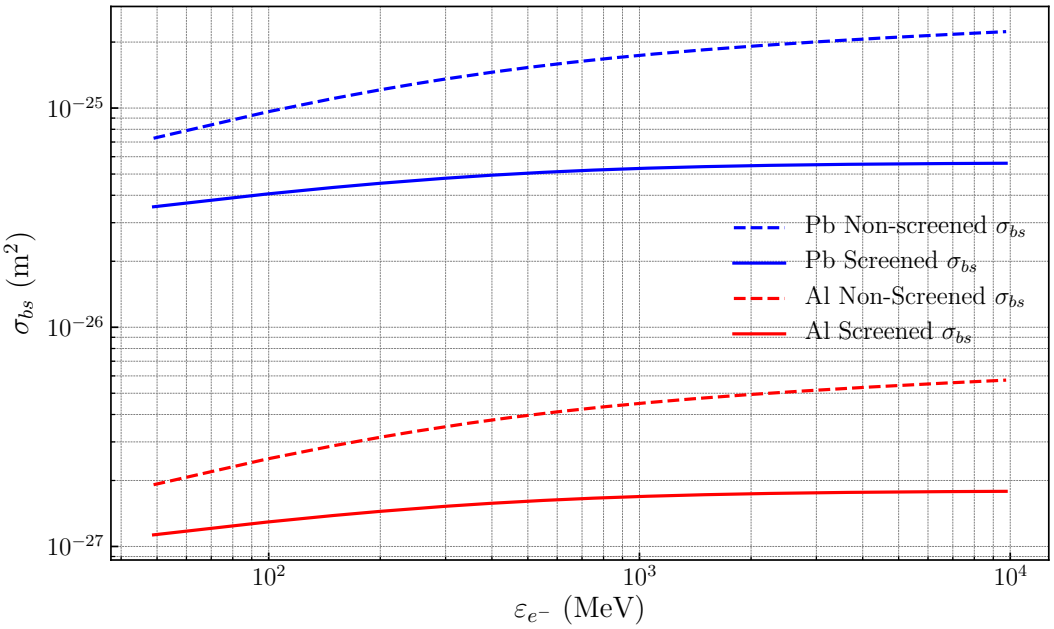

FIGURE 3.5: The completely screened and non-screened cross-section for lead (Pb) and aluminium (Al) nucleus.

As a final check, we compare the results from our module implemented in SMILEI with the bremsstrahlung module in a different particle-in-cell code, EPOCH (Arber et al., 2015). Their routines are based on the algorithm used in the Monte-Carlo code PENELOPE (Salvat, Fernández-Varea, Sempau, et al., 2008). It was implemented by Vyskočil, Ondřej Klimo, and Weber, 2018. They use cross-sections tabulated by Seltzer and Berger, 1985.

We let a bunch of 500 MeV electrons with density = $10^{19} e^-/m^3$ propagate through bulk neutral Au target for approximately 30 fs. From the Figure 3.6, we can see that the photon distributions from both the codes agree very well. The results from EPOCH match better with the completely screened cross-section. As discussed previously in Figure 3.5, the non-screened cross-section over estimates the probability of bremsstrahlung photon emission.

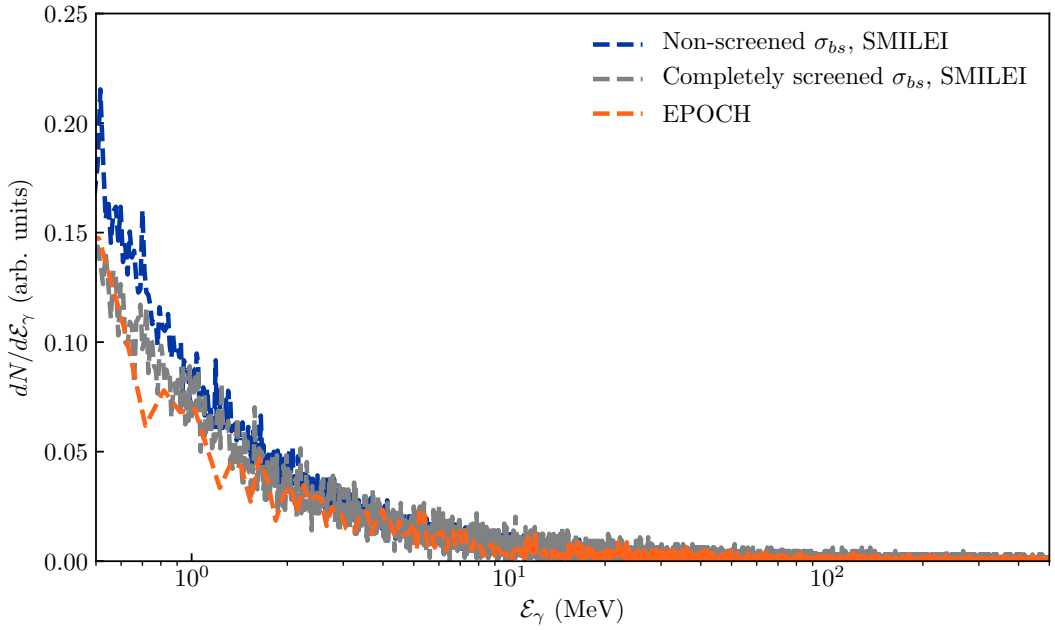

FIGURE 3.6: Comparison of photon spectra of bremsstrahlung radiation generated by a 500MeV electron bunch propagating through an Au target for 30 fs from a PIC simulations.

Hitherto we presented the obtained cumulative cross-section for bremsstrahlung emission for the two extreme limits of nuclear field screening. We compared the simulation outcomes with the expected theoretical results and benchmarked the module. We also analysed at which initial electron energy range one can expect the effect of screening to be significant for bremsstrahlung emission.

3.3 Bethe-Heitler pair production in the ultra-relativistic regime

We now discuss the creation of electron-positron pairs by a photon in the field of atomic nucleus, the Bethe-Heitler pair production. The calculations for predicting the properties of created pairs can be made by using the cross- sections tabulated in the paper by Motz, H. A. Olsen, and Koch, 1969. We use the differential cross-sections in the ultra-relativistic regime. Analogous to bremsstrahlung emission, the Bethe-Heitler pair production cross-section also grows fast with the atomic number of the target nuclei due to the Z^2 dependence. The effect of screening of nuclear field is discussed again in the two limiting cases; the non-screened and the fully screened field of the nucleus.

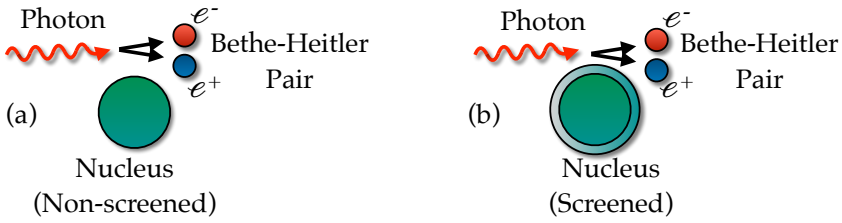

FIGURE 3.7: Bethe-Heitler pair production in the field of an atomic nucleus which is (a) not screened (b) screened by the surrounding electrons.

3.3.1 Non-screened cross-section

The differential pair production cross-section integrated over angles is provided by Davies, Bethe, and L. Maximon, 1954 which corresponds to Formula 3D-1007 from Motz, H. A. Olsen, and Koch, 1969.,

$$\begin{aligned}\frac{\mathrm{d}\sigma_{pp}}{\mathrm{d}\varepsilon_+} &= 2\frac{Z^2\alpha^3}{m^3}\frac{1}{\varepsilon_\gamma^3}(\varepsilon_+^2+\varepsilon_-^2+\frac{2}{3}\varepsilon_+\varepsilon_-)(2\ln\frac{2\varepsilon_+\varepsilon_-}{m\varepsilon_\gamma}-1-2f(Z))\\ \frac{\mathrm{d}\sigma_{pp}}{\mathrm{d}\varepsilon_+} &= 4Z^2\alpha r_0^2\frac{1}{\varepsilon_\gamma^3}(\varepsilon_+^2+\varepsilon_-^2+\frac{2}{3}\varepsilon_+\varepsilon_-)(\ln\frac{2\varepsilon_+\varepsilon_-}{m\varepsilon_\gamma}-\frac{1}{2}-f(Z))\end{aligned} \tag{3.15}$$

Total cross-section integrated over all photon energies without screening is given by

$$\sigma_{pp} = \frac{28}{9}Z^2\alpha r_e^2[\ln(\frac{2\omega}{m})-\frac{109}{42}-f(Z\alpha)] \tag{3.16}$$

By using the differential cross-section, one obtains the cumulative cross-section as follows:

$$\begin{aligned}\sigma_{pp} &= \int_{mc^2}^{\varepsilon_\gamma-mc^2}\frac{\mathrm{d}\sigma_{pp}}{\mathrm{d}\varepsilon_+}\mathrm{d}\varepsilon_+\\ &= \int_{mc^2}^{\varepsilon_\gamma-mc^2}\frac{4Z^2\alpha r_0^2}{\varepsilon_\gamma^3}(\varepsilon_+^2+(\varepsilon_\gamma-\varepsilon_+)^2+\frac{2}{3}\varepsilon_+(\varepsilon_\gamma-\varepsilon_+))(\ln\frac{2\varepsilon_+(\varepsilon_\gamma-\varepsilon_+)}{\varepsilon_\gamma}-\frac{1}{2}-f(Z))\mathrm{d}\varepsilon_+\\ &= \int_{mc^2}^{\varepsilon_\gamma-mc^2}\frac{C}{\varepsilon_\gamma^3}(\varepsilon_+^2+(\varepsilon_\gamma-\varepsilon_+)^2+\frac{2}{3}\varepsilon_+(\varepsilon_\gamma-\varepsilon_+))(\ln\frac{2\varepsilon_+(\varepsilon_\gamma-\varepsilon_+)}{\varepsilon_\gamma}-c)\mathrm{d}\varepsilon_+\\ &= \frac{C}{27\varepsilon_\gamma^3}\Bigg[3\varepsilon_+\ln\left(\frac{2\varepsilon_+(k-\varepsilon_+)}{\varepsilon_\gamma}\right)(9\varepsilon_\gamma^2-6\varepsilon_\gamma\varepsilon_++4\varepsilon_+^2)-21k^3ln(\varepsilon_+-k)\\ &\quad-(4\varepsilon_+^3-6kx^2)(2+3c)-3k^2\varepsilon_+(16+9c)\Bigg]_{mc^2}^{k-mc^2}\end{aligned} \tag{3.17}$$

where $C = 4Z^2\alpha r_0^2$ and $c = \frac{1}{2}+f(Z)$.

In Figure 3.3, we show the non-screened Bethe-Heitler pair production differential cross-section as a function of created positron energy. In particular we show the data obtained via 10^7 pair creations obtained during the interaction of high energy photons with "bare" lead (Pb) nucleus for three different initial photon energies. We also plot the corresponding analytical (Equation 3.17) function. We see that the numerical and analytical distributions match closely.

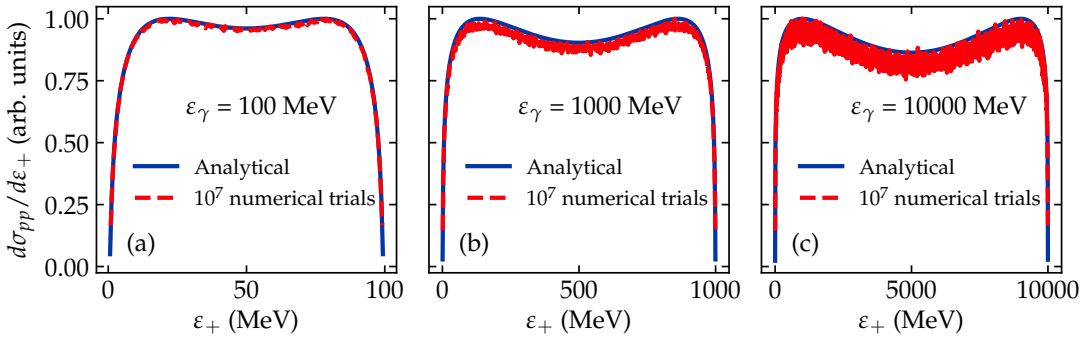

FIGURE 3.8: Differential cross-section for non-screened pair production obtained from numerical conversions and corresponding analytical result.

We perform 2D test simulations with a "bare" lead target, and compare the obtained number of pairs with the expected outcomes. The test simulation consisted of a photon beam with density $n_\gamma = 10^{20}/m^3$, target electron density $n_e = 3.3 \times 10^{28} e^-/m^3$, an interaction volume (area in 2D) of 0.1 m^{-2} and an interaction time of ~ 0.6 fs.

$$\nu = \sigma_{pp} v_{rel} n_t n_b V t \tag{3.18}$$

The theoretical number of outcomes (macro photon emissions) were obtained using Equation 3.18. The results of the tests are tabulated in Table 3.2. The obtained number of macro-particle pairs match very closely with the expected theoretical results for different macro-particle weight ratios.

$\frac{W_t}{W_b}$	ν (theory)	ν (computation) Trial 1	Trial 2	Trial 3
k	611	620	650	642
$2k$	611	636	676	652
$\frac{k}{2}$	611	592	665	593

TABLE 3.3: Validation of non-screened Bethe-Heitler pair production module for arbitrarily weighted macro-particles. ν is the number of macro electron/positron particles created during the collision of a photon beam with energy $\varepsilon_\gamma = 100$ MeV on neutral lead atoms (k is a constant).

3.3.2 Completely screened cross-section

If we take nuclear field screening into consideration, the cross-section for Bethe-Heitler production (Formula 3D-1009 in Motz, H. A. Olsen, and Koch, 1969,Akhiezer and Berestetskii, 1986) is available in the literature as,

$$\frac{\mathrm{d}\sigma_{pp}}{\mathrm{d}\varepsilon_+} = \frac{4\alpha Z^2 r_0^2}{\varepsilon_\gamma^3}\left((\varepsilon_+^2+\varepsilon_-^2+\frac{2}{3}\varepsilon_+\varepsilon_-)\left[\ln(183Z^{-1/3}-f(Z)\right] + \frac{1}{9}\varepsilon_+\varepsilon_-\right) \tag{3.19}$$

In the case of complete screening, the total cross-section

$$\sigma_{pp} = \frac{28}{9}Z^2\alpha r_e^2[\ln(183Z^{-1/3}) - \frac{1}{42} - f(Z\alpha)]. \tag{3.20}$$

It is pertinent to note that the total cross-section is independent of the incoming photon energy and solely depends on the atomic number of the target material. The corresponding cumulative cross-section

$$\begin{aligned}\sigma_{pp} = \left(\frac{4c_1c_2}{3}-\frac{c_1}{9}\right)\left(\frac{\varepsilon_{+,max}^3-\varepsilon_{+,min}^3}{3}\right) \\ +\left(\frac{-4\varepsilon_\gamma c_1c_2}{3}+\frac{c_1\varepsilon_\gamma}{9}\right)\left(\frac{\varepsilon_{+,max}^2-\varepsilon_{+,min}^2}{2}\right)+c_1c_2\varepsilon_\gamma^2(\varepsilon_{+,max}-\varepsilon_{+,min}) \\ \varepsilon_\gamma = \varepsilon_- + \varepsilon_+\end{aligned} \tag{3.21}$$

where $c_1 = \frac{4\alpha Z^2 r_0^2}{k^3}$, c_2 =ln(183$Z^{-1/3}$) - f(Z) , k= ε_γ.

Similar to the previous sections, the results obtained in Figure 3.9 and Table 3.4 elucidate the validity of the implemented Bethe-Heitler pair production cross-section.

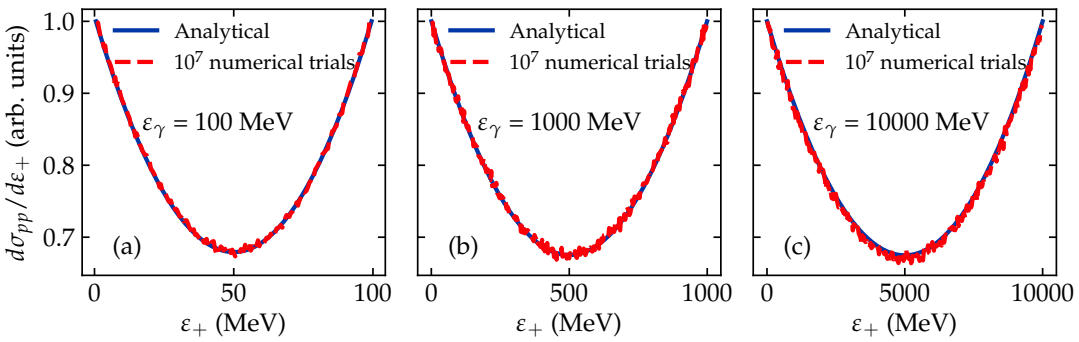

FIGURE 3.9: Differential cross-section for screened pair production obtained from numerical conversions and corresponding analytical result.

$\frac{W_t}{W_b}$	ν (theory)	ν (computation) Trial 1	Trial 2	Trial 3
k	667	669	676	659
$2k$	667	677	671	667
$\frac{k}{2}$	667	679	658	660

TABLE 3.4: Validation of completely screened Bethe-Heitler pair production module for arbitrarily weighted macro-particles. ν is the number of macro electron/positron particles created during the collision of a photon beam with energy $\varepsilon_\gamma = 100$ MeV on neutral lead atoms (k is a constant).

3.3.3 Screening effects

To examine the importance of screening effects, we plot the fully screened and the non-screened cross-section as a function of target nuclei atomic number for different initial photon energies in Figure 3.10. For photon energies around 100 MeV, we see that the difference between the two cross-sections is not relatively significant for all values of Z. As we increase the initial photon energies to 1 or 10 GeV, one can notice that the difference between non-screened and fully screened cross-section increases sharply for high Z materials. Hence depending on the setup, we may not be able to ignore the effect of screening, although the possibility of full ionization in high Z materials is slim.

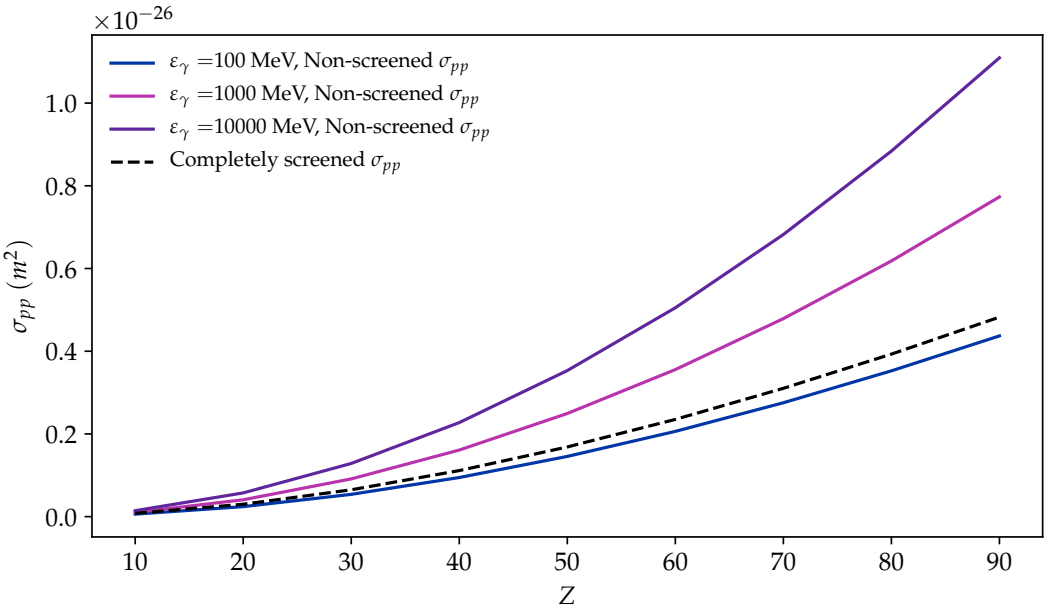

FIGURE 3.10: Variation of non-screened and completely screened cross-section σ (m^2) with atomic number Z and photon energy ε_γ.

3.4 Conclusion

In conclusion, we briefly presented the Monte-Carlo algorithm used to model collisional radiation and pair production processes. The numerical implementation was validated through comparison with theoretical predictions. To analyse the effect of nuclear field screening by the surrounding electrons, we implemented the bremsstrahlung emission and Bethe-Heitler pair production in the two limiting cases of screening, the non-screened and completely screened nucleus. We conclude that for both bremsstrahlung emission and Bethe-Heitler pair production in the field of high Z nucleus, the difference between non-screened and completely screened cross-section is significant when the incoming electron energy or photon energy is greater than 50 MeV or 1 GeV respectively.

In electron-beam plasma or laser-beam plasma interactions, although various degrees of ionisation is achieved by the plasma ions, the possibility of full ionisation of the target material is slim. In conclusion, the models presented until now cannot be considered fully complete and have some limitations. One can also implement these processes to ensure that all ranges of incoming electron or photon energies are discussed in the thesis of Martinez, 2018.

In the following chapter, we use this enriched version of particle-in-cell code SMILEI, in particular the completely screened nuclear cross-sections, to study the interaction of an ultra-relativistic electron beam with a thin conducting aluminium foil.

Chapter 4

Extremely Dense Gamma-Ray Beams in Electron-Conductor Collision

We propose a method for the efficient generation of gamma photons through the interaction of an ultra-relativistic electron beam with multiple conducting foils. The electron beam undergoes strong self-focusing and emits hard photons that originate from the beam interaction with the near-field transition radiation accompanying the beam-foil collision. This near field radiation is of an amplitude comparable with the beam self-field, and can be strong enough such that a single emitted photon can carry away a significant fraction of the emitting electron energy. Approximate analytic models and fully 3D particle-in-cell simulations were used to explore the dynamics of the electron beam and the emitted radiation during this interaction. This principle could be employed for constructing a dense collimated femtosecond photon source and also for strong-field QED investigations. The relatively simple model in this work along with the outcomes arising out it aids in extending the boundaries of fundamental and applied research. The key results of this chapter have been submitted for publication and available online in arXiv (Sampath, Davoine, et al., 2020).

4.1 Introduction

In this chapter we study the interaction of an ultra-relativistic electron beam with a thin conducting foil which aids in the generation of a dense photon beam. The basic idea of our setup stems from the fact that a conductor in the vicinity of an electron beam acts like a lens that focuses the beam via image charges. The beam in the presence of this focusing field emits copious amount of photons. This mechanism of electron beam focusing and photon emission can be enhanced by using a series of thin conducting foils. This approach of placing periodic array of foils transverse to the beam propagation axis were studied in the realm of particle accelerators (Adler, 1982, Stanley Humphries,

1983, Humphries Jr and C. B. Ekdahl, 1988, S. Humphries, C. Ekdahl, and Woodall, 1989, Fernsler, Hubbard, and Slinker, 1990).

This chapter is organised as follows. In Sec 4.2, we briefly present the approximate equations for the self-fields of an ultra-relativistic electron beam in vacuum. In Sec 4.3, we discuss the key consequences, i.e, the electron beam self-focusing and synchrotron-like emission that arises during the collision of an ultra-relativistic beam with a perfect conductor (aluminium). Using the method of images, in Sec 4.4 we derive approximate equations for predicting the dependence of total radiated energy on various beam parameters. In Sec 4.5 we present the 2D simulations results. We investigate the scalings of radiated energy with respect to the electron beam parameters such as the beam radius, the beam shape and the beam energy. We extend the study by investigating the collision of the electron beam with multiple aluminium foils. In Sec 4.6 we show 3D simulations results in which we analyse the effect of beam radius, length and shape on the radiated energy and also illustrate the results of electron beam collision with multiple foils.

4.2 Beam self-fields and equations of motion

Let us consider a cold ultra-relativistic bunch of charged particles with a gaussian density distribution ρ centred at x_0. Let us suppose that the bunch propagates in vacuum with velocity $\boldsymbol{v} = c\boldsymbol{\beta}$ and with Lorentz factor γ along $\hat{x}$. We assume that the bunch has cylindrical symmetry around the propagation axis $\hat{x}$. Hence it is convenient to approach the problem in cylindrical coordinates (r, θ, x) with $r = \sqrt{y^2 + z^2}$, $\theta = \arctan(y/z)$ and x being the radial, azimuthal and vertical directions respectively. As a result of cylindrical symmetry, only the radial and longitudinal components of the electric field (E_r and E_x) and the azimuthal components of the magnetic field (B_θ) are different from zero ($E_\theta = B_r = B_x = 0$).

The solutions to the electron beam self-fields can be obtained by solving the Maxwell equations in vacuum.

$$\begin{aligned} \nabla \cdot \boldsymbol{B}^b &= 0 \\ \nabla \cdot \boldsymbol{E}^b &= 4\pi\rho^b \\ \nabla \times \boldsymbol{E}^b &= -\frac{1}{c}\frac{\partial \boldsymbol{B}^b}{\partial t} \\ \nabla \times \boldsymbol{B}^b &= \frac{1}{c}\frac{\partial \boldsymbol{E}^b}{\partial t} + \frac{4\pi}{c}\boldsymbol{j}^b \end{aligned} \tag{4.1}$$

where the superscript b corresponds to "beam" and $\boldsymbol{j}^b = \rho^b \boldsymbol{v} = \rho^b v \hat{\boldsymbol{x}}$.
As a result of imposing cylindrical symmetry, Gauss's law for magnetic fields is directly fulfilled.

From the Faraday's law of induction,

$$\begin{aligned}
\nabla \times \boldsymbol{E}^b &= -\frac{1}{c}\frac{\partial \boldsymbol{B}^b}{\partial t} \\
\left(\frac{\partial E_r}{\partial x} - \frac{\partial E_x}{\partial r}\right) &= -\frac{1}{c}\frac{\partial B_\theta^b}{\partial t} \\
&= \frac{v}{c}\frac{\partial B_\theta^b}{\partial x} = \frac{v^2}{c^2}\frac{\partial E_r^b}{\partial x} \\
\left(\frac{\partial E_r}{\partial x} - \frac{\partial E_x}{\partial r}\right) &= \left(1 - \frac{1}{\gamma^2}\right)\frac{\partial E_r^b}{\partial x} \\
\frac{\partial E_x}{\partial r} &= \frac{1}{\gamma^2}\frac{\partial E_r^b}{\partial x}
\end{aligned} \tag{4.2}$$

where we have used the assumption that for a cold electron beam $\boldsymbol{B} = \beta \times \boldsymbol{E}$ which implies $B_\theta = vE_r/c$.
From the radial component of Maxwell-Ampere's law,

$$\frac{1}{c}\frac{\partial E_r^b}{\partial t} = -\frac{v}{c}\frac{\partial E_r^b}{\partial x} = -\frac{\partial B_\theta^b}{\partial x} \tag{4.3}$$

and the corresponding simplification of the vertical component gives the Gauss's law for electric fields,

$$\begin{aligned}
\frac{1}{c}\frac{\partial E_x^b}{\partial t} &= \frac{1}{r}\frac{\partial}{\partial r}(r\frac{v}{c}E_r^b) - 4\pi\frac{v}{c}\rho^b \\
\implies -\frac{\partial E_x^b}{\partial x} &= \frac{1}{r}\frac{\partial}{\partial r}(rE_r^b) - 4\pi\rho^b \\
\implies \frac{\partial E_x^b}{\partial x} &+ \frac{1}{r}\frac{\partial}{\partial r}(rE_r^b) = 4\pi\rho^b \\
&\equiv \nabla \cdot \boldsymbol{E}^b = 4\pi\rho^b.
\end{aligned} \tag{4.4}$$

Thus, the relevant equations to be satisfied for the beam fields are:

$$\boxed{\begin{aligned}
&\frac{1}{c}\frac{\partial E_r^b}{\partial t} = -\frac{\partial B_\theta^b}{\partial x} \\
&\frac{\partial E_x^b}{\partial r} + \frac{1}{r}\frac{\partial}{\partial r}(rE_r^b) = 4\pi\rho^b \\
&\frac{\partial E_x^b}{\partial r} = \frac{1}{\gamma^2}\frac{\partial E_r^b}{\partial x}
\end{aligned}} \tag{4.5}$$

From the above equation, for electron beams with energy in the order of few hundred MeV, the resultant γ factor becomes large, and the longitudinal electric field component can be safely neglected in comparison to the radial electric field ($E_x^b \ll E_r \sim 0$ when $\gamma >> 1$). Thus, this indicates that the resultant electron beam self-fields are confined in a disk perpendicular to the direction of propagation of the beam.

In addition, for ultra-relativistic beams magnitude the net defocusing transverse force,

$$\begin{aligned} \boldsymbol{f}_\perp &= e(\boldsymbol{E}_\perp + \boldsymbol{\beta} \times \boldsymbol{B}) \\ &= e\boldsymbol{E}_\perp/\gamma^2 \end{aligned} \tag{4.6}$$

is suppressed by a factor of $1/\gamma^2$ resulting in the ballistic propagation of the beam for large distances.

An approximate solution of the beam self-fields for ultra-relativistic beams with $\gamma \gg 1$ can be obtained by modulating the uniform longitudinal density solution. For an electron beam with Gaussian charge distribution ($\rho^b \equiv \rho$) with N_e particles, RMS beam length $\sigma_\parallel$, RMS beam radius $\sigma_\perp$, initial position x_0, and velocity v along x,

$$\rho(x, r, t) = \frac{eN_e}{2\sqrt{2}\pi^{3/2}\sigma_\perp^2\sigma_\parallel} \exp(\frac{-r^2}{2\sigma_\perp^2}) \exp\left(\frac{-(x - x_0 - vt)^2}{2\sigma_\parallel^2}\right) \tag{4.7}$$

the corresponding self-fields are given by,

$$\begin{aligned} E_r^b(r, x, t) &= \frac{2eN_e}{\sqrt{2\pi}\sigma_\parallel}\frac{1}{r}\left(1 - \exp(\frac{-r^2}{2\sigma_\perp^2})\right) \exp\left(\frac{-(x - x_0 - vt)^2}{2\sigma_\parallel^2}\right) \\ E_x^b &= 0 \\ B_\theta^b &= \frac{v}{c}E_r^b(r, x, t) \end{aligned} \tag{4.8}$$

where the subscripts $\perp$ and $\parallel$ denote the vector components perpendicular and parallel to v, respectively. The beam field Equations 4.8 provide an approximate solution to Maxwell equations up to terms of order γ^{-2} around the beam. Having obtained the electron beam self-fields in vacuum, we move on to discuss the presence of a perfect conductor in the vicinity of this beam.

4.3 Collision with a conductor foil

When the self-fields of the electron beam encounter an conductor (foil), the surface currents and charge densities are excited at the boundary, leading to the emission of coherent transition radiation. One can understand the basic physics behind this radiation via either virtual (pseudo) photon method or via the method of images. In the former method, the electron beam self-fields are considered to be made of virtual photons that are then converted into real photons via reflection at the electron beam-foil boundary. On the other hand, in the method of images, the electron beam is visualised as colliding with it's own image that is present on the other side of the conductor. When the real electron beam and the image electron beam reach the foil boundary, they "annihilate" and generate photons.

We employ the latter method of images to obtain approximate analytical expressions for the final radiated energy during the electron beam-foil collision. A schematic of the well-established image charge method is given in Figure 4.1.

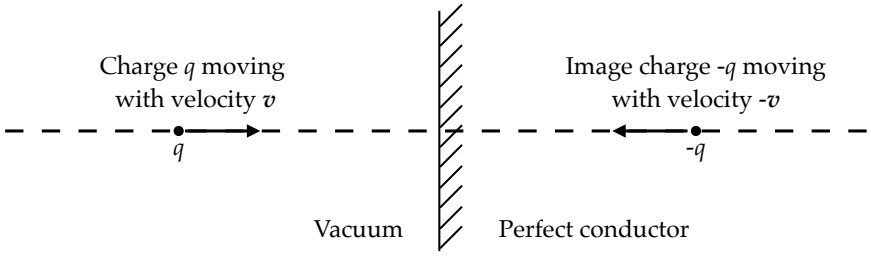

FIGURE 4.1: A charge q colliding with its image charge $-q$ at the boundary of vacuum and a perfect conductor.

The prerequisite for employing this method is that the boundary must be a flat surface with infinite conductivity. The method of images then takes advantage of the fact that the tangential electric field at the boundary of a perfect conductor vanishes. This enforces a change in sign of the beam and the image charge electric fields, i.e., $E_r^{image}(r,0,t) = -E_r^b(r,0,t)$ In addition, as electromagnetic energy cannot penetrate a perfect conductor, it is necessary that the Poynting vector of the image beam is equal and opposite to that of the real electron beam

$$\frac{c}{4\pi}\boldsymbol{E}^b \times \boldsymbol{B}^b = -\left(\frac{c}{4\pi}\boldsymbol{E}^{image} \times \boldsymbol{B}^{image}\right). \tag{4.9}$$

This condition can be attained if the transverse magnetic field of both the real beam and the image beam is of the same sign, i.e., $B_\theta^{image}(r,0,t) = B_\theta^b(r,0,t)$ at the boundary. In other words, the beam fields collide with its reflected self-fields at the boundary.

Hence, within these constraints, we consider the collision of the ultra-relativistic electron beam and a flat perfect conductor with it's front surface at $x = 0$ as shown in Figure 4.2. In particular, we use the method of images to find the conductor fields, i.e, the fields generated at the surface of the conductor during collision (Hammond, 1960). In the following, the superscript c denotes "conductor".

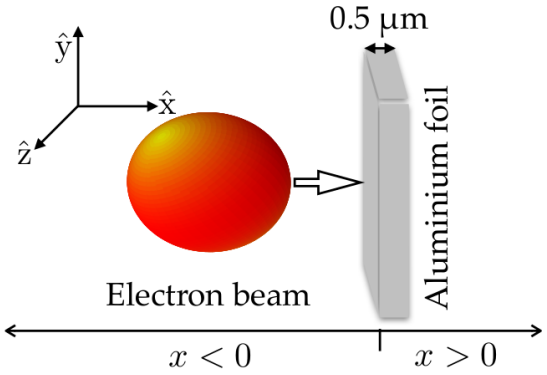

FIGURE 4.2: Schematic setup of an electron beam interaction with a conductor (Al) foil

The conductor fields $(\boldsymbol{E}^c, \boldsymbol{B}^c)$ satisfy source-free Maxwell equations outside the conductor in the region $x < 0$.

It is pertinent to note that the method of images cannot be applied when the beam enters the foil, because the image would be located in ($x < 0$ region), where conductor fields must satisfy source-free Maxwell equations. However, we use this reflected field model obtained via method of images to obtain the total fields at the boundary at all times, i.e., even when the electron beam penetrates the target foil. This could be considered reasonable due to the fact that in all our simulations the beam length is not much greater than the beam radius, i.e., $\sigma_\parallel \ll \sigma_\perp$. In this regime, the "reflected beam" approximation holds because the emitted radiation, i.e., coherent transition radiation, which has a transverse size $\sigma_\perp$ and typical wavelength $\sigma_\parallel$, undergoes weak diffraction over a Rayleigh length of approximately $\sigma_\perp^2/\sigma_\parallel \gg \sigma_\parallel$ from the boundary.

To further elucidate this, we show in Figure 4.3 the beam density ρ and radial electric field profile E_r as a function of the radial distance r. The source of the fields, i.e, the beam particles are majorly located at the region $r = 0$, while the peak radial field is approximately reached at $r \approx 1.5\sigma_\perp$. Thus, when $\sigma_\perp \gg \sigma_\parallel$, during the collision of the beam with the conducting foil, the current neutralisation effects do not have sufficient time to propagate from the central region of the beam, where most of the beam particles that are the sources of the field are located, to the region $r \approx 1.5\sigma_\perp$ where the fields are stronger. In this case, the reflected beam fields approximation holds because the longitudinal extent of the radiation is $\sigma_\perp^2/\sigma_\parallel$ and it is greater than $\sigma_\parallel$ when $\sigma_\perp \gg \sigma_\parallel$, i.e., the non-stationary case.

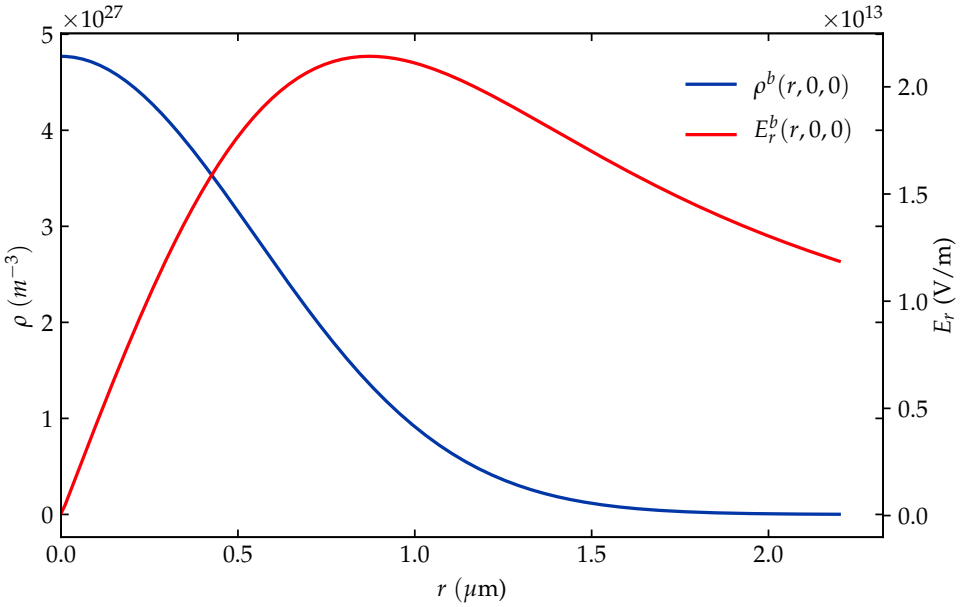

FIGURE 4.3: The radial dependence of beam density and transverse electric field.

On the other hand, when $\sigma_\perp \ll \sigma_\parallel$, fields weakly change in time close to the conductor surface and have relaxed to their stationary values for most of the interaction. This stationary limit implies that magnetic and electric fields in Maxwell's equations decouple. This corresponds to the magnetostatic approximation, yielding a vanishing B_θ^c

and a surface-localised E_r^c. B_θ^b of an ultra-relativistic beam are determined by the electron beam density per unit length $N/\sigma_\parallel$ (refer Equation 4.8), and are approximately invariant if part of the beam is removed (e.g., if $N \to N/2$ and $\sigma_\parallel \to \sigma_\parallel/2$). This is rigorously true for $\sigma_\parallel/\sigma_\perp \to \infty$ and to very good accuracy if the beam with $\sigma_\parallel \gg \sigma_\perp$ is ultra-relativistic. Thus the boundary conditions are approximately time independent and $B_\theta \approx B_\theta^b$. In this stationary field model, field imbalance basically arises purely from the uncompensated beam magnetic field that extends longitudinally within a region $\sigma_\perp$.

The Maxwell equations for the conductor in $x < 0$ source-free region are:

$$\begin{aligned} \nabla \cdot \boldsymbol{B}^c &= 0 \\ \nabla \cdot \boldsymbol{E}^c &= 0 \\ \nabla \times \boldsymbol{E}^c + \frac{1}{c}\frac{\partial \boldsymbol{B}^c}{\partial t} &= 0 \\ \nabla \times \boldsymbol{B}^c - \frac{1}{c}\frac{\partial \boldsymbol{E}^c}{\partial t} &= 0. \end{aligned} \tag{4.10}$$

We assume that cylindrical symmetry is preserved during the complete interaction of electron beam with the conductor foil. This implies that $E_\theta^c = B_r^c = B_x^c = 0$. By virtue of method of images, the fields of the conductor are,

$$\begin{aligned} E_r^c(r,x,t) = -E_r^b &= \frac{-2eN}{\sqrt{2\pi}\sigma_\parallel}\frac{1}{r}\left(1 - \exp(\frac{-r^2}{2\sigma_\perp^2})\right)\exp\left(\frac{-(x+x_0+vt)^2}{2\sigma_\parallel^2}\right) \\ B_\theta^c = B_\theta^b &= \frac{v}{c}E_r^c(r,x,t) \end{aligned} \tag{4.11}$$

The radial component of Maxwell-Ampere's equation for the conductor is identically satisfied.

$$\nabla \times \boldsymbol{B}^c = \frac{1}{c}\frac{\partial \boldsymbol{E}^c}{\partial t} \tag{4.12}$$

$$\begin{aligned} \frac{1}{c}\frac{\partial E_r^c}{\partial t} &= -\frac{\partial B_\theta^c}{\partial x} \\ \frac{v}{c}\frac{\partial E_r^c}{\partial x} &= -\frac{\partial(\frac{-v}{c}E_r^c)}{\partial x} \end{aligned} \tag{4.13}$$

And the vertical component,

$$\begin{aligned} \frac{1}{c}\frac{\partial E_x^c}{\partial t} &= \frac{1}{r}\frac{\partial(rB_\theta^c)}{\partial r} \\ &= \frac{1}{r}\frac{\partial(r\frac{-v}{c}E_r^c)}{\partial r} \\ \implies \frac{\partial E_x^c}{\partial t} &= \frac{-v}{r}\frac{\partial(rE_r^c)}{\partial r}. \end{aligned} \tag{4.14}$$

While $\nabla \cdot \boldsymbol{E}^c = 0$ implies,

$$\frac{\partial E_x^c}{\partial x} = -\frac{1}{r}\frac{\partial(rE_r^c)}{\partial r} \tag{4.15}$$

Thus the longitudinal and temporal dependence of E_x^c is determined by the radial dependence of (rE_r^c).

$$\frac{\partial(rE_r^c)}{\partial r} = E_r^c + r\frac{\partial E_r^c}{\partial r} \tag{4.16}$$

which implies, $E_x^c \approx E_r^c$.

Based on the above, we can conclude that there is a presence of a strong longitudinal electric field associated with the surface charge distribution of the conductor. However, this strong longitudinal field does not play any role in electron beam focusing and photon emission.

With this, we have obtained the beam and the conducting foil fields that provide an approximate solution to the Maxwell equations.

The total transverse electromagnetic fields at the boundary can be written as a linear superposition of the beam and conductor fields.

$$\begin{aligned} E_r(r,x,t) &= E_r^b(r,x,t) + E_r^c(r,x,t) \\ B_\theta(r,x,t) &= B_\theta^b(r,x,t) + B_\theta^c(r,x,t) \end{aligned} \tag{4.17}$$

Within the reflected field model, at the foil surface the total electric field is continuous and $E_r = E_r^b + E_r^c \approx 0$, whereas the total magnetic field is discontinuous and $B_\theta = B_\theta^b + B_\theta^c \approx 2B_\theta^b$. Effectively with respect to E_r and B_θ, the electron beam is colliding with its own image. This results in a net non-zero transverse Lorentz force $\boldsymbol{f}_\perp = e(E_r - B_\theta)\hat{r} = e(2B_\theta^b)\hat{r}$, and due to this force, the beam undergoes self-focusing and emits synchrotron like photon emission. This is analogous to a laser pulse hitting the conductor and getting reflected at the target surface.

4.4 Estimation of the radiated energy

With the information about the fields at the boundary, we proceed to estimate the total radiated energy. The electron quantum parameter χ_e primarily controls the amount of emission per unit time.

$$\chi_e = \frac{\gamma}{B_{cr}}\sqrt{\left(\boldsymbol{E} + \frac{\boldsymbol{v}}{c}\times\boldsymbol{B}\right)^2 - \left(\boldsymbol{E}\cdot\frac{\boldsymbol{v}}{c}\right)^2} \tag{4.18}$$

For the total electromagnetic fields obtained in Equation 4.17,

$$\begin{aligned} \left(\boldsymbol{E} + \frac{\boldsymbol{v}}{c}\times\boldsymbol{B}\right)^2 - \left(\boldsymbol{E}\cdot\frac{\boldsymbol{v}}{c}\right)^2 &= \left(E_r - \frac{v}{c}B_\theta\right)^2 + E_x^2 - E_x^2\frac{v^2}{c^2} \\ &= \left(E_r - \frac{v}{c}B_\theta\right)^2 + \frac{E_x^2}{\gamma^2} \end{aligned} \tag{4.19}$$

Since the electron beam is ultra-relativistic, $\gamma \gg 1$,

$$\chi_e \approx \frac{\gamma|E_r - B_\theta|}{B_{cr}} \quad \text{where} \begin{cases} E_r = E_r^b + E_r^c \\ B_\theta = B_\theta^b + B_\theta^c \end{cases} \tag{4.20}$$

The average energy radiated per particle per unit time as given in Katkov, Strakhovenko, et al., 1998 :

$$\begin{aligned} \dot{\varepsilon}_\gamma = \frac{\mathrm{d}\varepsilon_\gamma}{\mathrm{d}t} &= \frac{e^2 m_e^2 c^3}{3\sqrt{3}\pi\hbar^2} \int_0^\infty \frac{u(4u^2+5u+4)}{(1+u)^4} K_{2/3}\left(\frac{2u}{3\chi}\right) du \\ &= \frac{1}{3\sqrt{3}\pi} \frac{e^2}{\hbar c} \frac{m_e c^2}{\hbar} mc^2 \int_0^\infty \frac{u(4u^2+5u+4)}{(1+u)^4} K_{2/3}\left(\frac{2u}{3\chi}\right) du \\ &\approx \frac{2}{3}\frac{\alpha}{\tau_c} m_e c^2 \left[\frac{\chi^2}{(1+4.8(1+\chi\log_e(1+1.7\chi)+2.44\chi^2)^{2/3}}\right] \end{aligned} \tag{4.21}$$

If $f(r, x, \boldsymbol{p}, t) = \rho(r, x, t)\delta^3(\boldsymbol{p} - \boldsymbol{p_0})/e$ is the electron particle distribution function, then total initial energy of the beam is given by,

$$2\pi \int f(r, x, \boldsymbol{p}, t)\varepsilon_e(\boldsymbol{p})\mathrm{d}x r\mathrm{d}r\mathrm{d}^3p = \varepsilon_e(|\boldsymbol{p_0}|)N_e = \gamma m_e c^2 N_e \tag{4.22}$$

And the total average of the emitted energy by the electron beam is given by,

$$2\pi \int f(r, x, \boldsymbol{p}, t)\dot{\varepsilon}_\gamma \mathrm{d}x r\mathrm{d}r\mathrm{d}^3p\mathrm{d}t \tag{4.23}$$

where we have assumed that all the beam electrons have the same initial energy and momentum.

If we neglect energy loses during the interaction via other processes such as collisions, the fraction of emitted energy is,

$$\frac{2\pi \int f(r, x, \boldsymbol{p}, t)\dot{\varepsilon}_\gamma \mathrm{d}x r\mathrm{d}r\mathrm{d}^3p\mathrm{d}t}{\gamma m_e c^2 N} = \frac{2\pi \int \rho(r, x, t)\dot{\varepsilon}_\gamma(\chi_e(|\boldsymbol{p_0}|), r, x, t)\mathrm{d}x r\mathrm{d}r\mathrm{d}t}{\gamma m_e c^2 N} \tag{4.24}$$

The electron to photon conversion efficiency is

$$\eta = \frac{2\pi \int_{-\infty}^{+\infty} \mathrm{d}t \int_{-\infty}^{0} \mathrm{d}x \int_0^\infty r\mathrm{d}r \quad \rho(r, x, t)\dot{\varepsilon}_\gamma(\chi_e(|\boldsymbol{p_0}|), r, x, t)}{\gamma m_e c^2 e N} \tag{4.25}$$

We perform the integration in the above equation numerically.

In a nutshell for the analytical modelling, we consider a cold ultra-relativistic electron beam with cylindrical symmetry around its propagation axis. The foil is considered to be thin and infinitely conducting. We assume that cylindrical symmetry is preserved throughout the beam-foil interaction. The total electromagnetic fields were written as a linear superposition of beam and conductor fields. We use the method of images where applicable to determine the conductor fields. The key physical arguments considered in the analytical models are the continuity of total tangential electric field at the boundary

and zero within the conductor, and electromagnetic energy cannot be transferred across a surface of infinite conductivity. With this model we now aim to find the scaling laws that govern the dependence of the conversion efficiency η with respect to beam parameters such as (a) beam radius ($\sigma_\perp$) , (b) beam length $\sigma_\parallel$ and (c) beam mean energy γ.

4.5 2D simulation results

Having elaborately discussed the analytical models, we now present the results of the interaction of ultra-relativistic beam with thin aluminium (conductor) foil. For all our simulations, we use the particle-in-cell code SMILEI developed by Derouillat et al., 2018.

4.5.1 Simulation setup

The chosen electron beam parameters are within the reach of existing accelerator facilities such as FACET II (Yakimenko, Alsberg, et al., 2019). The beam has 2 nC charge, a Gaussian spatial and momentum distribution with 10 MeV mean energy, 212 MeV full width at half-maximum (FWHM) energy spread, and 3 mm-mrad normalised emittance. The target consists of 0.5 μm thick aluminium foil with initial charge state set to +3. We estimate the target thickness by considering an analogy with the reflectivity condition in light-sail acceleration (Macchi et al., 2010). The interaction of the laser and target is similar to the electron beam-target interaction with $\lambda_{laser} \approx 2(2\sqrt{2\ln 2}\sigma_\parallel)$. Within the light-sail acceleration model, the thin target plasma foil is modelled as a "mirror" foil that acts as perfectly reflecting surface during the interaction of the laser beam with the foil. The optimal target thickness l is chosen according to the reflectivity condition $l = a_0 n_c \lambda_{laser}/(\pi n_t)$, where $a_0 = (eE_r/(m_e c^2))\lambda_{laser}/(2\pi)$, $n_c = m_e(2\pi c/\lambda_{laser})^2/(4\pi e^2)$ and n_t corresponds to the plasma electron density of the conductor foil. Recall that E_r corresponds to the radial electric field of the electron beam. In light-sail acceleration, the laser fields are reflected by the thin target, while in our simulations, the electron beam self-fields are reflected from the target surface.

Our simulation domain depends on the size of the beam and is chosen as given in Figure 4.4. We ensure that boundary effects do not affect the simulation results. We use 16 particles-per-cell (ppc) for target ions, 196 ppc for target plasma electrons, and for the beam electrons we vary the ppc according to the beam size and the total beam macro-particles was kept approximately constant ($\sim 2.4 \times 10^7$) across all simulations. The spatial resolution of our simulation grid is given by $2\Delta x = \Delta y = 0.025$ μm. The electron beam enters the simulation box from the left and propagates in the x direction. We take into account the effect of field ionisation and collisional processes such as collisional ionisation, binary Coulomb collisions, bremsstrahlung emission and Bethe-Heitler pair production. We also consider field emission and pair production (stochastic

high-energy synchrotron photon emission and multiphoton Breit Wheeler) in all our simulations.

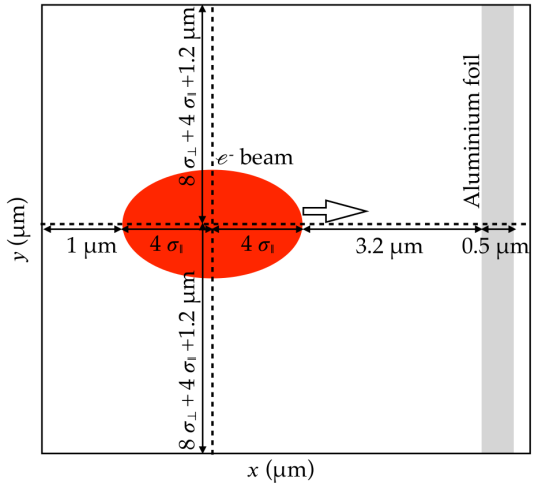

FIGURE 4.4: Schematic of the computational domain used in our 2D simulations

With the described simulation setup we conduct a series of simulations to explore the dependency of radiated energy on the (a) transverse size of the beam, (b) the shape of the beam, and (c) the energy of the beam. In sec 4.5.4, we extend our studies to investigate the collision of a round electron beam with multiple aluminium foils which are separated by 10 µm. Our 2D simulations shed light both on the radiated energy and the electron beam focusing.

4.5.2 Beam dynamics in the vicinity of a single foil

In this subsection, we briefly present the key phenomena underpinning the interaction of an ultra-relativistic electron beam with a sub-micrometer thin conductor foil. Our goal is to present the root mechanism that occurs in all our simulations. In Figure 4.5 we show different stages of electron beam interaction with the foil: (i) beam in vacuum (column 1 in Figure 4.5), (ii) beam centre hits the target front (column 2 in Figure 4.5), and (iii) beam exits the target (column 3 in Figure 4.5). In the vacuum, the beam electric and magnetic fields compensate each other perfectly as expected. In the second stage, when the beam centre reaches the the target front, the electromagnetic self-fields of the beam are shielded by the conducting foil surface, consequently the transverse magnetic field is doubled ((b2) in Figure 4.5) and the transverse electric field goes to zero ((c2) in Figure 4.5) just in front of the target surface. The beam rear experiences the transverse force induced due to this field imbalance and experiences slight self-transverse focusing and emits a lot of photons. As the beam exits the conductor fully ((a3) in Figure 4.5), the beam starts to regenerate it's own self-fields. In 2D simulations, the self-fields extend infinitely transversely due to the infinite z length. The beam loses energy considerably to this extensive field recreation artefact. It is important to also

note that the beam emits photons as it exits the conductor. This can be explained as the radial electric field is zero also at the rear foil surface, and the magnetic field grows gradually during the beam exit. However all our simulations indicate that stronger fields at present at the beam entrance and photon emission is dominated by beam emission at the foil entrance.

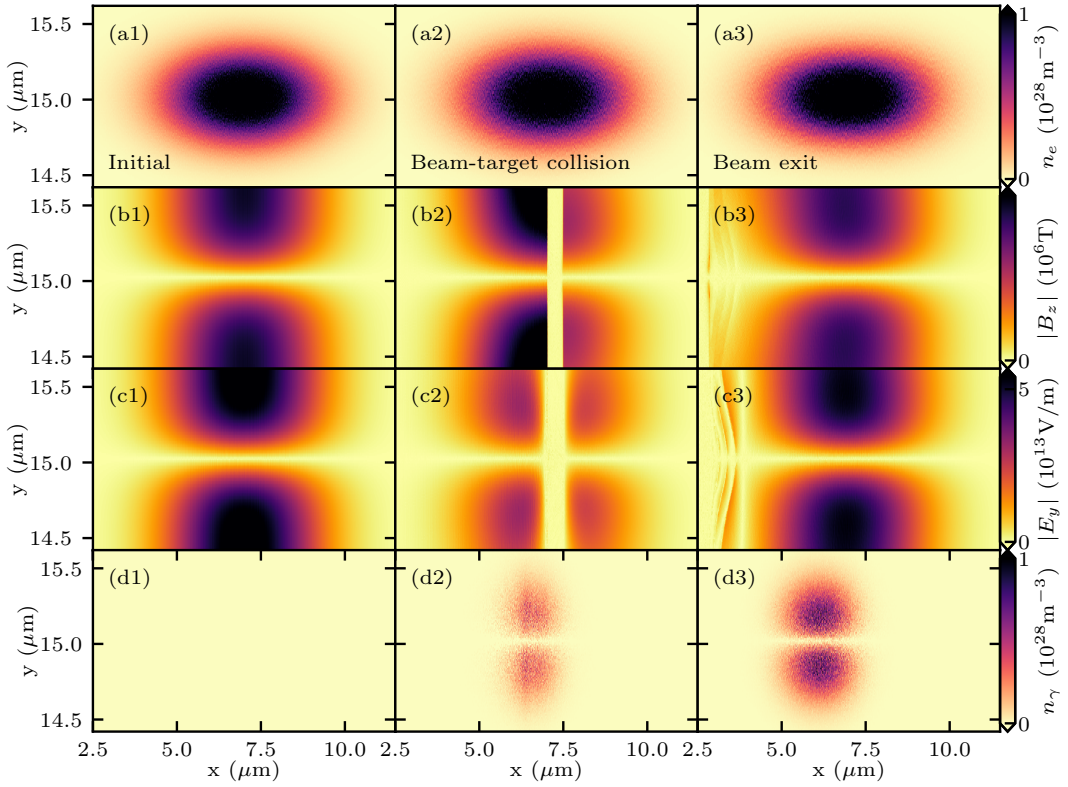

FIGURE 4.5: Snapshots of beam with $\sigma_{\parallel} = 1.5$ μm and $\sigma_{\perp} = 0.2$ μm evolution during the interaction with a single aluminium foil.

4.5.3 Variation of the radiated energy with the beam parameters

To investigate the effect of beam parameters on the amount of radiated energy, we consider a reference beam with $\sigma_{\parallel} = 1.5$ μm and $\sigma_{\perp} = 0.2$ μm. The chosen parameters are very close to the expected beam parameters at FACET II. We then vary (a) $\sigma_{\perp}$, (b) beam shape by keeping the self-fields constant and (c) mean energy of beam γ and study the variation in the obtained total radiated photon energy. It is important to note that in 2D geometry, the beam and the foil are considered to be infinite in the z direction, and therefore all values are independent of z. Both the beam density and the fields depend on time t and coordinates x and y.

Effect of the transverse size of the beam

For our investigations reported in Table 4.1, we keep the bunch length $\sigma_{\parallel}$, mean energy γ and total number of beam particles N_e to be constant, and increase $\sigma_{\perp}$ by $\Delta\sigma_{\perp} =$

0.1 and 0.2 μm. This implies that the beam density and the fields depend only on the transverse coordinate y which controls r. In particular, the total transverse fields in general are proportional to the inverse of radial distance (Equation 4.8). Hence qualitatively we can expect the transverse force ($\boldsymbol{f}_\perp \approx (E_r - v_x/cB_\theta)$) to decrease as the beam radius $\sigma_\perp$ increases. The quantum parameter $\chi_e \propto \boldsymbol{f}_\perp$ governs photon emission and changes significantly with beam radius as shown in Figure 4.6.

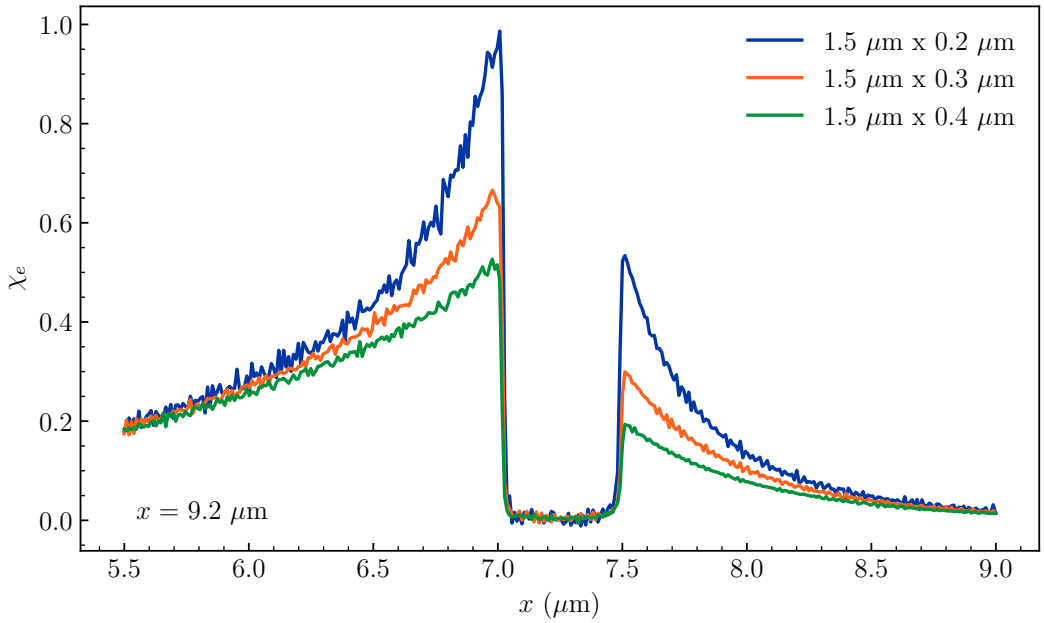

FIGURE 4.6: The quantum parameter χ_e obtained from 2D PIC simulations as a function of the longitudinal distance for three different beam radius. The beam centre has propagated a distance of $x = 9.2$ μm before hitting the target front surface.

The obtained electron to photon conversion efficiency is reported in Table 4.1. From the figure and the table we see that with increase in beam radius, the fields and subsequently the radiated energy decreases. Therefore, for a fixed short beam length, compression of beam transversely increases the final radiated energy.

$\sigma_\parallel$ (μm)	$\sigma_\perp$ (μm)	Conversion efficiency (η %)
1.5	0.2	$\eta_1 = 2.6$
1.5	0.3	$\eta_2 = 1.8$
1.5	0.4	$\eta_3 = 1.4$

TABLE 4.1: Variation of electron to photon conversion efficiency η obtained from 2D PIC simulations with respect to the transverse size of the beam.

Effect of beam shape

We now discuss the effect of shape of the beam on the radiated energy. The shape of an electron beam depends on both the beam length and the beam radius. A round electron beam has a length equal to it's radius, while, an oval electron beam has a radius greater than it's length, and a disc like electron beam has a length greater than it's radius. We vary the beam shape by changing the beam length and the beam radius such that the product of $\sigma_{\parallel} \times \sigma_{\perp}$ is a constant value. This in turn ensures that the maximum amplitude of transverse fields that controls χ_e and thereby photon emission is also a constant. Recall that the transverse electric field is $\propto 1/(r\sigma_{\parallel})$. The emission of photons depends primarily on the number of electrons in an intense field region. Firstly, although we keep the maximum amplitude of the initial self-field constant in our simulations, the value of $\sigma_{\perp}$ determines the location of the maximum field. Secondly, it is important to have a large number of electrons experience this "maximum" field region. In other words, we need a substantial amount of electrons in the intense field region. An optimal combination of $\sigma_{\parallel} \times \sigma_{\perp}$ for a constant perpendicular field ensures the most efficient conversion of electron energy into photons. The values for conversion efficiency as we vary the beam shape is reported in Table 4.2.

$\sigma_{\parallel}$ (μm)	$\sigma_{\perp}$ (μm)	Conversion efficiency (η %)
1.5	0.2	2.6
1.0	0.3	2.9
0.75	0.4	3.0
0.55	0.55	2.7
0.4	0.75	2.2
0.3	1.0	2.2

TABLE 4.2: Variation of electron to photon conversion efficiency η obtained from 2D PIC simulations with respect to the shape of the beam.

Effect of varying beam energy

Now we discuss the effect of mean beam energy on photon emission for the beam with $\sigma_{\parallel} = 1.5$ μm and $\sigma_{\perp} = 0.2$ μm. From Table 4.3, we can conclude that although the total radiated energy increases with increasing γ of beam, it is not drastically dependent on γ.

Mean beam energy	Conversion efficiency (η %)
10 GeV	2.6
20 GeV	3.4
30 GeV	3.8

TABLE 4.3: Variation of electron to photon conversion efficiency η obtained from 2D PIC simulations with respect to mean energy of the beam.

In conclusion, from the 2D beam parameter scans, we show that the beam shape (the product $\sigma_{\parallel} \times \sigma_{\perp}$) plays a key role in the amount of particles that are present in a strong-field region, and since these focusing effects only act on the transverse profile of the beam, it is pragmatic to start with a beam that has short length. In addition, given the sub-micron foil thickness in the reported simulations. We confirm that the effect of collisional processes is (binary Coulomb collisions, collisional ionisation, bremsstrahlung emission and Bethe-Heitler pair production) negligible.

4.5.4 Multiple foil interaction

Having discussed the electron beam-foil interaction dynamics for a single foil, we now extend the idea to multiple foils. In particular, we study the interaction of a round electron beam (0.55 μm × 0.55 μm) with a periodic array of 20 Al^{+3} foils. The foil thickness is 0.5 μm and distance between the rear and front of two consecutive foils is set as 10 μm. This distance is chosen to allow the electron beam to recreate it's own self-fields to it's vacuum value before colliding with the subsequent foil. The inter-foil distance is not large enough to lead to a significant beam expansion.

From the 2D simulations, we observe a total of conversion of ∼19% of initial electron beam energy into energy of photons. The conversion efficiency η as a function of the number of foils crossed by the beam is reported in Figure 4.8. Specifically the electron beam energy in 2D simulations is burnt out both by photon emission and self-field reproduction after interaction with each foil. The self-fields extend infinitely in the transverse direction in 2D simulations which is a numerical artefact.

To further grasp the complex electron dynamics during this multiple-foil interaction we show in Figure 4.7, some snapshots of beam evolution. The first column in the Figure 4.7 corresponds to the initial time. The electron beam displays a gaussian density profile (Figure 4.7(a1)), and as expected the transverse fields (Figure 4.7(b1)) is zero as the focusing magnetic field and the defocusing electric fields cancel almost perfectly for an ultra-relativistic beam. The second column of Figure 4.7 shows the instant when the beam centre collides with the fourth foil. By now, the rear of the beam, which experiences the most focusing force accompanied by photon emission is significantly compressed (Figure 4.7(a2)). We can also see that there is a net strong focusing transverse force (Figure 4.7(b2)), and the generated photons are displayed in Figure 4.7(c2). With further collisions, the density of the rear drops as one part of the beam crosses and overshoots the other transversely (Figure 4.7(a3)). And finally, the beam dynamics becomes complex as the beam experiences longitudinal modulations. This is due to the presence of a longitudinally inhomogeneous transverse force as seen in Figure 4.7(b4).

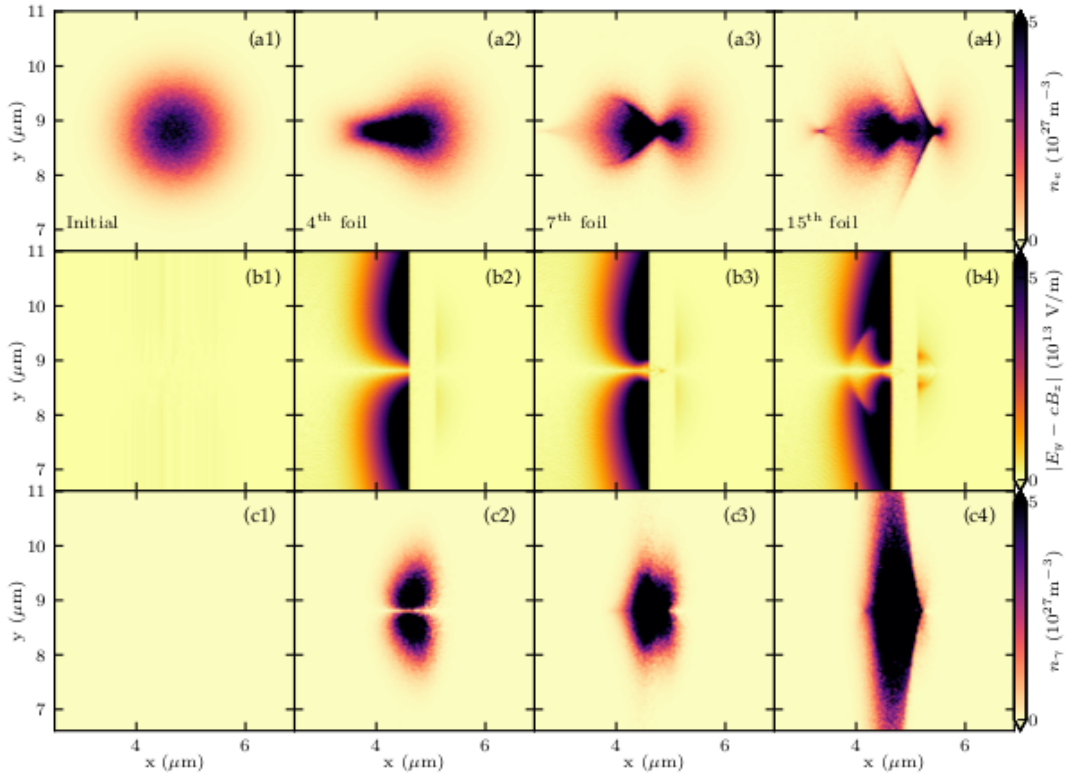

FIGURE 4.7: Electron beam evolution. First column, initial electron beam density (a1), the transverse field (b1), and the initial photon density (c1). Second to fourth column, same quantities as in the first column but at the 4th (a2)-(c2), the 7th (a3)-(c3), and the 15th (a4)-(d4), beam-foil interaction, respectively.

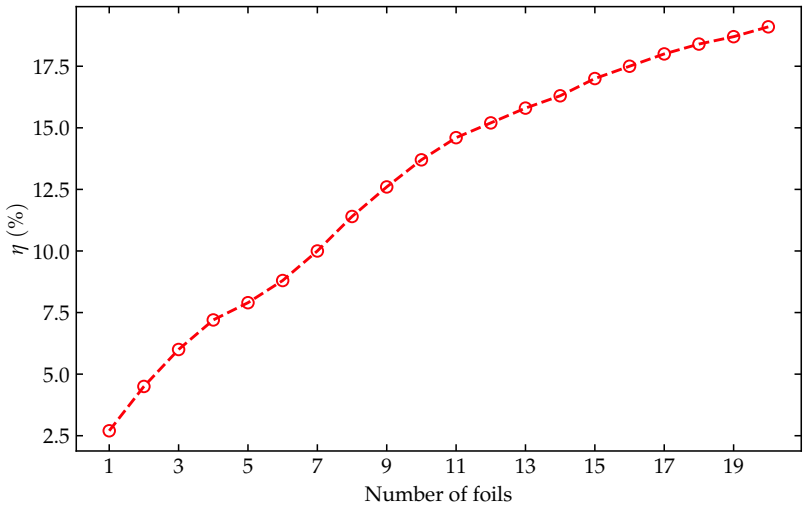

FIGURE 4.8: The electron to photon conversion efficiency η obtained from 2D PIC simulations as a function of number of foils crossed by the electron beam.

4.6 3D simulation results

The extension of self-fields infinitely in the transverse direction in 2D simulations interferes with the physics being studied, and therefore it is crucial to use fully 3D PIC simulations to enable the accurate modelling of ultra-relativistic electron beam interaction with sub-micron thick conductor foils. In this section, we investigate the scalings of electron energy conversion into photons with respect to beam emittance, bunch length $\sigma_{\parallel}$ and bunch radius $\sigma_{\perp}$ and finally electron beam interaction with multiple foils.

4.6.1 Simulation setup

As in 2D simulations, we initialise the electron beam with gaussian spatial and momentum distribution $\sigma_{\parallel}$, $\sigma_{\perp}$ being the RMS beam length and radius, 10 GeV mean energy, 212 MeV FWHM energy spread and 3 mm-mrad emittance. The aluminium target is initially in Al^{+3} charge state with 0.5 μm thickness. The simulation domain is chosen such that boundary effects do not affect the region of interest; i.e., the full beam region. Unless otherwise specified, the resolution $dx = 0.5dy = 0.5dz = 0.0125$μm. The temporal resolution $dt \sim 1.96 \times 10^{-17}s$. In the simulations, we also take into account the effect of binary Coulomb collisions between charged particle species, collisional and field ionisation, synchrotron radiation and multiphoton-Breit-Wheeler pair production. Bremsstrahlung emission and Bethe-Heitler pair production are considered as necessary.

4.6.2 Beam-Single Foil Interaction

We first illustrate the beam self-focusing and photon emission mechanism during the collision of the beam with a single aluminium foil. The model beam is chosen such that the reflected field model (obtained via method of images) fully holds, i.e., $\sigma_{\perp} \gg \sigma_{\parallel}$. We consider an electron beam with $\sigma_{\parallel} = 0.55$ μm and $\sigma_{\perp} = 1.25$ μm. Figure 4.9(a) displays a snapshot of the electron beam density when the beam centre has reached the front surface of the foil. Figures 4.9(b) and 4.9(c) show the transverse magnetic $\boldsymbol{B}_{\perp}$ and electric field $\boldsymbol{E}_{\perp}$, respectively. As seen in 2D simulation results, and expected from the analytical model, at the boundary surface of collision, $\boldsymbol{B}_{\perp}$ is amplified and its peak value doubles with respect to the beam self-field (3.1×10^4 T), $\boldsymbol{E}_{\perp}$ is suppressed and is much smaller than the beam self-field (9.4×10^{12} V/m). Thus, when an electron beam collides with a conductor, the focusing magnetic term of the Lorentz force overcomes the de-focusing electric term, leading to a net result of beam self-focusing.

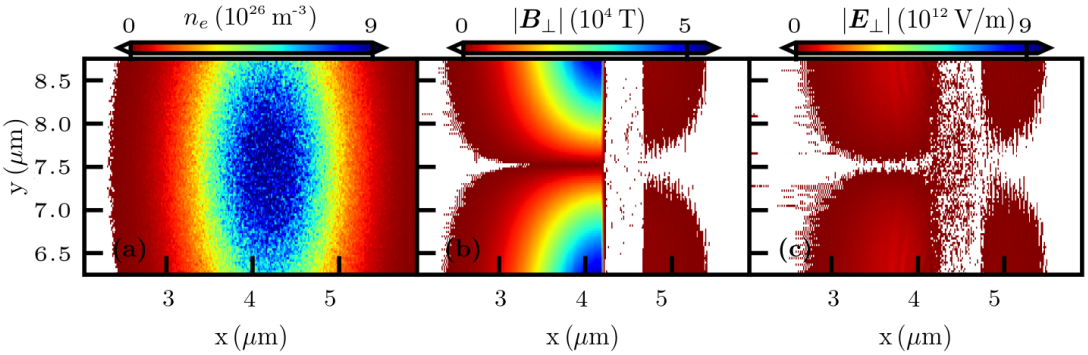

FIGURE 4.9: (a) Electron beam density, (b) transverse magnetic field, and (c) transverse electric field in the collision of an electron beam with 0.5 μm thick aluminium foil. The electron beam has 2 nC charge, 10 GeV energy, $\sigma_\parallel$ = 0.55 μm and, $\sigma_\perp$ = 1.25 μm

4.6.3 3D scalings with respect to beam parameters

In this subsection, we study the effect of beam elongation and focusing individually in both directions and compare with the predictions of analytical models.

Transverse modulation

We transversely modulate a beam with $\sigma_\parallel$ = 0.55 μm and compare the conversion efficiency with and without beam emittance. In addition as photon emission occurs when the beam crosses any boundary, i.e., when the beam enters or exits the target, we record the contribution from both entrance and exit phase separately.
In Table 4.4, we report the conversion efficiency η obtained from the simulations for a beam with and without emittance as we increase $\sigma_\perp$ from $0.275 - 1.25$ μm. It is clearly evident that the obtained radiated energy is robust with respect to beam emittance. We also report in Table 4.4 η obtained solely from the beam entrance phase. We obtain this by using a 2 μm target which ensures that there is no overlap of entrance and exit emission signals. It can be concluded that the dominant contribution to emission comes from the beam entrance phase. Specifically, when $\sigma_\perp \geq 0.55$ μm (i.e., $\sigma_\perp \gg \sigma_\parallel$), more than 75% of the total emission recorded in the simulations is from the beam entrance phase.

$\sigma_\perp$	Conversion efficiency η (%)		
(μm)	Cold beam	Beam emittance$\neq$ 0	Beam entrance
0.275	1.94 %	1.94 %	1.23%
0.55	1.14 %	1.14 %	0.86 %
0.75	0.81 %	0.81 %	0.66 %
1.00	0.56 %	0.56 %	0.48 %
1.25	0.44 %	0.44 %	0.37 %

TABLE 4.4: Variation of conversion efficiency of η with respect to $\sigma_\perp$ with and without beam emittance. The conversion efficiency obtained during beam entrance phase is also reported.

In Figure 4.10, we present η as a function of $\sigma_\perp$ for the reflected (blue circles) field model, and the corresponding PIC simulation results (black circles). As discussed in Section 4.3, when $\sigma_\perp \ll \sigma_\parallel$ (for example, $\sigma_\perp = 0.275\,\mu$m and $\sigma_\parallel = 0.55\,\mu$m), the current neutralisation effects propagate from the beam centre to $r \approx \sigma_\perp$ reducing the value of total reflected fields from the conductor boundary. The results obtained for $\sigma_\perp = 0.275\,\mu$m show more difference with respect to the analytical expectation in comparison to $\sigma_\perp = 1.25\,\mu$m. This corresponds to the magnetostatic approximation, which implies a vanishing B^c_θ, and the result focusing field is majorly from the uncompensated electron beam self-fields.

The obtained simulation results agree more with the reflected field approximation with increasing $\sigma_\perp$. To further validate the effect of current neutralisation, we report in Table 4.5, the ratio of transverse peak magnetic field observed when the beam centre hits the target front to the initial beam transverse magnetic field $\frac{B_{center,peak}}{B(t=0)}$ for different values of $\sigma_\perp$. It is clear from the table that the peak amplitude of total transverse fields increases with increasing $\sigma_\perp$, thereby supporting the validity of the reflecting field model.

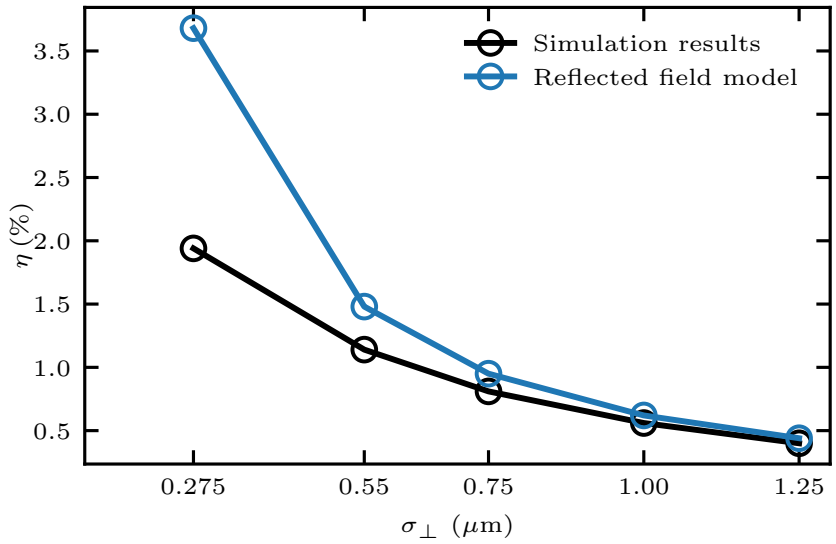

FIGURE 4.10: Conversion efficiency η in electron beam-foil collision as a function of $\sigma_\perp$. Results from 3D PIC simulations (black circles), reflected field (blue circles) model predictions.

$\sigma_\perp$ (μm)	$\frac{B_{center,peak}}{B(t=0)}$ Simulations (S)	Reflected field model (RF)	Relative error $\frac{RF-S}{RF} \times 100$
0.275	1.3	2	35%
0.55	1.6	2	20%
0.75	1.8	2	10%
1.00	1.8	2	10%
1.25	1.9	2	5%

TABLE 4.5: The ratio of peak transverse magnetic field observed when beam centre hits the target front to the initial beam transverse magnetic field $\frac{B_{center,peak}}{B(t=0)}$ as function of $\sigma_\perp$.

Longitudinal modulation

We move on to discuss the effect of longitudinal modulation of the electron beam for a constant $\sigma_\perp = 0.55$ μm. We use a cold beam in our simulations as it was already shown that beam emittance does not affect the physics being discussed in our work.

In Figure 4.11, we show η as a function of $\sigma_\parallel$ for the reflected (blue circles) field model, and the corresponding PIC simulation results (black circles). As explained for transverse elongation, the ratio of $\sigma_\perp/\sigma_\parallel$ is crucial in determining the effects of current neutralisation. The results for longitudinally compressed beam fit well with reflected field approximation, and the difference between analytical predictions and simulation results increase for longitudinally elongated beams. We report the ratio of the peak

$\sigma_{\parallel}$ (μm)	$\frac{B_{center,peak}}{B(t=0)}$ Simulations (S)	Analytical (A)	Relative error $\frac{A-S}{A} \times 100$
0.275	1.7	2	15%
0.55	1.6	2	20%
0.75	1.5	2	25%
1.00	1.3	2	35%
1.25	1.2	2	40%

TABLE 4.6: Effect of $\sigma_{\parallel}$ on the amount of reflection of fields by the target.

transverse magnetic field observed when beam centre hits the target front to the initial beam transverse magnetic field $\frac{B_{center,peak}}{B(t=0)}$ for different values of $\sigma_{\parallel}$ in Table 4.6, It is clear from the table that the peak amplitude of total transverse fields ($B^c_\theta + B^b_\theta$) decreases with increasing $\sigma_{\parallel}$ (i.e., $\sigma_{\perp} \ll \sigma_{\parallel}$), thereby elucidating the decrease in conductor fields B^c_θ, which corresponds to the magnetostatic approximation.

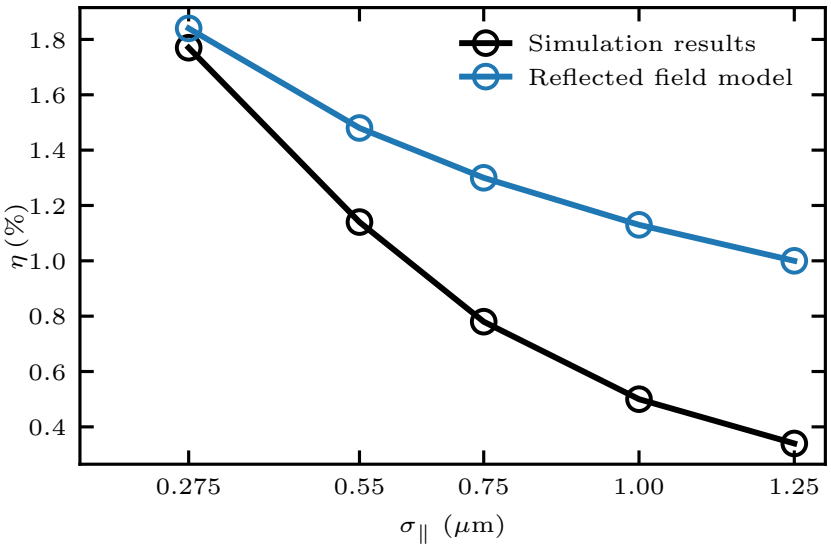

FIGURE 4.11: Conversion efficiency η in electron beam-foil collision as a function of $\sigma_{\parallel}$. Results from 3D PIC simulations (black circles), and reflected field (blue circles) field model predictions.

4.6.4 Beam-Multiple foil interaction

We now move onto the interesting and novel idea of the interaction of an ultra-relativistic electron beam with multiple-foils. The goal is to use full 3D PIC simulations will enable to capture the rich dynamics of the electron and gamma beam evolution without any numerical artefacts. A schematic of our setup is given in Figure 4.12. The beam and target parameters are chosen to be exactly the same as in 2D simulations (Refer subsection 4.5.4). Note that, in both 2D and 3D simulations, the distance between two foils

(inter-foil distance) is kept to be 10 μm. For efficient self-focusing, this distance must be sufficiently large to allow for the restoration of beam-fields around its propagation axis ($r \sim \sigma_\perp$), which requires the inter-foil distance to be greater than $\sigma_\perp$. Additionally, it needs be short enough to prevent beam expansion. This can be estimated by considering the effect of $|\boldsymbol{f}_\perp| \approx |2eB_\theta|$ calculated at $x \approx x0 + vt$ and $r \sim \sigma_\perp$, i.e., where the focusing is stronger. For $\sigma_\perp \gg \sigma_\parallel$, the coherent transition radiation extends approximately over a distance $\sigma_\perp^2/\sigma_\parallel$, which is larger than the beam length $\sigma_\parallel$. Thus, $|\boldsymbol{f}_\perp|$ lasts for approximately $\sigma_\parallel/c$, and the deflection angle is $\theta \approx |\boldsymbol{f}_\perp|\sigma_\parallel/\gamma m_e c^2$. Hence, to prevent defocusing the inter-foil distance must be much smaller than $\sigma_\perp/\theta$.

In total we observe a conversion of $\sim 30\%$ of the initial electron energy into dense collimated photon beam production.

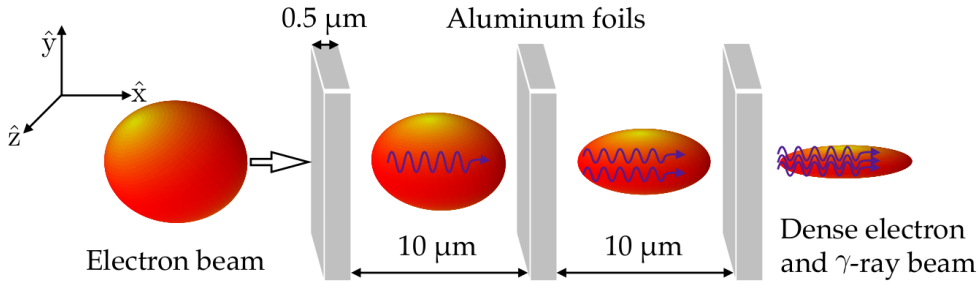

FIGURE 4.12: Schematic setup of beam interaction with multiple aluminium foils.

Finite beam emittance

We first study the interaction of the electron beam with multiple foils when the beam emittance is equal to 3 mm-mrad. Figure 4.13 snapshots of the electron and gamma beam evolution. During the collision of the beam from the first to sixth foil, the beam interacts with the field "reflected" by each foil. As explained previously, this leads to the self-focusing of the beam accompanied by synchrotron-like photon emission. This self-focusing of the beam, gradually increases the beam density from its initial value of 4.7 $\times$ 10^{27} m^{-3} to 8.2 $\times$ 10^{28} m^{-3} after the 6th foil (see first to third column of Figure 4.13). The corresponding maximum photon number density and the peak value of χ_e of the electrons are 2.9 $\times$ 10^{28} m^{-3} and 0.8 respectively. A transition occurs in the interaction with the 7th foil, where the electron beam density reaches 3.8 $\times$ 10^{29} m^{-3} exceeding the foil density 1.8 $\times$ 10^{29} m^{-3}. (see Figure 4.13(a3)-(d3)). Thus, the foil is unable to reflect the fields of the beam, and a channel is created inside the foil. Within this channel (localised at the beam location), the plasma electrons are expelled. The field strengths observed in this channel were strong enough to cause rapid field ionisation and also trigger strong-field QED effects. Here χ_e and the photon beam density rise up to 3 and 4.1 $\times$ 10^{29} m^{-3}, respectively. Moreover, approximately 10^{-4} photons convert into electron-positron pairs via multi-photon Breit-Wheeler pair production. At this stage, when the electron beam density is greater than the plasma electron density, the beam does not interact with reflected fields at the target boundary,

and subsequently the focusing effects stop. Instead of focusing, the beam undergoes longitudinal modulation (see Figure 4.13(a5)-(a6)). The modulation arises because both reflected and channeling fields are stronger around the rear part of the beam, which yields in the longitudinal inhomogeneous focusing force. (see Figure 4.13(b4)-(c4)). The effect of the computational grid resolution when the beam density increases is reported in the upcoming subsection 4.6.4.

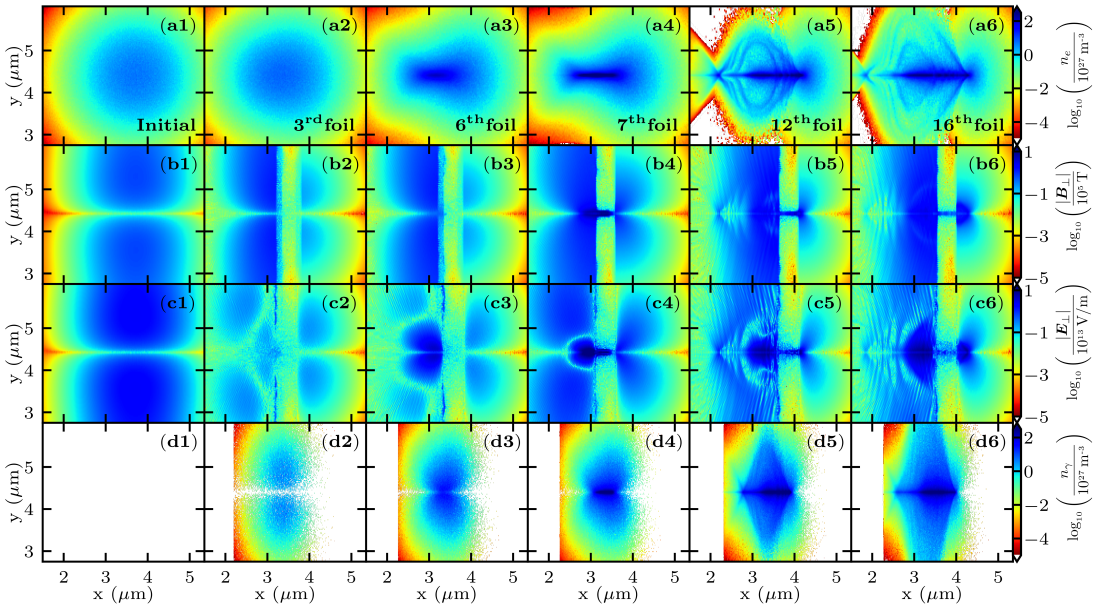

FIGURE 4.13: Beam evolution. First column, initial electron beam density (a1), its magnetic (b1) and electric (c1) field, and the initial photon density (d1). Second to sixth column, same quantities as in the first column but at the 3rd (a2)-(d2), the 6th (a3)-(d3), the 7th (a4)-(d4), the 12th (a5)-(d5), and the 16th (a6)-(d6) beam-foil interaction, respectively.

Figure 4.14(a) reports the initial (black dashed line) and final (blue line) electron beam energy distribution after the interaction with 20 consecutive foils. The final energy distribution shows a residual peak around the initial electron beam energy, which is indicative of the relatively small energy loss of the front part of the beam, both due to synchrotron emission and collisional processes. The broad distribution around 5 GeV results from the intense synchrotron emission occurring in the central and rear part of the beam. Figure 4.14(b) reports the final photon spectrum and the conversion efficiency η (inset) as a function of the number of crossed foils. The sudden increase of η at the 7th foil is explained by the transition from the field reflection to the field channeling regime. After colliding with 20 foils, more than 30% percent of the electron beam energy is converted into a collimated (5 mrad rms photon energy angular distribution), 4 femtosecond FWHM duration, 2.8 $\times$ 10^{29} m^{-3} density gamma-ray pulse.

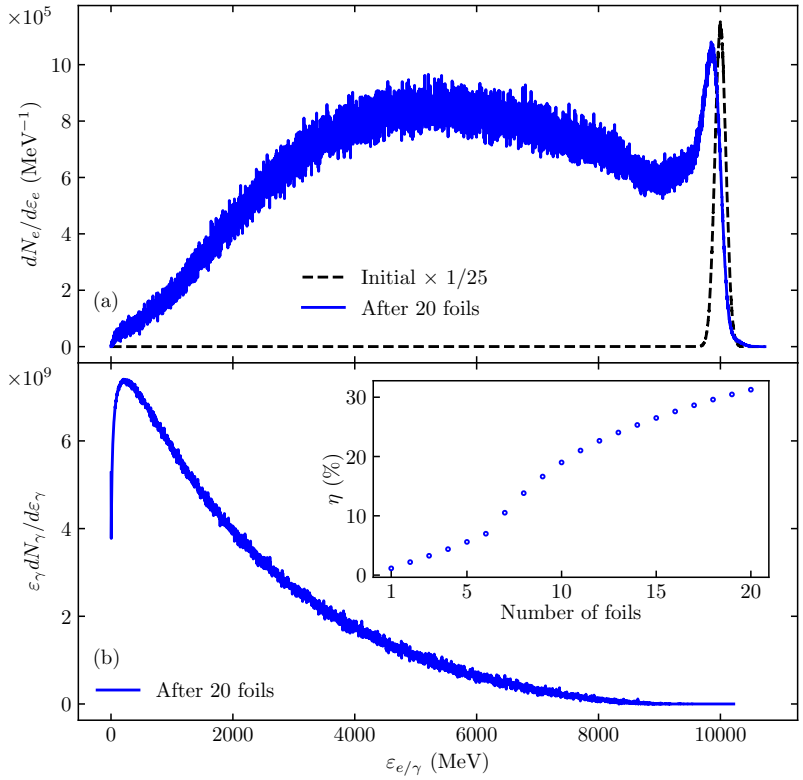

FIGURE 4.14: Panel (a), initial (black dashed line) and final (blue line) electron beam energy distribution. Panel (b), final pho- ton spectrum. The inset displays the conversion efficiency η as a function of the number of foils crossed by the electron beam.

Convergence of results

As reported previously, the beam density during interaction with the seventh foil increases up to 3.8 $\times$ 10^{29} m^{-3} exceeding the foil density 1.8 $\times$ 10^{29} m^{-3}. In our simulations, the grid was designed to resolve a maximum of foil plasma electron density, which is much greater than the initial beam electron density. Hence, in order to check the robustness of the results, we performed convergence tests. In order to do so, we extract the beam density profile data just after beam interaction with the 6th foil, approximately at 57.6 μm propagation distance. We then input this data into new simulation grid with increased resolution. The beam is allowed to interact with one foil with 0.5 μm thickness. Since these are fully 3D PIC simulations, the computational resources needed are very demanding. Due to the sub micro-meter foil thickness, and from the trends observed in all our simulations, we know that collisional processes and multiphoton Breit-Wheeler pair production is negligible. Hence, we do not incorporate these effects in our new simulation with increased resolution. In particular, since the beam is compressed transversely, we increase the transverse resolution of the computational grid. We check the effect of numerical grid resolution only for beam-single foil interaction as the beam expands after interacting with the seventh foil. We report the tests for convergence in Table 4.7. The obtained data in the first row corresponds to the

computational grid resolution used in our beam-multiple foil simulations. The relative error between the first row and the highest resolution we approach within the limits of our cluster facility is 29%. The results presented in the second row show a relative difference of approximately 7% with respect to the third row results (highest achievable resolution). Therefore, we state that we underestimate the conversion efficiency during the beam interaction with the seventh foil in our beam-multiple foil interactions.

Resolution of the computational PIC grid	Conversion efficiency η (%) (after interaction with foil number 7)
dx= 0.0125 μm, dy= dz= 2dx	3.54
dx= 0.0125 μm, dy= dz= 1dx	4.61
dx= 0.0125 μm, dy= dz= 0.5dx	4.96

TABLE 4.7: Convergence of results with respect to numerical grid resolution. The conversion efficiency obtained by taking the beam data after interaction with the sixth foil and inputting the data into a computational grid with higher resolution.

In addition, we performed simulations with varying numerical resolution during the interaction of a cold electron beam with $\sigma_{\parallel} = 0.55\,\mu$m and $\sigma_{\perp} = 0.027\,\mu$m. The transverse size of the beam is chosen such that the resultant peak beam density is comparable with the peak beam density observed during beam interaction with seventh foil. In these simulations, we reduce both the transverse and longitudinal grid size thereby increasing grid resolution along both directions. The results presented in the first row of the table correspond to the grid resolution we use in our beam-multiple foil collisions. The relative error between the first row and the third row (highest numerical grid resolution we achieved) is approximately 24%. The results presented in the second show a relative difference of approximately 7% with respect to the third row results (highest achievable resolution). The beam parameters although chosen here are extreme, we restate that we underestimate the conversion efficiency of energy transferred from the electron beam into photon emission during the beam interaction with the seventh foil.

Resolution of the computational PIC grid	Conversion efficiency η(%)
dx= 0.0125 μm, dy= dz= 2dx	18.91
dx= dy= dz= 0.0125 μm	23.20
dx= dy= dz= 0.00625 μm	24.83

TABLE 4.8: Variation of conversion efficiency η (%) as we increase the computational grid resolution.

Cold beam

In the previous section, the electron beam emittance was chosen to be 3 mm-mrad, a value expected at the FACET II beam facility. Here, we repeat the simulation in the previous section with a cold electron beam, and without collisions and collisional ionisation. We let a cold electron beam collide with 16 sub-micrometer thick aluminium foils.

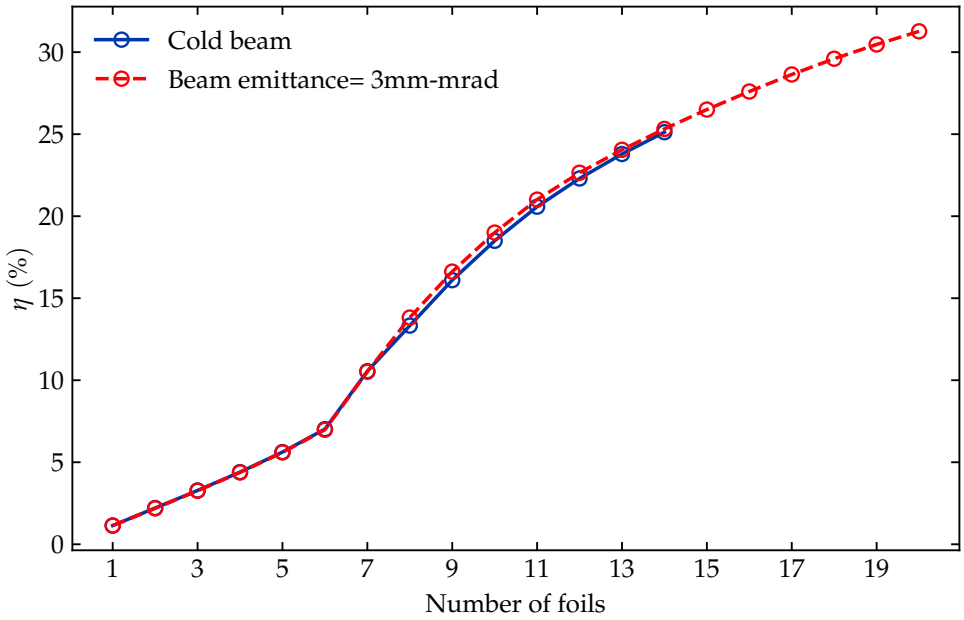

FIGURE 4.15: Scalings of conversion efficiency of electron beam energy into photon energy as a function of number of foils.

Figure 4.15 presents conversion efficiency of electron beam energy into photon energy as a function of number of foils. We plot the results obtained with a initially cold electron beam and when beam emittance was equal to 3 mm-mrad. The results match very closely, which implies that the mechanism of beam self-focusing and photon emission is robust with respect to beam emittance, binary Coulomb collisions and collisional ionisation. We also confirm that there are no numerical artefacts as we performed tests using different fields solvers and different boundary conditions.

4.7 Conclusions

Using self-consistent 2D and 3D PIC simulations, we have extensively studied the interaction of an ultra-relativistic electron beam with sub-micron thin aluminium foil. The key outcomes of this interaction are electron beam self-focusing and photon emission. We have then investigated the effect of transverse and longitudinal beam size on this mechanism and we have compared the simulation results with approximate analytical models. To summarise, the root mechanism of beam self-focusing and photon emission is robust for a wide range of $\sigma_{\parallel}$ and $\sigma_{\perp}$ parameters. We have extended the idea

to electron beam interaction with multiple foils. In this interaction, we have observed extreme electron beam self-focusing and the production of a dense collimated GeV photon beam. We have reported an efficient conversion $\sim 30\%$ of electron beam energy into the gamma photons. Specifically, the obtained electron and photon beams have a number density that exceeds that of a solid. From all our simulations, we have concluded that the obtained results are robust with respect to beam emittance. Another interesting feature is the observation of "channelling" regime when the electron beam density becomes greater than the target foil density. The electron beam self-fields channel into the target and enables the creation of strong-fields such that the χ_e parameter of the electron rises to ≈ 3 within the target. This implies that the field strengths in the rest frame of electron beam rises up to approximately 3 times the critical QED field. Collisional processes were not significant so far in all our simulations. This opens up the possibility of accessing the strong field QED regime with a single electron beam and without external super intense laser fields. Overall, our relatively simple setup is promising, and we have illustrated the generation of extremely dense collimated gamma-ray pulses with applications both in fundamental and applied physics.

Chapter 5

Summary and Outlook

5.1 Summary

We have first discussed the Maxwell-Vlasov equations that govern the self-consistent evolution of plasmas and the numerical method employed to solve these equations, namely, the Particle-In-Cell (PIC) technique. In order to determine the role of collision assisted radiation and pair production in electron beam-plasma interactions, we have implemented bremsstrahlung emission and Bethe-Heitler pair production in the ultra-relativistic regime within the PIC code SMILEI. The cross-section of both these processes varies with respect to the effect of nuclear field screening by the surrounding electrons. Therefore, we have implemented both these processes in the two extreme limits of screening, i.e., the non-screened and completely screened cross-sections. Furthermore, we have systematically validated the implemented cross-sections against theoretical predictions, and we have briefly reviewed the effect of screening. We have observed that screening effects gain importance when the electron energy is greater than 50 MeV for bremsstrahlung emission and when the photon energy is of the order of GeV in the presence of a target nucleus with high atomic number.

With this enriched PIC code, we have studied the interaction of a multi-GeV electron beam with aluminium foil(s). Based on the simulation results, we have shown that the electron beam undergoes strong self-focusing accompanied by efficient emission of gamma-ray photons. We have discussed the physical origin of beam self-focusing and high-energy photon emission, which arises from the beam interaction with the near-field transition radiation accompanying the beam-foil collision. We have also shown that the self-generated fields can be strong enough that emission occurs in the strong-field QED regime, where a single emitted photon can carry away a significant fraction of the emitting electron energy. Due to the submicrometre thickness of the target foil(s), the effect of collisional processes has been negligible in our simulations.

For a fixed electron beam charge of 2 nC and initial beam energy of 10 GeV, we have investigated the effect of the electron beam shape, radius and length on the total radiated photon energy. These beam parameters are expected to be available at the FACET II facility. Overall, for a fixed short beam length, we have demonstrated that transversely compressed electron beams convert their initial energy into synchrotron photons more efficiently. The simulations have also confirmed that both the beam

self-focusing and the photon emission mechanisms are robust for a range of beam parameters that could soon be explored in the existing accelerator facilities such as FACET II.

Furthermore, we have shown that the self-focusing and photon emission effects could be systematically enhanced during the collision of the electron beam with multiple submicrometre thick conducting foils. As a result of self-focusing, when the electron beam density increases to values greater than the target foil density, we observe that the beam fields channelled into the target and target plasma electrons are expelled from this region. We have observed an increase in the conversion efficiency during this channelling regime, and the χ_e parameter of the beam electrons grows up to a peak of approximately 3, i.e., the electric field experienced by beam electrons in their rest frame is three times the QED critical field. This indicates the possibility of accessing the QED regime (χ_e>1) without employing high- power and ultra-intense laser pulses, but only a single high-current ultra-relativistic electron beam.

Specifically, we have found that this scheme of electron beam-multiple foil interaction converts 30% of its electron energy into a dense collimated photon beam. The resultant high-energy photon beam is found to have a duration comparable to that of the electron beam ($\sim$4 fs FWHM) and is highly collimated (the photon energy is radiated in a cone with 5 mrad rms opening angle).

5.2 Outlook

In addition to our findings above, we also identify potential areas of further explorations based on our study.

5.2.1 Thick Targets

From the beam-multiple foil collisions, we observe that the beam undergoes strong compression, until it reaches the seventh foil. The process of photon emission and beam self-focusing during these collisions occur via the beam interaction with reflected fields from the conductor surface. On the other hand, when the beam reaches the seventh foil surface, the beam density is greater than the target plasma electron density and hence the target foil fails to reflect the beam self-fields. The beam self-fields channel into the target expelling all the electrons in that region. From this point, the observed photon emission is due to the fields present in the channel within the target, and not due to interaction of the beam with the fields reflected at the target boundary surface. Due to the expulsion of plasma electrons, the created channel has field strengths that are strong enough to trigger strong-field QED effects.

To understand this new channelling regime further, we investigate the collision of a transversely compressed Gaussian beam with thick targets. One can engineer these Gaussian beams with varying beam radius by carefully varying the number of initial electron-beam foil collisions. Here, we start our investigation from the channelling

regime which starts from the seventh foil and continues until the twentieth foil. The total accumulated target thickness is 0.5 μm × 14 (remaining foils) = 7 μm. We therefore let the electron beam interact with a thick target of 7 μm to further explore the channelling regime. Additionally, in order to investigate the role of collisional processes during these collisions, we choose targets with varying atomic number Z. In particular, we investigate the electron beam interaction with lithium ($Z = 3$), aluminium ($Z = 13$) and lead targets ($Z = 82$). This idea is schematically represented in Figure 5.1. In our simulations the beam has 2 nC charge, Gaussian spatial and momentum profile with $\sigma_{\parallel}$= 0.55 μm, $\sigma_{\perp}$= (a) 0.216, (b) 0.108, and (c) 0.054 μm, 10 GeV mean energy, 212 MeV full-width at half maximum (FWHM) energy spread, and 3 mm-mrad normalised emittance. The resolution of our simulation grid is dx = dy = dz=0.0125μm. As these 3D simulations are computationally very expensive, for our initial investigations, we do not increase the resolution further. With further increase in the resolution of the grid, we expect a difference of approximately 7% in the reflection regime and between 20% and 30% for channeling regime. The effect of numerical resolution on the obtained values for transversely compressed beams was already discussed in the subsection 4.6.4.

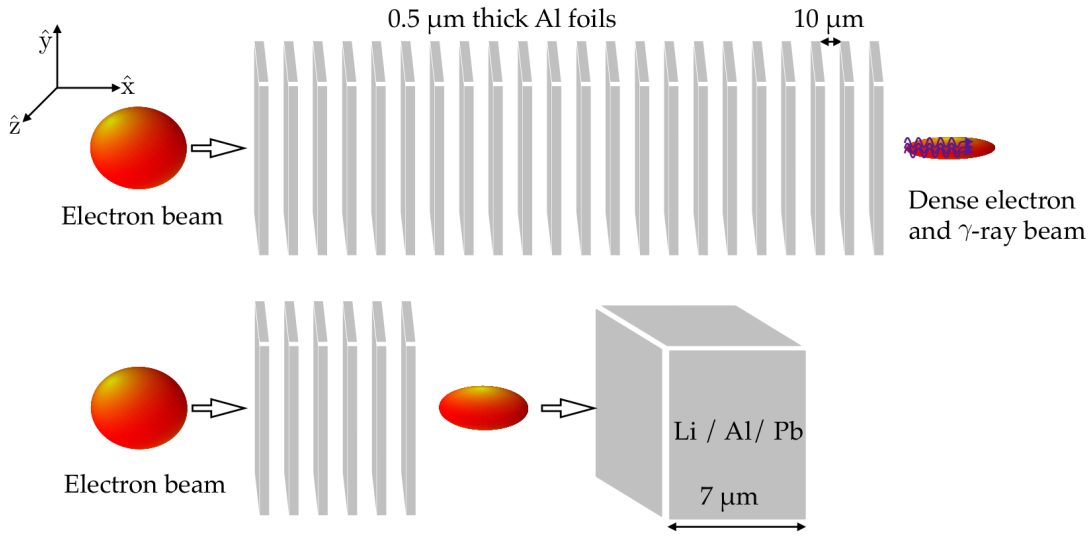

FIGURE 5.1: A schematic of electron beam interaction with 20 Al foils (top row) and beam interaction with a thick target after initially being compressed by multiple thin foils (bottom row).

The results obtained via these investigations are reported in the tables below. The electron beam density n_e in comparison to the plasma electron density n_{pe} determines the regime of interaction. If $n_e < n_{pe}$, the beam self-fields are reflected at the boundary of collision, and if $n_e > n_{pe}$, the beam self-fields channel into the target material resulting in an expulsion of plasma electrons in that region. This generates a field in the rest frame of the electron beam that is strong enough to trigger strong-field QED effects. The plasma electron densities are n_{pe} = for Li, Al and Pb respectively. For the values reported in Table 5.1, the electron beam has an initial density of $n_e(0) = 3.1 \times 10^{28}$

electrons/m^3 which is less than the plasma electrons' density initially in all three targets. Hence, we observe the reflection of beam self-fields during this interaction. Collisional processes such as bremsstrahlung emission and Bethe-Heitler pair does not contribute to electron beam energy loss during this interaction for both lithium and aluminium targets, and is negligible during electron-beam interaction with the thick lead target.

		Li	Al	Pb
Regime		Reflection	Reflection	Reflection
η	Synchrotron photons	$\sim$ 1.5%	$\sim$1.4%	$\sim$1.4%
	Multiphoton Breit-Wheeler pairs	$\sim$ 0%	$\sim$ 0%	$\sim$0%
	Bremsstrahlung photons	$\sim$ 0%	$\sim$ 0%	$\sim 6 \times 10^{-2}$%
	Bethe-Heitler pairs	$\sim$ 0%	$\sim$ 0%	$\sim 1.2 \times 10^{-3}$%
χ_e		$\sim$0.09	$\sim$0.03	$\sim$0.03

TABLE 5.1: The conversion efficiency η of electron beam energy into strong-field QED processes and collisional processes. The regime of field interaction and also the obtained maximum value of χ_e of electrons is reported. The electron beam has 2 nC charge, 10 GeV energy, $\sigma_\parallel$ = 0.55 μm and $\sigma_\perp$ = 0.216 μm.

With a slightly more compressed electron beam such that $\sigma_\parallel$ = 0.55 and $\sigma_\perp$ = 0.108 μm (refer Table 5.2), resulting in an initial electron beam density of $n_e(0) = 1.23 \times 10^{29}$ electrons/m^3, the beam density is greater than the plasma electrons' density in lithium target. The beam fields channel into the target, and we observe enhanced synchrotron photon emission in this "channelling" regime. The fields in the rest frame of the electron beam is almost three times the QED critical field, χ_e = 3. Collisional processes are still negligible during beam interaction with lithium target. On the other hand, both aluminium and lead target's plasma electrons' are still approximately greater than the electron beam density. The synchrotron photon emission in this regime is limited majorly to the initial beam-target colliding phase. The collisional processes are still negligible in comparison to strong-field processes in both aluminium and lead targets.

		Li	Al	Pb
Regime		Channeling	Reflection	Reflection
η	Synchrotron photons	$\sim$ 38%	$\sim$ 2.38%	$\sim$ 1.96%
	Multiphoton Breit-Wheeler pairs	$\sim$ 0.1%	$\sim$ 0%	$\sim$ 0%
	Bremsstrahlung photons	$\sim$ 0%	$\sim 1 \times 10^{-2}$%	$\sim 1.4 \times 10^{-2}$%
	Bethe-Heitler pairs	$\sim 9 \times 10^{-5}$%	$\sim 2 \times 10^{-4}$%	$\sim 3 \times 10^{-3}$%
χ_e		$\sim$ 3	$\sim$ 0.4	$\sim$ 0.2

TABLE 5.2: The conversion efficiency η of electron beam energy into strong-field QED processes and collisional processes. The regime of field interaction and also the obtained maximum value of χ_e of electrons is reported. The electron beam has 2 nC charge, 10 GeV energy, $\sigma_\parallel$ = 0.55 μm and $\sigma_\perp$ = 0.108 μm.

Finally, we investigate the interaction of an electron beam with $\sigma_{\parallel}$ = 0.55 μm and highly compressed $\sigma_{\perp}$ = 0.054 μm, and initial electron density $n_e(0) = 4.95 \times 10^{29}$ electrons/m^3 with thick targets (refer Table 5.3). All three targets enter the channelling regime of interaction and result in approximately more than 50% conversion of initial electron energy into gamma-photons. The χ_e value of electrons rises up to a peak value of approximately 8 and 9 in Al and Pb target. Once more, although the effect of collisional processes is enhanced in comparison to the previous two beams ($\sigma_{\perp}$ = 0.108, and 0.216 μm), it is still less significant than strong-field QED photon emission and pair production.

		Li	Al	Pb
Regime		Channeling	Channeling	Channeling
η	Synchrotron photons	$\sim$ 58.2%	$\sim$58.9%	$\sim$49.2%
	Multiphoton Breit-Wheeler pairs	$\sim$ 1.8%	$\sim$ 8.8%	$\sim$ 8.3%
	Bremsstrahlung photons	$\sim$ 0%	$\sim 1 \times 10^{-2}$%	$\sim$ 0.13%
	Bethe-Heitler pairs	$\sim$ 0%	$\sim 1.8 \times 10^{-3}$%	$\sim 2.63 \times 10^{-2}$%
χ_e		$\sim$ 3	$\sim$ 8	$\sim$ 9

TABLE 5.3: The conversion efficiency η of electron beam energy into strong-field QED processes and collisional processes. The regime of field interaction and also the obtained maximum value of χ_e of electrons is reported. The electron beam has 2 nC charge, 10 GeV energy, $\sigma_{\parallel}$= 0.55 μm and $\sigma_{\perp}$= 0.054 μm.

The results obtained indicate that the density of the electron beam with respect to the plasma electron density of the target plays a crucial role in determining if the fields of the beam get "reflected" or if the fields channel into the target. This channeling regime paves way a unique way for strong-field QED investigations with a single high-current electron beam. For computing the collisional processes of emission and pair production we have used cross-sections which account for complete screening of the nuclear field. In all the simulations, we do not observe full ionisation of the target material, and hence the cross-section underestimates the strength of collisional processes such as bremsstrahlung emission and Bethe-Heitler pair production. Having said that, since the role of collisional processes so far has not been significant, the underestimation of collisional processes should not affect the key physical results.

5.2.2 Dense collimated gamma beams

Another intriguing prospect is in relation to dense collimated gamma beams in the generation of high-Z-catalysed QED cascades or showers. QED cascades are complex physical phenomena that shed light on the interplay between strong-field QED and collective plasma effects. To summarise, QED cascades are continuous cyclical series of photon emissions and pair creations that lead to an exponential growth of number of particles. The growth rate Γ of the particles is governed by a parameter $r = \frac{W_r}{W_{pp}}$

(Thomas Grismayer, Vranic, Joana L Martins, et al., 2017) where W_r and W_{pp} determine the rate of photon emission and pair-production respectively,

$$\Gamma \simeq \begin{cases} 2W_r & \text{if } r \ll 1 \\ W_{pp} \sim W_r & \text{if } r \sim 1 \\ \sqrt{2W_r W_{pp}} & \text{if } r \gg 1. \end{cases} \tag{5.1}$$

Most of the proposals for the initiation and development of these cascades focus on the use of multiple colliding laser pulses or collision of laser pulses with electron beam. (Bell and Kirk, 2008, Bulanov, Mur, et al., 2010, Fedotov, Narozhny, et al., 2010, Sokolov et al., 2010, Bulanov, Schroeder, et al., 2013). The interaction of highly energetic (GeV) and highly collimated photon beam with a high atomic number target provides a unique possibility of studying QED cascades through the interplay of non-linear inverse Compton scattering (SFQED process) and Bethe-Heitler pair production (collisional process). In this setup, there are two routes for both photon emission and pair production, namely, the strong-field and the collisional processes (Figure 5.2).

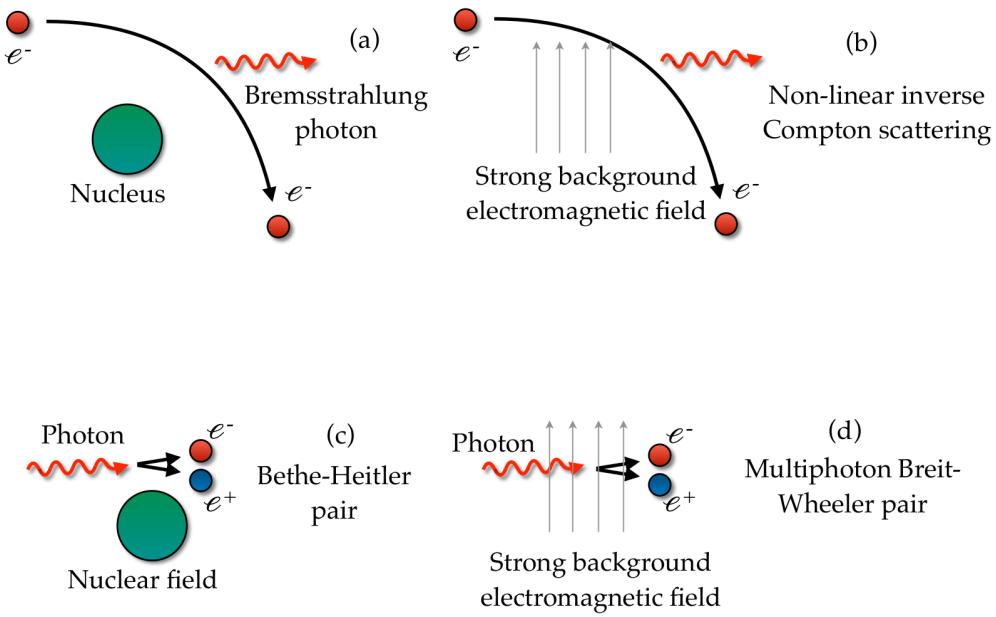

FIGURE 5.2: Photon emission and pair creation in the field of an atomic nucleus and in an external strong electromagnetic field.

To estimate the growth of particles in this setup, we analyse the growth rates for estimating how these processes compete in different situations. Firstly, we compare the rates for strong-field emission (non-linear inverse Compton scattering, NICS) and

bremsstrahlung (B) emission, $W_{r,NICS}$ and $W_{r,B}$

$$W_{r,NICS} \sim \frac{1.45\alpha m_e c^2}{\hbar}\frac{\chi_e}{\gamma_e} \sim 8.2\times 10^{18}\left(\frac{\chi_e}{\gamma_e}\right), \qquad W_{r,B} \sim \sigma_B n_{ions} v_{rel}, \tag{5.2}$$

where χ_e and γ_e are the electron quantum parameter and Lorentz factor respectively, σ_B corresponds to the bremsstrahlung emission cross-section, n_{ions} is the target ion density and v_{rel} is the velocity of the electron in the ion rest frame.

For an electron with γ=100 in the nuclear field of Pb^{+2} plasma ions with density 3.3×10^{28} ions/m^{-3} and in a moderate background field such that $\chi_e = 0.1$, the formation time for NICS is about one tenth of a femtosecond ($W_{r,NICS} = 8.2\times 10^{15}$ s^{-1}), and for bremsstrahlung emission, it is in the order of few picoseconds ($W_{r,B} = 3.5\times 10^{11}$ s^{-1}). Hence, we can reasonably conclude that strong-field emission will dominate over collisional emission in the scale of few tens of femtoseconds up to picoseconds.

Similarly, we analyse the rates for pair creation via non-linear Breit Wheeler $W_{pp,BW}$ and Bethe-Heitler pair production $W_{pp,BH}$

$$\begin{aligned} W_{pp,BW} &\sim 0.38\frac{\alpha m_e^2 c^4}{\hbar\varepsilon_\gamma}\chi_\gamma^{2/3} \quad \text{for } \chi_\gamma \gg 1 \\ W_{pp,BW} &\sim 0.23\frac{\alpha m_e^2 c^4}{\hbar\varepsilon_\gamma}\chi_\gamma e^{\frac{-8}{3\chi\gamma}} \quad \text{for } \chi_\gamma \ll 1 \\ W_{pp,BH} &= \sigma_{pp,BH} n_{ions} c, \end{aligned} \tag{5.3}$$

where χ_γ and ε_γ are the photon quantum parameter and the normalised photon energy, and $\sigma_{pp,BH}$ corresponds to the Bethe-Heitler pair production cross-section. In our discussed setup, non-linear Breit-Wheeler pair production is exponentially suppressed as $\chi_\gamma \ll 1$. On the other hand, for photons with energy ≥ 1 GeV, $W_{pp,BH} \sim 4.2\times 10^{10}$ s^{-1}, corresponding to a formation time of few tens of picoseconds. Hence for pair production, Bethe-Heitler dominates over non-linear Breit-Wheeler process. In conclusion, the dominating channels for photon emission and pair production are NICS and Bethe-Heitler pair production when $\chi_\gamma \lesssim 0.5$.

With this information, we estimate for the growth rate (Γ) of the number of particles in the system. From the estimates of $W_{r,NICS}$ and $W_{pp,BH}$, we get $r \sim W_{r,NICS}/W_{pp,BH} \gg 1$ which implies $\Gamma \sim \sqrt{2W_{r,NICS}W_{pp,BH}}$ $s^{-1} \sim 1.8\times 10^{13}$ s^{-1}. This growth rate corresponds to a net formation time and length of ∼54 fs and ∼16 μm respectively. In short, the "fast" photon emission (femtoseconds) compensates for the "slow" pair production (picoseconds) time scale with the extremely abundant production of photons, resulting in a comparatively small formation length. This implies that if an external driving field leads to the production of copious gamma rays in the presence of high-Z nuclei, the high-Z nuclei may substantially contribute to the formation of pairs and to the cyclic creation of new particle generations when the χ_γ parameters of photons is sufficiently small ($\chi_\gamma \lesssim 0.3$) such that the multiphoton-Breit-Wheeler channel is blocked, practically. Based on all of the above, we have demonstrated a feasible route to reproduce

extreme conditions present in astrophysical environments that is determined by a complex interplay of strong-field QED and multi-particle dynamics.

Bibliography

Adler, Robert J (1982). “Image field focusing of intense ultrarelativistic electron beams in vacuum”. In: *Part. Accel.* 12, pp. 39–44.

Akhiezer, A. I. and V. B. Berestetskii (1986). *Quantum electrodynamics*.

Andersen, BC et al. (2020). “A bright millisecond-duration radio burst from a Galactic magnetar”. In: *arXiv preprint arXiv:2005.10324*.

Arber, TD et al. (2015). “Contemporary particle-in-cell approach to laser-plasma modelling”. In: *Plasma Physics and Controlled Fusion* 57.11, p. 113001.

Artemenko, II and I Yu Kostyukov (2017). “Ionization-induced laser-driven QED cascade in noble gases”. In: *Physical Review A* 96.3, p. 032106.

Aurenche, Patrick, François Gelis, and H Zaraket (2000). “Landau-Pomeranchuk-Migdal effect in thermal field theory”. In: *Physical Review D* 62.9, p. 096012.

Bashmakov, VF et al. (2014). “Effect of laser polarization on quantum electrodynamical cascading”. In: *Physics of Plasmas* 21.1, p. 013105.

Bell, AR and John G Kirk (2008). “Possibility of prolific pair production with high-power lasers”. In: *Physical review letters* 101.20, p. 200403.

Benedetti, Alberto, Matteo Tamburini, and Christoph H Keitel (2018). “Giant collimated gamma-ray flashes”. In: *Nature Photonics* 12.6, pp. 319–323.

Ben-Ismaïl, Ahmed et al. (2011). “Compact and high-quality gamma-ray source applied to 10 μ m-range resolution radiography”. In: *Applied Physics Letters* 98.26, p. 264101.

Bochenek, Christopher D et al. (2020). “A fast radio burst associated with a Galactic magnetar”. In: *arXiv preprint arXiv:2005.10828*.

Bulanov, SS, VD Mur, et al. (2010). “Multiple colliding electromagnetic pulses: a way to lower the threshold of e+ e- pair production from vacuum”. In: *Physical review letters* 104.22, p. 220404.

Bulanov, SS, CB Schroeder, et al. (2013). “Electromagnetic cascade in high-energy electron, positron, and photon interactions with intense laser pulses”. In: *Physical Review A* 87.6, p. 062110.

Chang, HX et al. (2017). “Brilliant petawatt gamma-ray pulse generation in quantum electrodynamic laser-plasma interaction”. In: *Scientific reports* 7, p. 45031.

Chen, Alexander Y, Fábio Cruz, and Anatoly Spitkovsky (2020). “Filling the Magnetospheres of Weak Pulsars”. In: *The Astrophysical Journal* 889.1, p. 69.

Chen, CD et al. (2008). “A Bremsstrahlung spectrometer using k-edge and differential filters with image plate dosimeters”. In: *Review of Scientific Instruments* 79.10, 10E305.

Chen, Hui, F Fiuza, et al. (2015). “Scaling the yield of laser-driven electron-positron jets to laboratory astrophysical applications”. In: *Physical review letters* 114.21, p. 215001.

Chen, Hui, Scott C Wilks, et al. (2009). “Relativistic positron creation using ultraintense short pulse lasers”. In: *Physical review letters* 102.10, p. 105001.

Chen, Hui, SC Wilks, et al. (2010). “Relativistic quasimonoenergetic positron jets from intense laser-solid interactions”. In: *Physical review letters* 105.1, p. 015003.

Cipiccia, Silvia et al. (2012). “A tuneable ultra-compact high-power, ultra-short pulsed, bright gamma-ray source based on bremsstrahlung radiation from laser-plasma accelerated electrons”. In: *Journal of Applied Physics* 111.6, p. 063302.

Compant La Fontaine, A, C Courtois, and E Lefebvre (2012). “Production of multi-MeV Bremsstrahlung x-ray sources by petawatt laser pulses on various targets”. In: *Physics of Plasmas* 19.2, p. 023104.

Courtois, C et al. (2013). “Characterisation of a MeV Bremsstrahlung x-ray source produced from a high intensity laser for high areal density object radiography”. In: *Physics of Plasmas* 20.8, p. 083114.

Cowan, TE et al. (2000). “Photonuclear fission from high energy electrons from ultraintense laser-solid interactions”. In: *Physical Review Letters* 84.5, p. 903.

Davies, Handel, HA Bethe, and LC Maximon (1954). “Theory of bremsstrahlung and pair production. II. Integral cross section for pair production”. In: *Physical Review* 93.4, p. 788.

Del Gaudio, F et al. (2019). “Bright γ rays source and nonlinear Breit-Wheeler pairs in the collision of high density particle beams”. In: *Physical Review Accelerators and Beams* 22.2, p. 023402.

Derouillat, Julien et al. (2018). “Smilei: A collaborative, open-source, multi-purpose particle-in-cell code for plasma simulation”. In: *Computer Physics Communications* 222, pp. 351–373.

Di Piazza, A, C Müller, et al. (2012). “Extremely high-intensity laser interactions with fundamental quantum systems”. In: *Reviews of Modern Physics* 84.3, p. 1177.

Di Piazza, A, Matteo Tamburini, et al. (2018). “Implementing nonlinear Compton scattering beyond the local-constant-field approximation”. In: *Physical Review A* 98.1, p. 012134.

Di Piazza, Antonino, Karen Zaven Hatsagortsyan, and Christoph Helmut Keitel (2005). “Harmonic generation from laser-driven vacuum”. In: *Physical Review D* 72.8, p. 085005.

Duclous, Roland, John G Kirk, and AR Bell (2010). “Monte Carlo calculations of pair production in high-intensity laser–plasma interactions”. In: *Plasma Physics and Controlled Fusion* 53.1, p. 015009.

Elkina, NV et al. (2011). “QED cascades induced by circularly polarized laser fields”. In: *Physical Review Special Topics-Accelerators and Beams* 14.5, p. 054401.

Fedotov, AM and NB Narozhny (2007). “Generation of harmonics by a focused laser beam in the vacuum”. In: *Physics Letters A* 362.1, pp. 1–5.

Fedotov, AM, NB Narozhny, et al. (2010). “Limitations on the attainable intensity of high power lasers”. In: *Physical review letters* 105.8, p. 080402.

Fernsler, RF, RF Hubbard, and SP Slinker (1990). "Foil focusing of electron beams". In: *Journal of applied physics* 68.12, pp. 5985–5994.

Gelfer, EG et al. (2015). "Optimized multibeam configuration for observation of QED cascades". In: *Physical Review A* 92.2, p. 022113.

Gonoskov, Arkady et al. (2017). "Ultrabright GeV photon source via controlled electromagnetic cascades in laser-dipole waves". In: *Physical Review X* 7.4, p. 041003.

Grismayer, Thomas, Marija Vranic, Joana Luis Martins, et al. (2016). "Laser absorption via quantum electrodynamics cascades in counter propagating laser pulses". In: *Physics of Plasmas* 23.5, p. 056706.

Grismayer, Thomas, Marija Vranic, Joana L Martins, et al. (2017). "Seeded QED cascades in counterpropagating laser pulses". In: *Physical Review E* 95.2, p. 023210.

Habs, D. et al. (2009). "Vision of nuclear physics with photo-nuclear reactions by laser-driven beams". In: *The European Physical Journal D* 55, pp. 279–285. DOI: 10.1140/epjd/e2009-00101-2.

Hammond, P (1960). "Electric and magnetic images". In: *Proceedings of the IEE-Part C: Monographs* 107.12, pp. 306–313.

Heinzl, Thomas et al. (2006). "On the observation of vacuum birefringence". In: *Optics communications* 267.2, pp. 318–321.

Heisenberg, Werner and Heinrich Euler (1936). "Folgerungen aus der diracschen theorie des positrons". In: *Zeitschrift für Physik* 98.11-12, pp. 714–732.

Huang, TW et al. (2019). "Highly efficient laser-driven Compton gamma-ray source". In: *New Journal of Physics* 21.1, p. 013008.

Humphries Jr, S and Carl B Ekdahl (1988). "Image charge focusing of relativistic electron beams". In: *Journal of applied physics* 63.2, pp. 583–585.

Humphries, S., Carl Ekdahl, and D. M. Woodall (1989). "Image current guiding of a relativistic electron beam in a foil focusing system". In: *Applied Physics Letters* 54.22, pp. 2195–2197. DOI: 10.1063/1.101142. eprint: https://doi.org/10.1063/1.101142. URL: https://doi.org/10.1063/1.101142.

Humphries, Stanley (1983). "Equilibria for foil focused relativistic electron beams". In: *Part. Accel.* 13, pp. 249–253.

Ji, LL et al. (2014). "Energy partition, γ-ray emission, and radiation reaction in the near-quantum electrodynamical regime of laser-plasma interaction". In: *Physics of Plasmas* 21.2, p. 023109.

Jirka, Martin, Ondrej Klimo, Yan-Jun Gu, et al. (2020). "Enhanced photon emission from a double-layer target at moderate laser intensities". In: *Scientific Reports* 10.1, pp. 1–8.

Jirka, Martin, Ondrej Klimo, Marija Vranic, et al. (2017). "QED cascade with 10 PW-class lasers". In: *Scientific Reports* 7.1, pp. 1–7.

Kaspi, Victoria M and Andrei M Beloborodov (2017). "Magnetars". In: *Annual Review of Astronomy and Astrophysics* 55, pp. 261–301.

Katkov, VM, Vladimir Moiseevich Strakhovenko, et al. (1998). *Electromagnetic processes at high energies in oriented single crystals*. World Scientific.

Kmetec, J. D. et al. (1992). “MeV x-ray generation with a femtosecond laser”. In: *Phys. Rev. Lett.* 68 (10), pp. 1527–1530. DOI: 10.1103/PhysRevLett.68.1527. URL: https://link.aps.org/doi/10.1103/PhysRevLett.68.1527.

Koch, H. W. and J. W. Motz (1959). “Bremsstrahlung Cross-Section Formulas and Related Data”. In: *Rev. Mod. Phys.* 31 (4), pp. 920–955. DOI: 10.1103/RevModPhys.31.920. URL: https://link.aps.org/doi/10.1103/RevModPhys.31.920.

Landau, LD and EM Lifshitz (1980). *The classical theory of fields Butterworth*.

Li, CK et al. (2020). “Identification of a non-thermal X-ray burst with the Galactic magnetar SGR 1935+ 2154 and a fast radio burst with Insight-HXMT”. In: *arXiv preprint arXiv:2005.11071*.

Li, Jian-Xing, Karen Z. Hatsagortsyan, et al. (2015). “Attosecond Gamma-Ray Pulses via Nonlinear Compton Scattering in the Radiation-Dominated Regime”. In: *Phys. Rev. Lett.* 115 (20), p. 204801. DOI: 10.1103/PhysRevLett.115.204801. URL: https://link.aps.org/doi/10.1103/PhysRevLett.115.204801.

Li, Jian-Xing, Karen Z Hatsagortsyan, et al. (2015). “Attosecond gamma-ray pulses via nonlinear compton scattering in the radiation-dominated regime”. In: *Physical review letters* 115.20, p. 204801.

Liang, Edison (2010). “Intense laser pair creation and applications”. In: *High Energy Density Physics* 6.2, pp. 219–222.

Lin, L et al. (2020). “Stringent upper limits on pulsed radio emission during an active bursting phase of the Galactic magnetar SGRJ1935+ 2154”. In: *arXiv preprint arXiv:2005.11479*.

Lobet, Mathieu (2015). “Effets radiatifs et d’électrodynamique quantique dans l’interaction laser-matière ultra-relativiste”. PhD thesis. Bordeaux.

Macchi, Andrea et al. (2010). “Radiation pressure acceleration of ultrathin foils”. In: *New Journal of Physics* 12.4, p. 045013.

Magnusson, J et al. (2019). “Laser-particle collider for multi-GeV photon production”. In: *Physical review letters* 122.25, p. 254801.

Marklund, Mattias and Padma K Shukla (2006). “Nonlinear collective effects in photon-photon and photon-plasma interactions”. In: *Reviews of modern physics* 78.2, p. 591.

Martinez, Bertrand (2018). “Radiative and quantum electrodynamic effects in ultra-relativistic laser-matter interaction”. PhD thesis.

Medin, Zach and Dong Lai (2010). “Pair cascades in the magnetospheres of strongly magnetized neutron stars”. In: *Monthly Notices of the Royal Astronomical Society* 406.2, pp. 1379–1404.

Migdal, A. B. (1956). “Bremsstrahlung and Pair Production in Condensed Media at High Energies”. In: *Phys. Rev.* 103 (6), pp. 1811–1820. DOI: 10.1103/PhysRev.103.1811. URL: https://link.aps.org/doi/10.1103/PhysRev.103.1811.

Mironov, AA, NB Narozhny, and AM Fedotov (2014). “Collapse and revival of electromagnetic cascades in focused intense laser pulses”. In: *Physics Letters A* 378.44, pp. 3254–3257.

Mironov, Arsenii Antonovich, Aleksandr Mikhailovich Fedotov, and Nikolai Borisovich Narozhnyi (2016). "Generation of quantum-electrodynamic cascades in oblique collisions of ultrarelativistic electrons with an intense laser field". In: *Quantum Electronics* 46.4, p. 305.

Mösta, Philipp et al. (2015). "A large-scale dynamo and magnetoturbulence in rapidly rotating core-collapse supernovae". In: *Nature* 528.7582, pp. 376–379.

Motz, J. W., Haakon A. Olsen, and H. W. Koch (1969). "Pair Production by Photons". In: *Rev. Mod. Phys.* 41 (4), pp. 581–639. DOI: 10.1103/RevModPhys.41.581. URL: https://link.aps.org/doi/10.1103/RevModPhys.41.581.

Nakamura, Tatsufumi et al. (2012). "High-power γ-ray flash generation in ultraintense laser-plasma interactions". In: *Physical review letters* 108.19, p. 195001.

Nanbu, K (1997). "Theory of cumulative small-angle collisions in plasmas". In: *Physical Review E* 55.4, p. 4642.

Nanbu, K and Shigeru Yonemura (1998). "Weighted particles in Coulomb collision simulations based on the theory of a cumulative scattering angle". In: *Journal of Computational Physics* 145.2, pp. 639–654.

Nuter, R et al. (2011). "Field ionization model implemented in particle in cell code and applied to laser-accelerated carbon ions". In: *Physics of Plasmas* 18.3, p. 033107.

Olsen, Haakon and L. C. Maximon (1959). "Photon and Electron Polarization in High-Energy Bremsstrahlung and Pair Production with Screening". In: *Phys. Rev.* 114 (3), pp. 887–904. DOI: 10.1103/PhysRev.114.887. URL: https://link.aps.org/doi/10.1103/PhysRev.114.887.

Olsen, Haakon, L. C. Maximon, and Harald Wergeland (1957). "Theory of High-Energy Bremsstrahlung and Pair Production in a Screened Field". In: *Phys. Rev.* 106 (1), pp. 27–46. DOI: 10.1103/PhysRev.106.27. URL: https://link.aps.org/doi/10.1103/PhysRev.106.27.

Pérez, F et al. (2012). "Improved modeling of relativistic collisions and collisional ionization in particle-in-cell codes". In: *Physics of Plasmas* 19.8, p. 083104.

Powell, Devin (2013). "Europe sets sights on lasers". In: *Nature* 500.7462, pp. 264–265.

Qu, Kenan, Sebastian Meuren, and Nathaniel J Fisch (2020). "Observing Collective Plasma Effects in Beam-Driven QED Cascades via Laser Frequency Upconversion". In: *arXiv preprint arXiv:2001.02590*.

Remington, Bruce A, R Paul Drake, and Dmitri D Ryutov (2006). "Experimental astrophysics with high power lasers and Z pinches". In: *Reviews of Modern Physics* 78.3, p. 755.

Ridgers, CP et al. (2012). "Dense electron-positron plasmas and ultraintense γ rays from laser-irradiated solids". In: *Physical review letters* 108.16, p. 165006.

Ridnaia, A et al. (2020). "A peculiar hard X-ray counterpart of a Galactic fast radio burst". In: *arXiv preprint arXiv:2005.11178*.

Salvat, Francesc, José M Fernández-Varea, Josep Sempau, et al. (2008). "PENELOPE-2008: A code system for Monte Carlo simulation of electron and photon transport". In: *the Workshop Proceedings, June*.

Sampath, Archana, Xavier Davoine, et al. (2020). “Extremely Dense Gamma-Ray Pulses in Electron Beam-Multifoil Collisions”. In: *arXiv e-prints*, arXiv:2009.01808, arXiv:2009.01808. arXiv: 2009.01808. URL: https://arxiv.org/abs/2009.01808.

Sampath, Archana and Matteo Tamburini (2018). “Towards realistic simulations of QED cascades: Non-ideal laser and electron seeding effects”. In: *Physics of Plasmas* 25.8, p. 083104.

Santala, MIK et al. (2000). “Effect of the plasma density scale length on the direction of fast electrons in relativistic laser-solid interactions”. In: *Physical Review Letters* 84.7, p. 1459.

Sarri, Gianluca et al. (2015). “Generation of neutral and high-density electron–positron pair plasmas in the laboratory”. In: *Nature communications* 6.1, pp. 1–8.

Sauter, Fritz (1931). “Über das Verhalten eines Elektrons im homogenen elektrischen Feld nach der relativistischen Theorie Diracs”. In: *Zeitschrift für Physik* 69.11-12, pp. 742–764.

Schwinger, Julian (1951). “On gauge invariance and vacuum polarization”. In: *Physical Review* 82.5, p. 664.

Seguchi, T et al. (2002). “New material synthesis by radiation processing at high temperature—polymer modification with improved irradiation technology”. In: *Radiation Physics and Chemistry* 63.1, pp. 35–40.

Seltzer, Stephen M and Martin J Berger (1985). “Bremsstrahlung spectra from electron interactions with screened atomic nuclei and orbital electrons”. In: *Nuclear Instruments and Methods in Physics Research Section B: Beam Interactions with Materials and Atoms* 12.1, pp. 95–134.

Sentoku, Yasuhiko and Andreas J Kemp (2008). “Numerical methods for particle simulations at extreme densities and temperatures: Weighted particles, relativistic collisions and reduced currents”. In: *Journal of Computational Physics* 227.14, pp. 6846–6861.

Sokolov, Igor V et al. (2010). “Pair creation in QED-strong pulsed laser fields interacting with electron beams”. In: *Physical review letters* 105.19, p. 195005.

Strickland, Donna and Gerard Mourou (1985). “Compression of amplified chirped optical pulses”. In: *Optics communications* 56.3, pp. 219–221.

Tamburini, Matteo, Antonino Di Piazza, and Christoph H Keitel (2017). “Laser-pulse-shape control of seeded QED cascades”. In: *Scientific reports* 7.1, pp. 1–8.

Tamburini, Matteo and Sebastian Meuren (2019). “Efficient High-Energy Photon Production in the Supercritical QED Regime”. In: *arXiv preprint arXiv:1912.07508*.

Tamburini, M et al. (2010). “Radiation reaction effects on radiation pressure acceleration”. In: *New Journal of Physics* 12.12, p. 123005.

Tavani, M et al. (2020). “An X-Ray Burst from a Magnetar Enlightening the Mechanism of Fast Radio Bursts”. In: *arXiv preprint arXiv:2005.12164*.

Timokhin, AN and AK Harding (2019). “On the maximum pair multiplicity of pulsar cascades”. In: *The Astrophysical Journal* 871.1, p. 12.

Toll, John Sampson (1952). “The Dispersion Relation for Light and its Application to Problems Involving Electron Pairs.” In: *PhDT*.

Tsai, Yung-Su (1974). “Pair production and bremsstrahlung of charged leptons”. In: *Rev. Mod. Phys.* 46 (4), pp. 815–851. DOI: 10.1103/RevModPhys.46.815. URL: https://link.aps.org/doi/10.1103/RevModPhys.46.815.

Vranic, Marija, Thomas Grismayer, Ricardo A Fonseca, et al. (2016). “Electron–positron cascades in multiple-laser optical traps”. In: *Plasma Physics and Controlled Fusion* 59.1, p. 014040.

Vranic, Marija, Thomas Grismayer, Sebastian Meuren, et al. (2019). “Are we ready to transfer optical light to gamma-rays?” In: *Physics of Plasmas* 26.5, p. 053103.

Vyskočil, Jiří, Ondřej Klimo, and Stefan Weber (2018). “Simulations of bremsstrahlung emission in ultra-intense laser interactions with foil targets”. In: *Plasma Physics and Controlled Fusion* 60.5, p. 054013.

Wang, Wei-Min et al. (2018). “Collimated ultrabright gamma rays from electron wiggling along a petawatt laser-irradiated wire in the QED regime”. In: *Proceedings of the National Academy of Sciences* 115.40, pp. 9911–9916.

Xue, YQ et al. (2019). “A magnetar-powered X-ray transient as the aftermath of a binary neutron-star merger”. In: *Nature* 568.7751, pp. 198–201.

Yakimenko, V, L Alsberg, et al. (2019). “FACET-II facility for advanced accelerator experimental tests”. In: *Physical Review Accelerators and Beams* 22.10, p. 101301.

Yakimenko, V, S Meuren, et al. (2019). “Prospect of studying nonperturbative QED with beam-beam collisions”. In: *Physical review letters* 122.19, p. 190404.

Zhu, Xing-Long et al. (2020). “Extremely brilliant GeV γ-rays from a two-stage laser-plasma accelerator”. In: *Science Advances* 6.22, eaaz7240.

Acknowledgements

I take this opportunity to express my gratitude for the city of Heidelberg in Germany and my family back home in India for providing me with a conducive sphere in which I could materialise my ambitions. I express my gratitude to my revered teachers and elderly mentors since the days of school, and all those who have shaped my interests in sciences. The presentation of this work is a testimony to their passion and diligent care in my personal and professional growth.

I profoundly thank Prof. Christoph H. Keitel for the opportunity to work under his leadership and supervision over the past years. I thank Dr. Matteo Tamburini for being my first port of guidance for all the projects that we have collaborated since the commencement of by stay at MPIK. His directions have guided this dissertation and my significant publications thus far. I thank the administrative staff of MPIK who work tirelessly behind the scenes to make our stay at the institute and outside of it smooth. I acknowledge the financial support awarded by International Max Planck Research School for Quantum Dynamics (IMPRS-QD).

I am immensely grateful to Prof. Joerg Jaeckel for his kind consent to be the referee to my dissertation; Prof. Dr. Rüdiger Klingeler and Prof. Dr. Kurt Roth for their kind consent to be the examiners to my dissertation. It is my pleasure and honour to present my work on this topic to the esteemed examination committee.

Amongst my colleagues at MPIK, I thank Maitreyi Sangal, Dr. Sergei Kobzak, Dr. Ujjwal Sinha, Dr. Oleg Skoromnik, Dr. Sergey Bragin for the various technical discussions we have had over the years, which enhanced by understanding in this field and beyond. Particularly, Maitreyi Sangal has been my all weather pillar of support and Sergei Kobzak has kindly accommodated my presence while sharing our office room.

A big thank you to colleagues Daniel Bakucz-Canário, Fabien Niel, Kamil Dzikowski, Petar Andrejić, Dr. Halil Cakir, Dr. Shikha Bhadoria and Dr. Suo Tang for sharing their time, thoughts and friendship. Without their warmth and fondness, my stay at MPIK would have been incomplete. At a personal level, I would recall the support from my roommates in Heidelberg, Tina Schöbel and Stefan Stadtherr. A special mention to Yogesh, Atul, Sayee and all other friends from across the world for their unwavering belief in my abilities.

Finally, and most specially, I cannot express in mere words the love and invaluable contribution of my mother, Ms. Suseela Sampath, my father, Mr. Sampath Sesha Iyengar and my sister, Ms. Aparna Sampath throughout this challenging and yet satisfying journey.